UCLA
UCLA Electronic Theses and Dissertations

Title

Alignment and Load Transfer in Carbon Nanotube and Dicyclopentadiene Composites

Permalink

https://escholarship.org/uc/item/5pj3j4rw

Author

Severino, Joseph Vincent

Publication Date

2015

Peer reviewed|Thesis/dissertation

UNIVERSTIY OF CALIFORNIA

Los Angeles

Alignment and Load Transfer in Carbon Nanotube and Dicyclopentadiene Composites

A dissertation submitted in partial satisfaction of the

requirements of the degree Doctor of Philosophy

in Materials Science and Engineering

By

Joseph Vincent Severino

2015

ABSTRACT OF THE DISSERTATION

Alignment and Load Transfer in Carbon Nanotube and Dicyclopentadiene Composites

By

Joseph Vincent Severino

Doctor of Philosophy in Materials Science and Engineering

University of California, Los Angeles 2015

Professor Jenn-Ming Yang, Chair

Individual carbon nanotubes (CNTs) are the strongest materials available but their macroscopic assemblies are weak. This work establishes a new thermosetting dicyclopentadiene (DCPD) and CNT composite that increases the strength of CNT assemblies. These high volume fraction and void free structures constitute advanced materials that could one day replace traditional composite systems. To further the understanding of physical interactions between polymer and CNTs, a novel "capstan" load transfer mechanism is also introduced. Self-supporting assemblies of interconnected carbon nanotubes were stretched, twisted and compressed to fashion composites by the infusion and polymerization of low viscosity DCPD based monomeric

resins. The properties of the CNTs, polymer and composite were characterized with thermal gravimetric analysis (TGA), dynamic mechanical analysis (DMA) and Raman spectroscopy. The microstructure was analyzed by wide angle X-ray scattering (WAXS), scanning electron microscopy (SEM) and transmission electron microscopy (TEM).

Sheets were drawn at 15 m/min from a growth furnace to impart alignment then stretched to further modify alignment. The mechanical properties were determined in five orientations with respect to the growth direction. The strength was nearly three times higher along this growth direction than it was perpendicular, and modulus was nearly six times higher. Transverse stretching achieved 1.5 times the elongation but alignment was inferior due to CNT kinking that prevented alignment and consolidation.

Composites yarns and sheets were investigated for the mechanical properties, microstructure and load transfer. The DCPD resin was found to wet the CNTs and lubricated deformation. This reduced loads during processing, and curing solidified the aligned and consolidated structure. The stretched and twisted composite yarns increased the failure stress 51%. In aligned composite sheet, the failure stress increased 200%. The increased stresses were attributed to load transfer by a capstan mechanism that utilized the kinked CNTs that formed as a result of stretching. This mechanism reflects the tortuous structure of real CNT assemblies.

The dissertation of Joseph Vincent Severino is approved.

Robert F. Hicks

Gaurav N. Sant

Suneel Kodambaka

Jenn-Ming Yang, Committee Chair

University of California, Los Angeles

2015

This dissertation is dedicated to my father, Gene Severino, for all his guidance,

teaching and support. He was overcome by cancer in 2012 but he was truly an

inspiration.

TABLE OF CONTENTS

LIST OF FIGURES

LIST OF TABLES

ACKNOWLEDGMENTS

I would like to thank my family. My parents, Gene and Linda Severino, my brother Nick Severino and Sisters, Gina and Angie Severino. They were always supportive.

I want to acknowledge my former and current lab members and collogues. The support and advice of Professor Arie Venkert, Dr. Igor de Rosa, Dr. Wei Yuan, Dr. Po-Ching Yeh, Dr. Jonathan Quan, Dr. Yuanwei (Edward) Chang, Hang Yu, Wenbo (Kevin) Xin, Jose Gaviriaje, Eric Sasse, Tait McLouth and Eric Marin have been invaluable. I also want to thank my PhD. committee members Professor Gaurav Sant, Professor Suneel Kodambaka, Professor Robert Hicks and my advisor, Professor Jenn-Ming Yang. They have motivated me to be a better scientist and helped me refine my research. I also thank Professor David Scott for making my research possible with the use of his laboratory. I would especially like to thank Larry Carlson, my P.I., for supporting me throughout my graduate program. I also thank the people at Surfx Technologies, Materia Inc., Nanocomp Technologies Inc and the Aerospace Corporation. Finally, I thank the United States Department of Defense who funded all the research that went into this dissertation.

VITA

After finishing high school in 2004, Joseph Severino attended Palomar Community

College between 2004 and 2006 while working in the quality assurance department of a

software company in Carlsbad CA. He was admitted to the University of California Los

Angeles in 2006 where he studied materials science and engineering, receiving his B.S.

in 2009. He then spent the summer of 2009 developing fabrics for protection against

laceration, abrasion and penetration at Neptunic Technologies Inc. He was admitted

into the graduate program at the University of California Los Angeles in the fall of 2009.

From 2010 to 2015 he worked as a sports equipment engineer for LC Technologies

(Santa Clarita CA). In 2011 he was a teaching assistant for the introduction to materials

characterization with electron microscopy. From 2011 to 2015 he was a research

assistant with a joint appointment at the Easton Institute for Technology Advancement

and the department of Materials Science and Engineering at the University of California

Los Angeles.

CHAPTER 1: INTRODUCTION

In the 1980's a new truncated icosahedron polymorph of carbon was discovered that resembled the pattern of hexagons and pentagons seen on a soccer ball. This carbon structure was given the name Buckminster fullerene [1, 2]. While examining the soot that results from the production of fullerenes, Iijima discovered the existence of multi wall carbon nanotubes [3]. However it has also been suggested that carbon nanotubes were found in the 1960's, but the characterization tools were not available to adequately establish the structure [4]. Two years after Iijima's discovery the existence of single wall nanotubes was confirmed [5, 6]. These carbon polymorphs resemble a rolled up tube of graphite planes. The unique material has received an enormous amount of research interest due to its properties, high aspect ratio and quasi one dimensional structure. The exceptional electrical, thermal and mechanical properties that have garnered its application in many areas. The thermal conductivity of carbon nanotubes is on the same order as diamond at 3000 W/mK for multiwall nanotubes (MWNTs) and 3500 W/mK for single wall nanotubes (SWNTs) [7]. This is far better than the in plane thermal conductivity of graphite at 2000 W/mK. They have better conductivity than copper with 10^6 S/cm for SWNTs [8] and 3 x 10^4 S/cm for MWNTs [9]. Furthermore, individual nanotubes have demonstrated tensile strength of 150 GPa [10][150 GPa ref] and modulus of 1 TPa [11]. The carbon nanotubes exceptional properties have driven their broad application in many fields. They have been used to

form conductive plastics [12-14], Lithium ion batteries [15-17], fuel cells [18-20], microelectronic interconnects [21-23], semiconductor transistor channels [24, 25], energy storage [18, 26-30], biosensors [31-33], field emission [34-37], structural composites [38-41], super capacitors [27-29, 42], actuators [43-46] and other commercial applications [47-50]

In the present work the mechanical properties are of the most interest because harnessing the strength of individual nanotubes in large scale structures would revolutionize manufacturing. Cornwell et al. [51] modeled the idealized properties of a perfectly fabricated bundle of carbon nanotubes and they found a tensile strength of 60 GPa, a modulus of 700 GPa and elongation to failure of 15%. This would make carbon nanotube assemblies the strongest and toughest materials available. However these properties are not achieved in real carbon nanotube structures as a result of poor adhesion, alignment and packing. Furthermore the mechanical properties of carbon nanotubes themselves can vary widely [52]. There are many methods available to process CNT assemblies to improve the mechanical properties, but deep understanding of the effects processing has on the microstructure is lacking. Furthermore, establishing connections between the various processing methods and the final mechanical properties is also lacking. This work introduces a novel dicyclopentadiene and carbon nanotube composite system. It also aims to establish methodologies to characterize the microstructure of the composites. Furthermore, it investigates the relationship

between the microstructure and mechanical properties, suggesting a capstan

mechanism for load transfer.

In chapter 2 a background and literature review of carbon nanotubes and there

assemblies is given. This will start with the various carbon bonding states and the effect

this bonding has on structure and properties. Then the various shapes and sizes of

carbon nanotubes are discussed, along with the helical arrangement of carbon atoms in

nanotubes and the effect this has on properties. Then the physical properties of

individual nanotubes will be reviewed. The growth techniques and mechanisms will be

discussed, including the effects the growth parameters have on the structure and

quality of nanotubes. The assembly of carbon nanotubes into larger structures will then

be discussed along with the properties of the assemblies and related composites.

Furthermore, the alignment of the CNT assemblies will be reviewed starting with

methods to quantify alignment, followed by approaches to achieve alignment. Finally,

models developed to understand the load transfer between nanotubes and their

surroundings will be reviewed.

The properties of carbon nanotube assemblies can vary widely depending on growth

conditions and post processing. Chapter 3 characterizes the carbon nanotube material

used for the present research. The aim is to give the reader an understanding of the

CNTs and the structures in the assemblies under investigation. The analysis starts at the

early growth stages by looking at samples that were retrieved near the feedstock

injector of the growth furnace. Then the nanotubes that make up the CNT assemblies

are characterized with electron microscopy and Raman spectroscopy. Then the CNT

assemblies are investigated to understand the structure of the network, how the CNTs

bundle together and how bundles interconnect to form large scale CNT assemblies.

Chapter 4 is a paper to be published under the title "Progression of Alignment in

Stretched CNT Sheets Determined by Wide Angle X-ray Scattering." The goal of this

work is to understand the rearrangement of the CNT assemblies in response to

deformation. The CNT material is characterized for quality by thermal gravimetric

analysis. Wide angle X-Ray scattering is used to find the distribution of carbon

nanotubes around the drawing axis used during growth and with respect to the axis

used for post-stretching. Conclusions are drawn about the mechanical properties versus

alignment and the total alignment achieved prior to failure. Also structural features in

the CNT assemblies are discussed based on the mechanical response and the structural

rearrangement. Furthermore, electron microscopy is utilized to observe the evolution

of kinks that form in the CNT network in response to stretching.

The effects of infusion and polymerization of dicyclopentadiene polymer into a CNT a

yarn is discussed in chapter 5. This is work is from a publication in review with the

journal Carbon under the title "Fabrication and Characterization of Solid Composite

Yarns from Carbon Nanotubes and Dicyclopentadiene Polymer."   The nanotubes in this

specimen were characterized with Raman spectroscopy. The yarns without resin, with

uncured resin, and cured polymer are characterized mechanically for tensile properties.

The surface wetting of the nanotubes by dicyclopentadiene is observed. The structure

of yarns is determined with scanning electron microscopy and focused ion beam cross-

sectioning. The fracture surfaces are also characterized with scanning electron

microscopy. A capstan mechanism is introduced to account for the increased strength

of the composite fibers in comparison with the strength of the neat fibers without

polymer.

Chapter 6 investigates the load transferred to carbon nanotubes in composite sheets

made with various amounts of alignment achieved by stretching. The alignment is

characterized with wide angle X-ray scattering. The CNT material is characterized by

Raman spectroscopy and the CNT material, DCPD polymer and the composites are

characterized with thermal gravimetric analysis and dynamic mechanical analysis. The

specific mechanical properties of the sheet and composite, based on linear density, are

considered to reflect the stress carried by the carbon nanotubes. The increased stress

on the carbon nanotubes in the composite is attributed to kinking that enables load

transfer through a capstan mechanism. The amount increased stress applied to the

carbon nanotubes is then solved with the capstan equation to quantify the amount of

kinking in the bundles of nanotubes.

Finally chapter 7 provides concluding remarks about the results obtained in this

research. Then avenues for future research are suggested that will build on the present

findings and take the scientific body of knowledge closer to understanding the deformation and load transfer mechanism in carbon nanotube assemblies and composites.

CHAPTER 2: LITERATURE REVIEW OF CARBON NANOTUBE ASSEMBLIES

2.1 CARBON NANOTUBES

2.1.1 BONDING

Carbon forms bonds in three structurally different ways represented in Figure 2.1. The first is a linear structure with a carbon – carbon triple bond. The simplest molecule demonstrating this bond arrangement is acetylene which is shown in Figure 2.1a. This $C \equiv C$ bond has the highest bond dissociation energy of 201 kcal/mol and the shortest bond length of the three primary bonding types at 137pm [53]. The second bond type is a double bond with a simple molecular form of ethylene shown in Figure 2.1b. This $C = C$ bond forms planar structures where the four hydrogen atoms are in the same plane and twisting at the $C = C$ bond is prevented by π bonding. The angle between carbon bonds in this arrangement is 120° which effects the structures formed from this bond type. This bond has an energy of 146 kcal/mol and a bond length of 147 pm. Finally Figure 2.1c shows the structure of ethane which has a tetragonal structure with hydrogen atoms arranged 109° 28' away from the c-c bond. These have the lowest bond energy of 83 kcal/mol and the bond length of 154pm makes it the weakest of the three primary carbon bonds.

The different bonding schemes available to carbon is a result of the hybridization of its valence electrons. An individual carbon atom has the ground state electron

a

Acetylene

b

Ethylene

c
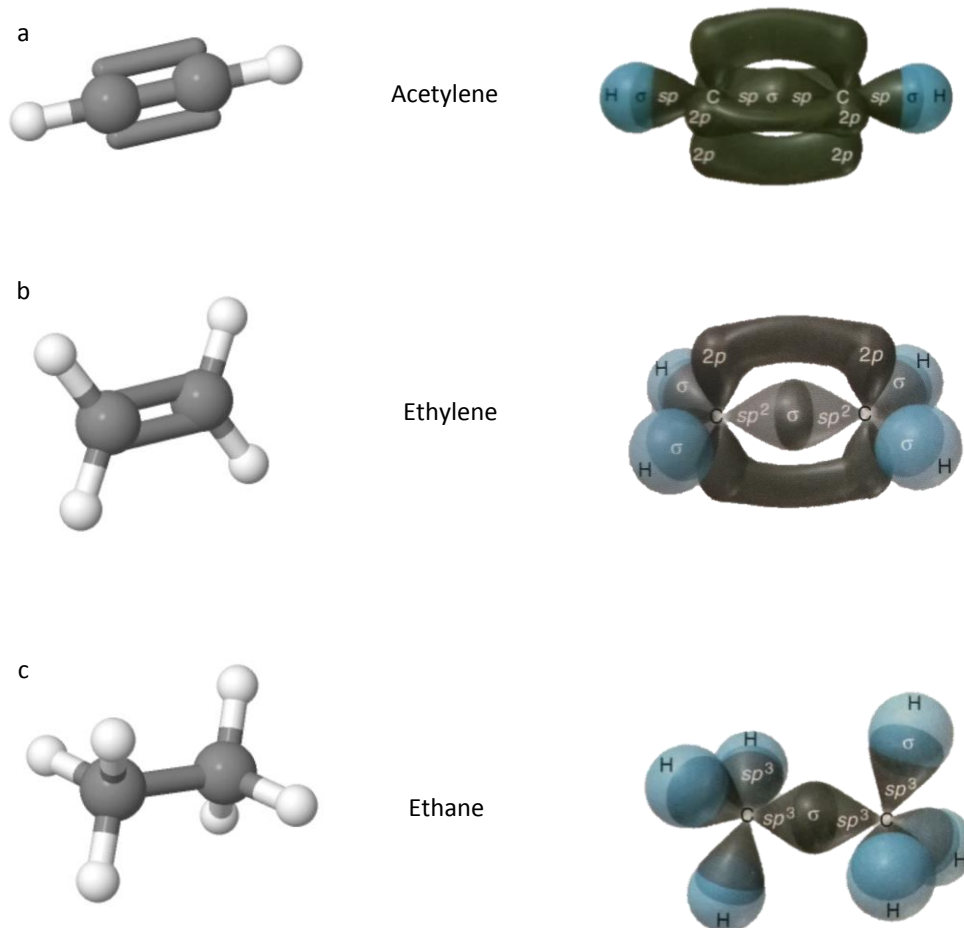
Ethane

Figure 2.1: Carbon bonding structures: a) Acetylene molecule showing C≡C triple bond forming a linear structure. b) Ethylene molecule showing C=C double bond forming a planar structure. c) Methane molecule showing three dimensional structure. The ball and stick structures were drawn with Jsmol (www.molecular-networks.com) and the orbital diagrams were adapted from [54]

configuration shown in Figure 2.2a where the 2s orbital is filled and two of the 2p

orbitals have a single electron. This valence structure means the Carbon atom needs to

find four more electrons to fill its valence and stabilize its energy. However, carbon has

the ability to mix its s and p orbitals to form a hybrid sp orbital. This process is shown

schematically in Figure 2.3 where the spherical s orbital combines with the dumbbell p

orbital to make a skewed dumbbell sp orbital where the amount of skew changes based

on the amount of s orbital character in the bond. This is based on the number of p

orbitals that mix with the s orbital. From the stand point of orbital energy this process is

favored because it lowers the energy of the system.

When two carbon atoms bond they form a strong sigma bond that holds the carbons

together and, depending on the hybridization, there can be additional bonding from the

formation of π bonds between the p orbitals of the carbon atoms. These π bonds add

some more attraction between the carbon atoms making the bond stronger.   This

partnership is why the sp^1 acetylene bond stronger than the sp^2 ethylene bond which

stronger than the sp^3 bond. Additionally the π bonds prevent rotation around the σ

bond which causes ethylene to be a planar molecule.

The π bonded electrons also play a major role in the properties of carbon materials,

as they grow into large molecules. In a molecule with multiple π bonds in close

proximity, like benzene, the electrons delocalize as shown in Figure 2.4b. This means

the electrons are not held between specific carbon atoms which allow them to move
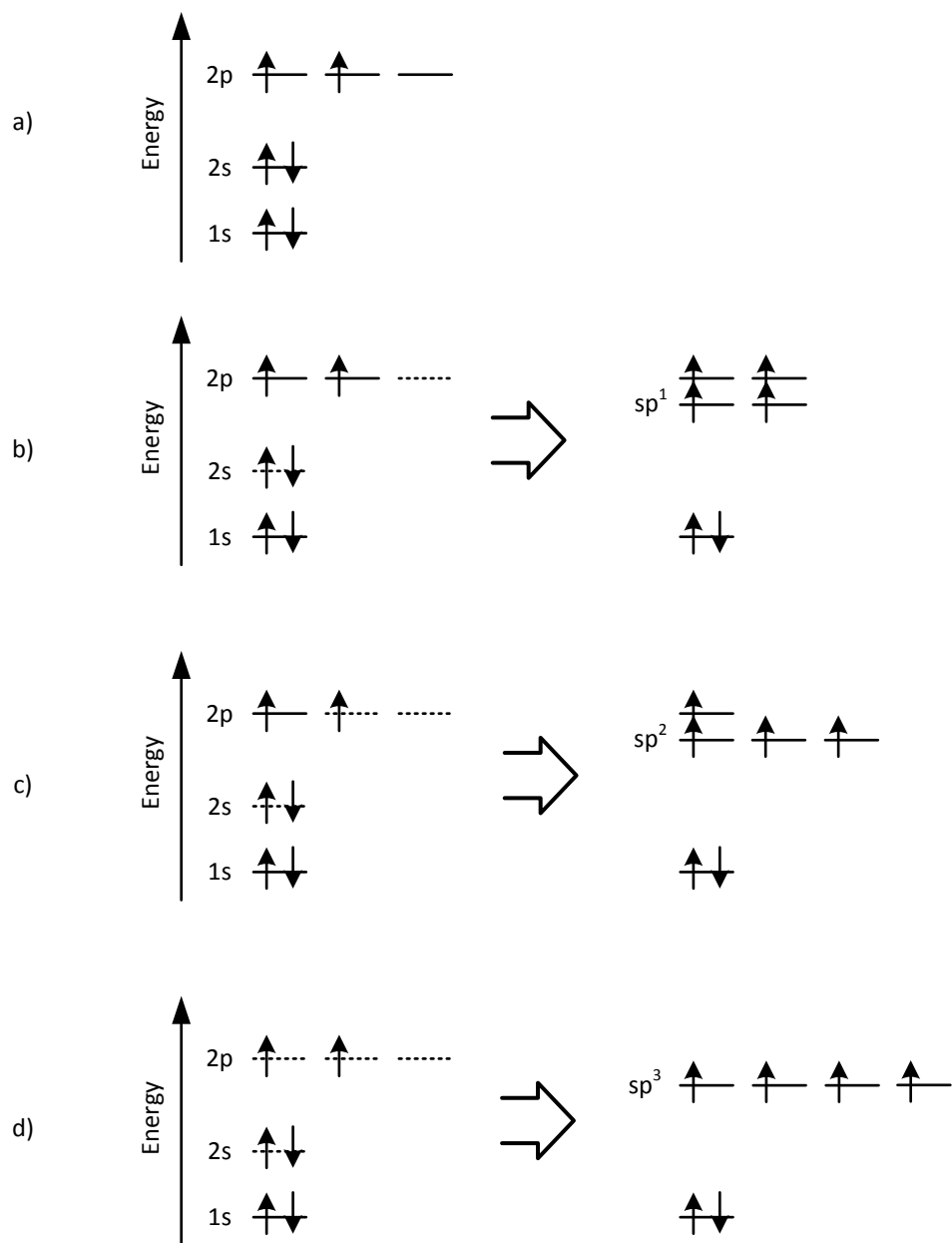
Figure 2.2: Carbon hybridization of electron orbital energy: a) Isolated carbon. b) sp^1 hybridized carbon. c) sp^2 hybridized carbon. d) sp^3 hybridized carbon. The dashed lines on the left diagrams show which orbital are used to form the sp hybrid orbitals.
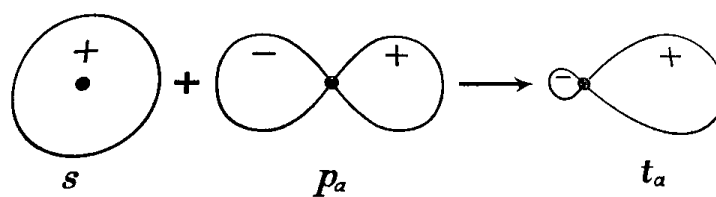
Figure 2.3: Hybridization of S and P orbital: The spherical s orbital hybridizes with a dumbbell shaped p orbital to form a hybrid sp orbital with a skewed dumbbell shape. Adapted from [53].

a

Benzene

b

Delocalization

c
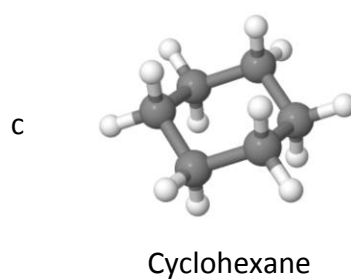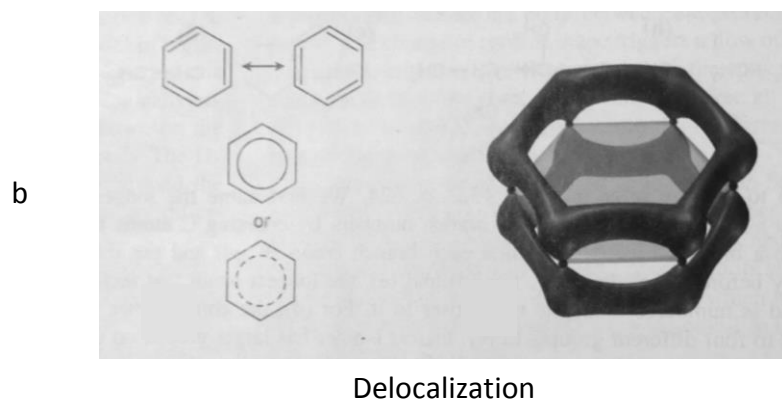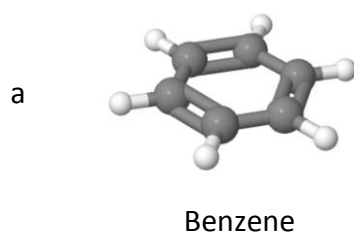
Cyclohexane

Figure 2.4: π orbital delocalization: a) Benzene molecule with three localized π bonds b) Delocalization of π bonds in benzene [54] c) Cyclohexane with sp^3 carbon bonding

freely around the molecule. As the size of the molecule increases, as in the case of

graphene (Figure 2.5b), this freedom manifests as electrical conduction, Figure 2.5b.

The opposite case is that of cyclohexane (Figure 2.4c) where the molecule is made up of

6 carbon atoms in a ring but with sp^3 hybridization. No p orbitals are available, as a

result of the hybridization, so there is no conduction of electrons. As this structure

grows larger, as in diamond shown in Figure 2.5c, it will be non-conducting.   However,

because both structures have strong C-C bonds, phonons can readily travel through the

material, producing thermal conductivity. The sp^1 bond in acetylene can also be

extended into larger structures. This is seen in carbyne (Figure 2.5a) which consists of

sp^1 hybridized carbon atoms that form a chain that is theorized to be the strongest

allotrope of carbon [55-57]. The π bonds delocalize and this chain of carbon atoms is

conductive both electrically and thermally [58, 59].

Of interest to the present research is the defects that occur in a graphitic structure.

Vacancies are the most straightforward (Figure 2.6a) and they result in holes in the

structure that will decrease the strength as they act as stress concentrators [60]. In

addition to this, the vacancies result in dangling bonds or a distorted network that act as

scattering sites for electron and phonon conduction [61]. Another common defect is

the Stone—Wales defect shown in Figure 2.6b [60]. In this case, when the graphene

sheet is stressed a C=C bond can rotate 90° creating strained group of 5 and 7 member

rings. In addition to these defects, carbon atoms within the graphitic plane can also

a   Carbyne

b   Graphene
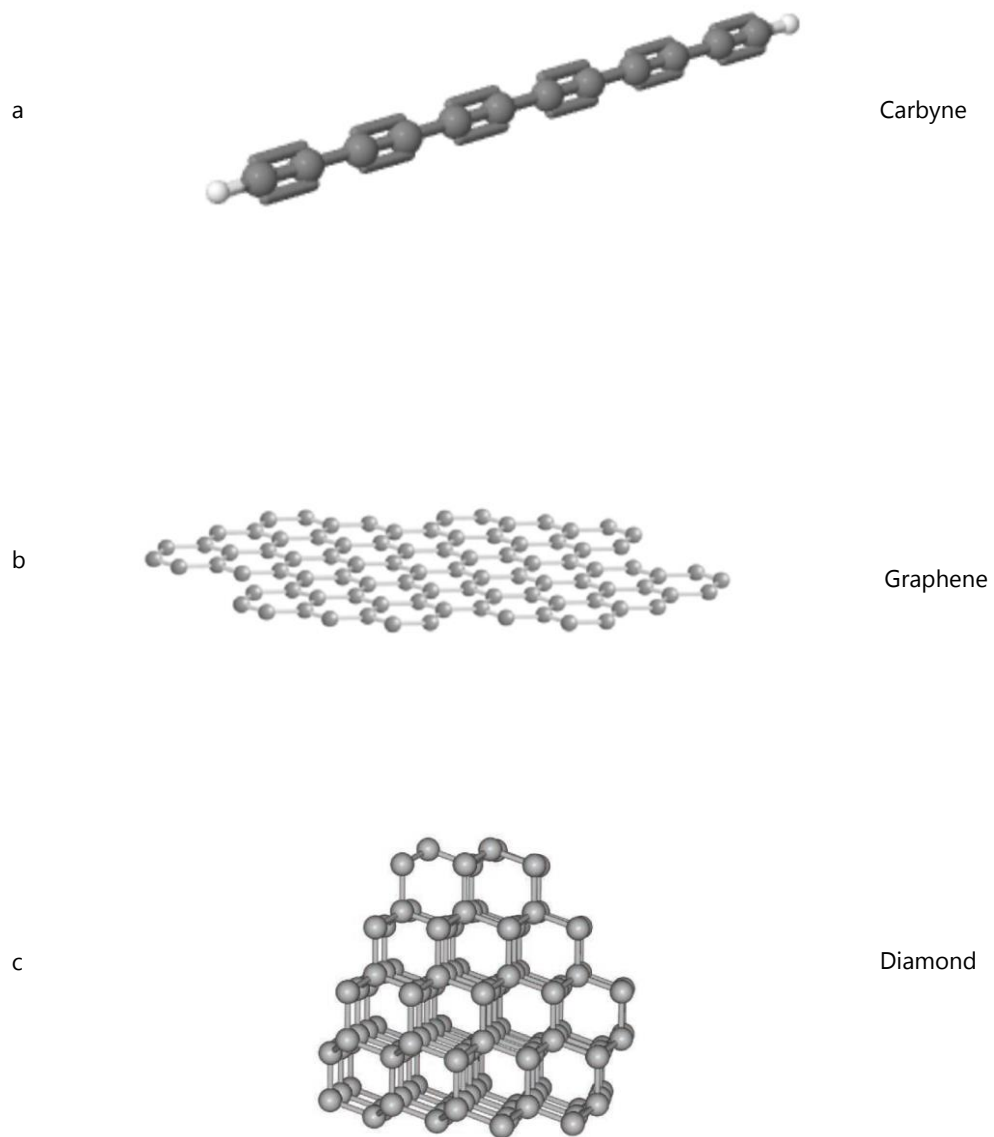
c   Diamond

Figure 2.5: Carbon structures. a) Linear chain of sp^1 bonded carbon (carbyne). b) Two dimensions sheet of sp^2 bonded carbon (graphene) [62]. c) Three dimensional structure of sp^3 bonded carbon (diamond) [63].
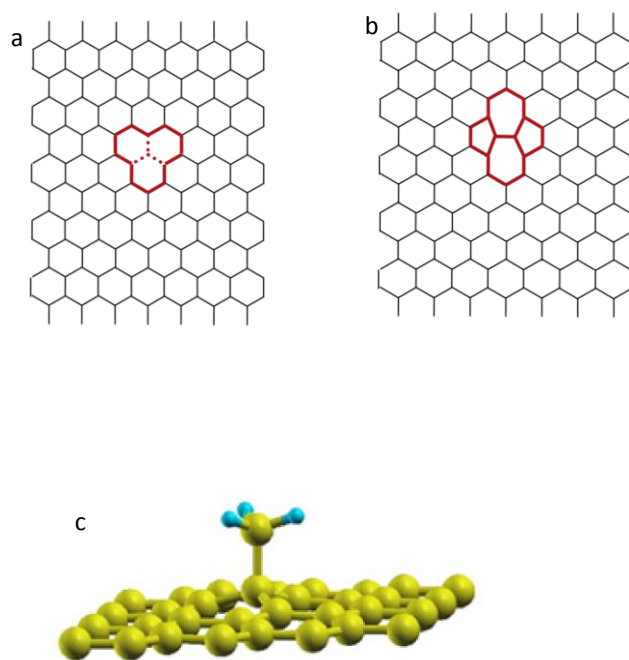
Figure 2.6: Defects in graphitic structure. a) Vacancy [60]. b) Stone Wales 5-7 defect [60]. c) In plane sp^3 hybridized carbon atom [61].

have sp^3 hybridization, as shown in Figure 2.6c. Here the carbon atom is attached to a methyl group. This defect also alters the local electric and thermal properties [61].

Finally an important aspect of expanding individual carbon bonds into larger scale structures is the effect of van der Waals (VDW) forces. Specifically this is of great importance to the adhesion of multiple layers of graphene into a repeating hexagonal close packed arrangement of graphite. This weak VDW bonding has another important provides very little shear strength between graphene layers [64, 65]. This week bonding means that bulk graphite has dramatically different properties in and out of the graphitic plane. The thermal expansion of graphite out of plane is 2.7 x 10^{-5} K^{-1}. The in plane expansion is -1.3 x 10^{-5} K^{-1} [66].

2.4.2 STRUCTURE

A carbon nanotube is a cylindrical structure that resembles a ribbon of graphene rolled into a tube. Figure 2.7 shows the structure of carbon nanotubes. A single walled carbon nanotube (SWNT) is shown in Figure 2.7a where a single sheet of graphene has conceptually been wrapped to form the tube. In Figure 2.7b a multiwall carbon nanotube having multiple graphitic planes arranged concentrically is shown. The spacing between these walls is approximately 3.4Å [67] as the graphene sheets cannot align into perfect AB stacking like graphite, but instead the spacing resembles turbostratic graphite [68]. Occasionally the multiwall nanotubes can share the same helical arrangement of carbon atoms [69]. There are also other naming mechanisms

16
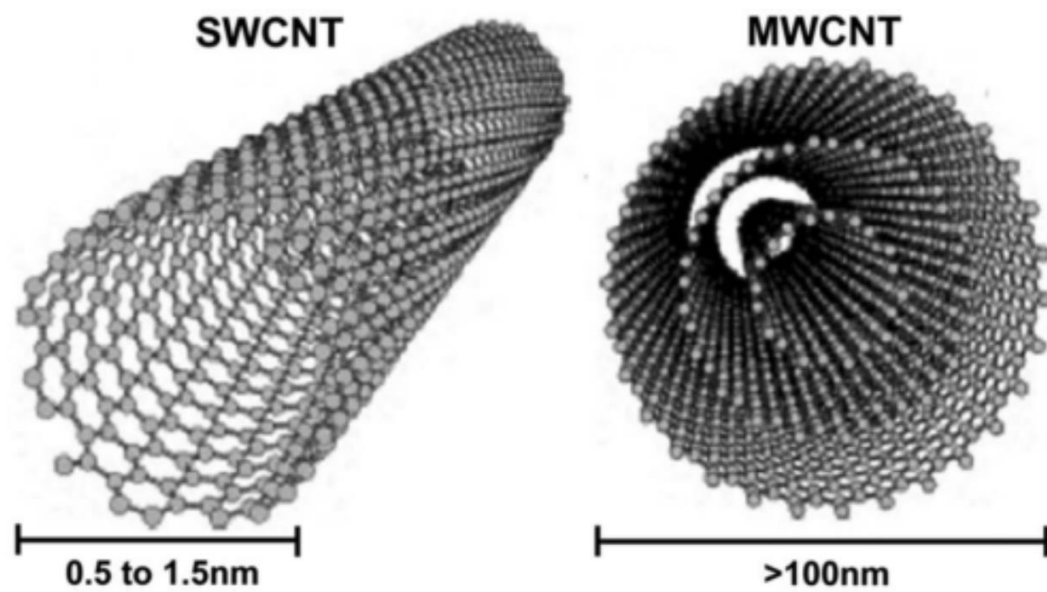
Figure 2.7: Carbon nanotube structure. a) Single wall nanotube. b) Multiwall nanotube. Adapted from [70].

used for more specific arrangements like dual wall (DWNT) for a multiwall nanotube

with two layers or few wall nanotube (FWNT) for tubes that have approximately 3-10

walls.

The arrangement of atoms around a carbon nanotube can have a substantial effect

on the properties. Figure 2.8 shows the chirality (helical arrangement) of CNTs with two

special cases being the armchair arrangement in Figure 2.8a and the zigzag arrangement

in Figure 2.8b. Figure 2.8c shows a chiral nanotube with the atoms arranges in a helical

manner between armchair and zigzag. These chiralities are enumerated with a method

using indices n and m for the lattice indices of a graphene sheet at the tail and tip of a

vector that describes the circumference of a nanotube. Figure 2.9 shows how this

indexing works. The region with the dashed box in Figure 2.9a is a single unit cell in the

graphene sheet. By shifting this unit cell along the a_1 and a_2 vector directions it is

possible to describe any position in the graphene sheet. In Figure 2.9b the nanotube

circumference is the **A** vector direction and the vector **T** points along the nanotube axis.

The vector $C_n = na_1 + ma_2$ starts and ends at the point where the graphene sheet fuses to

form a tube. Therefore the tip and tail of the C_n vector are the same atom.

This chirality has minor effect on the mechanical and thermal properties of the

carbon nanotube but it has a large effect on the electrical properties. The cylindrical

structure of the nanotube causes it to behave like a graphene ribbon and therefore

electronic wave functions are confined [71].   The energy bands consist of cuts through

18
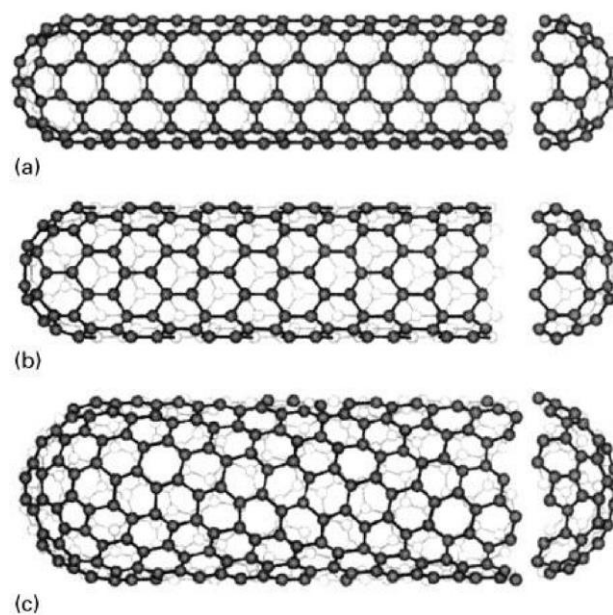
Figure 2.8: Chirality of carbon nanotubes. a) Arm Chair (5,5). b) Zig-zag (9,0). c) Chiral (10,5). Adapted from [72].
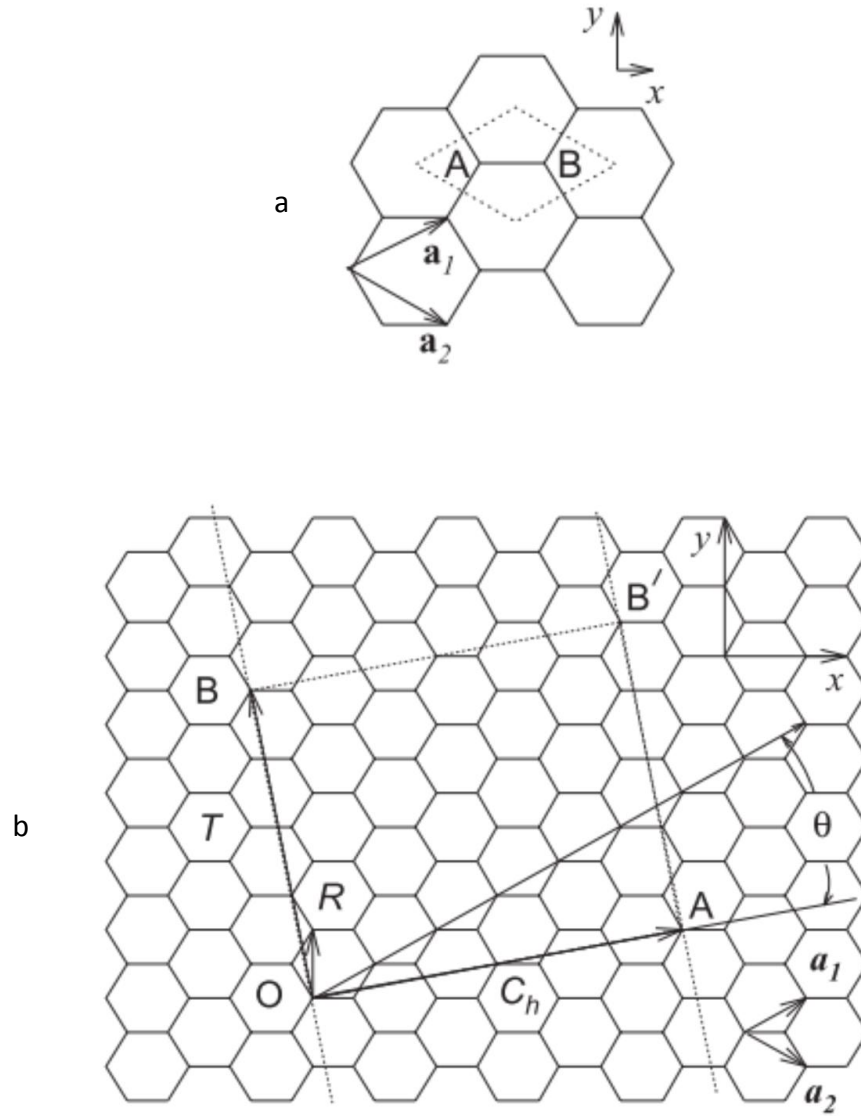
Figure 2.9: Defining chirality in nanotubes. a) The unit cell of graphene b) The chiral vector for a (4,2) nanotube overlaid on a graphene sheet. Adapted from [73].

the energy contours of the two dimensional dispersion relations of graphene, Figure

2.10. Depending on the orientation of **Cₙ**, the electronic structure does or does not align

with the K edge of the BZ of graphene. These cuts through the Brillouin zone are either

at the K point (Figure 2.11) where the π and π* energy bands are degenerative and

there is no band gap or it cuts on either side producing a band gap [74]. The tubes that

are aligned with the K corner and have no band gap therefore conduct metallically by

thermal excitations. Orientations of **Cₙ** that do result in cuts at the zone corner are

semiconducting and have a band gap depending on the tube diameter, Figure 2.11.

There are only 3 possible arrangements thus one third of carbon nanotube are metallic.

The determination of this metallic state depends on the indices according to the

equation referenced from [75]:

$$|n - m| = \begin{cases} 3q \; ; q \neq 0 \rightarrow Metallic \\ 3q \pm 1 \; ; q \neq 0 \rightarrow Semiconducting \end{cases}$$

(2.1)

Though the band gap grows as the tube diameter shrinks these rules breakdown when

the nanotubes reach very small diameter.   As the tube diameter shrinks, the distortion

of bonds by the high curvature means that the energy bands shift into the

semiconducting energy gap to make very small nanotubes with semiconducting
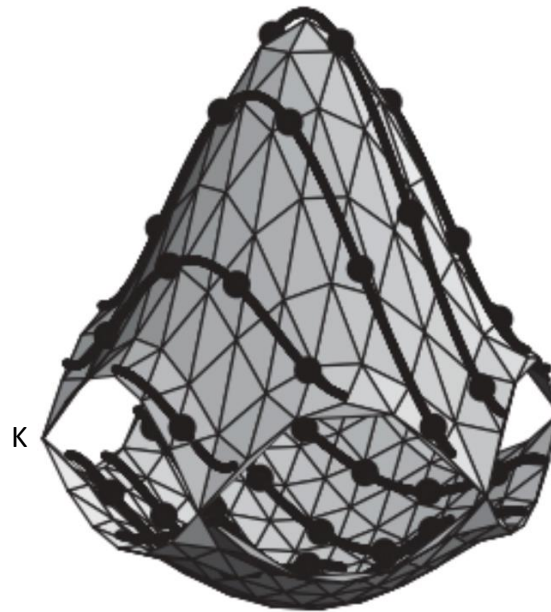
Figure 2.10: Energy contours for CNTs. Calculated energy for valence and conduction bands of the first Brillouin zone. The bands touch at the K point and the lines correspond to cutting for a (4,2) nanotube. Adapted from [73].
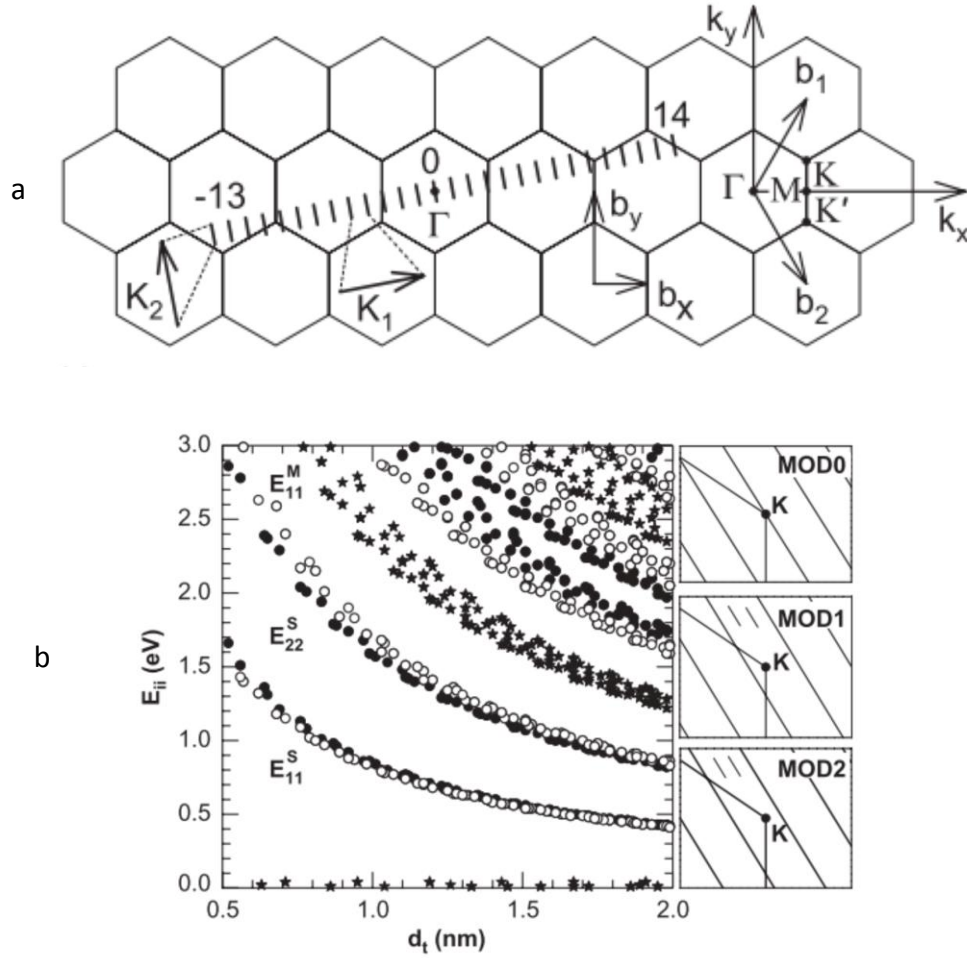
Figure 2.11: Nanotube K space: a) Lines representing the cut in a (4,2) nanotube drawn over the extended Brillouin zone. Where the cut lines cross the BZ determines if CNT is metallic of semiconducting. b) The left chart shows the electronic transition energies based on tube diameter. The right charts shows schematics for where the BZ is cut. MOD0 are metallic and cuts cross the K point. MOD1 and 2 are semiconducting and do not cut the K point. Adapted from [73].

chiralities behave metallic [76, 77]. Conversely, as the nanotube diameter increases the band gap is reduced, but it does not go to zero as bilayer graphene has a band gap [78].

Carbon nanotubes form the same ring defects as graphene but the constrained structure produces interesting shapes. Dumitrica et al. [79] showed that the chirality of carbon nanotubes plays a role in plastic deformation. An armchair nanotube is likely to form stone wales defect and therefore result in plastic deformation. This is opposed to zigzag nanotubes where the Stone-Wales formation is less probable due to the bond orientation. Instead, the carbon bonds break and the nanotube fails in a brittle manner. Figure 2.12a shows a CNT that is placed under strain. The bonds that are oriented along the tube axis (blue) are prone to brittle failure. Bonds oriented perpendicular to the tube axis are prone to thermally activated rotation to form a 5-7 Stone-Wales defect. This plastic deformation can go further in the splitting of the Stone Wales defect and the traversing of the nanotube in a spiraling fashion to increase the tubes length and reduce its diameter, Figure 2.12b. If the 5 and 7 member rings are arranged opposite of each other, a kink is formed in the tube, as shown experimentally and schematically in Figure 2.12c. If there are several defects arranged in a regular pattern the nanotubes can even form a helical structure as shown in Figure 2.12 d and e.

The graphitic structure of carbon nanotubes means that they adhere to neighbors through VDW forces. This VDW attraction is shown nicely in Figure 2.13a and c where SWNTs have agglomerated into a hexagonally packed bundle. When intermediate size

24
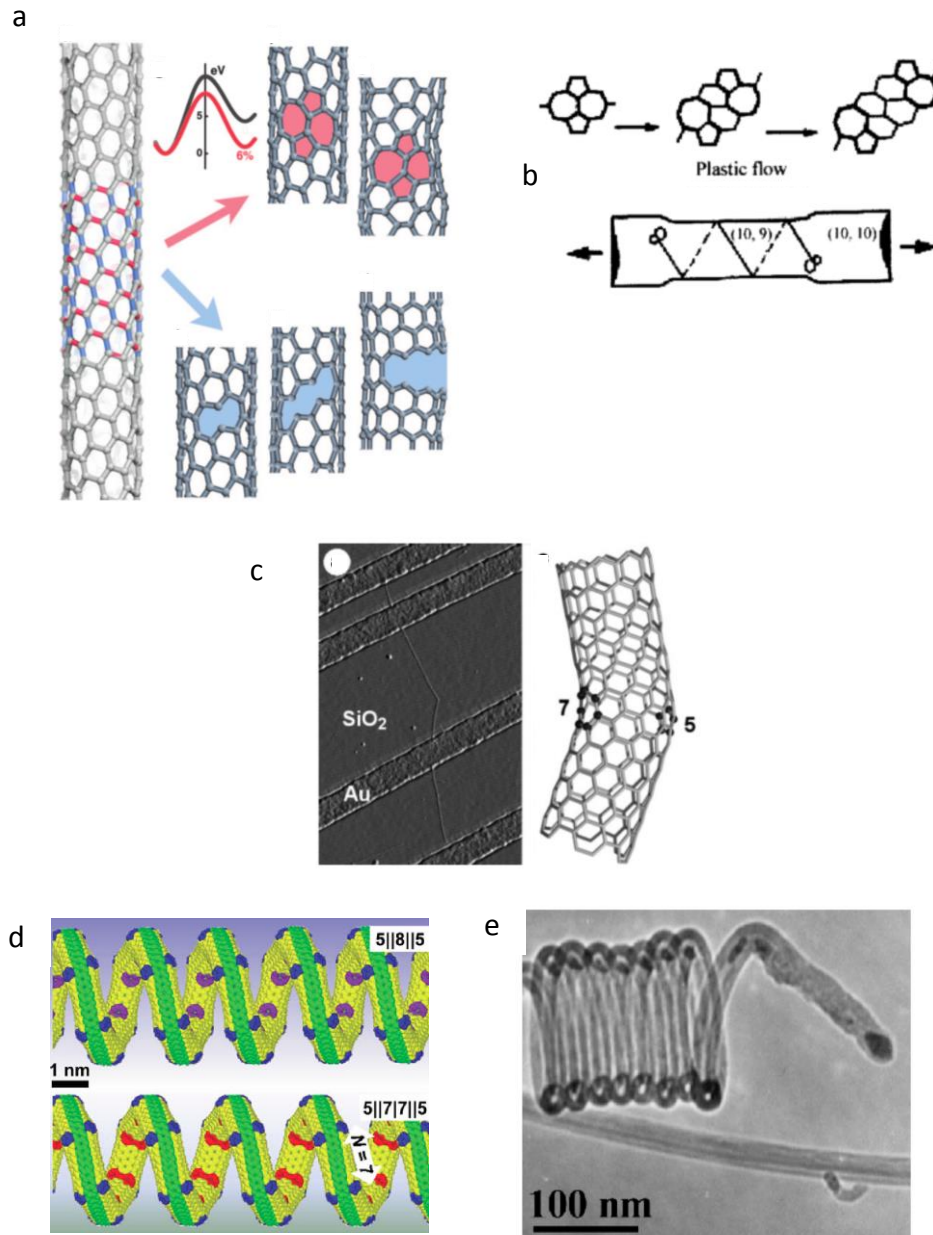
Figure 2.12: CNT Defects. a) Stress induced formation of defects under 15% strain. Red regions are susceptible to plastic deformation by bond rotation at elevated temperature while blue regions see brittle breakage at low temperature [79]. b) Plastic flow of stone wales defect increases CNT length and reduces diameter [80]. c) Opposed 5-7 defects produce kink in CNT with micrograph on left and schematic on right [81]. d) Ordered arrangement of 5/8 and 5/7 defects produce a helical structure [82]. e) Observation of helical multiwall nanotube in TEM [83].
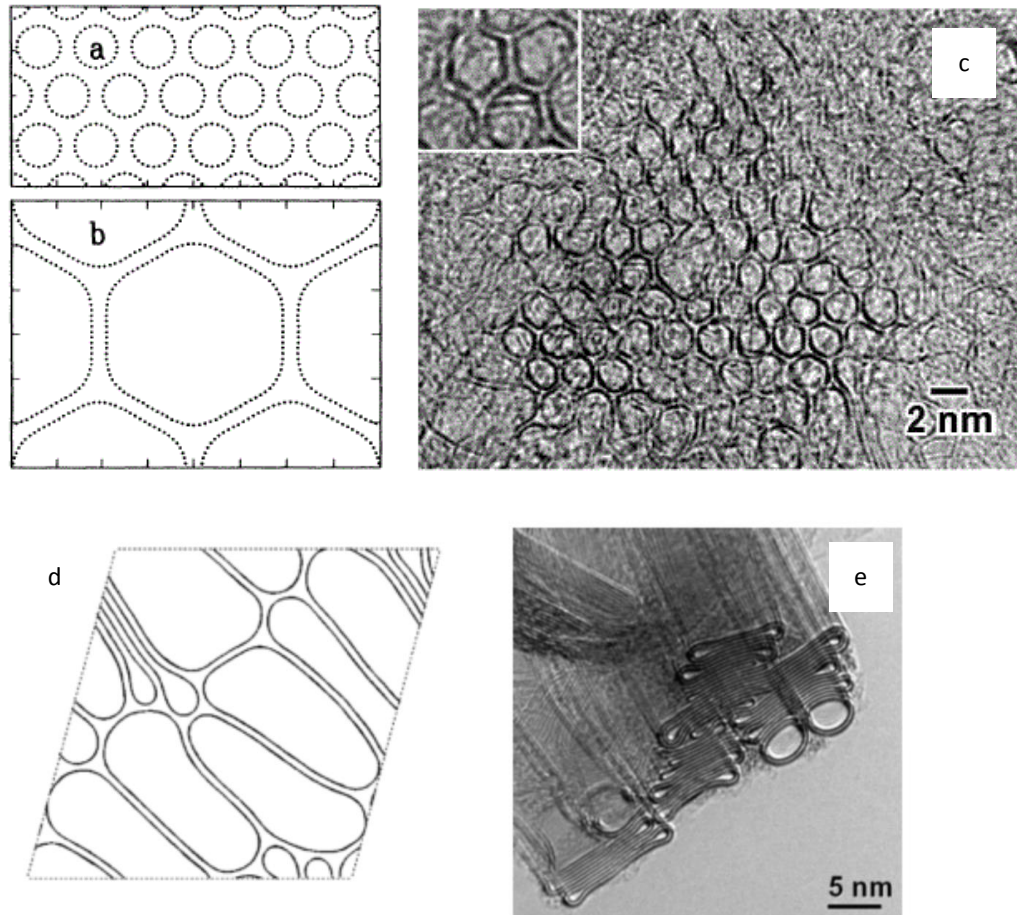
Figure 2.13: Flattening of CNTs in bundles. a) Bundles of 1nm nanotubes were modeled and wall collapse was not observed. b) A bundle of 4nm nanotubes showed substantial wall flattening [84] c) TEM of a SWNT bundle demonstrating wall flatting in the inset [85] d) Model of collapse in large diameter and few wall nanotubes [86] e) Micrograph of collapse in large diameter and few wall nanotubes [87].

nanotubes come in contact they tend to flatten at the contact points as shown in Figure

2.13b [84]. Elliot 2004 et al. [86] showed that as the diameter of carbon nanotubes

increases the pressure needed to collapse the tube from a circular cross-section into a

dog-bone decreases. Eventually the nanotube become unstable and collapse by the

mutual VDW attraction of the opposing CNT walls, Figure 2.13d and e. For single wall

nanotubes this instability occurs around 2.2 nm [86]. This effect is important because

the collapsed tubes expose more surface area to their neighbors. This increases contact

area and thereby increases shear strength. This effect is also important for the analysis

of CNT lattice spacing by X-ray diffraction [88].

    Carbon nanotubes also form interesting structures under severe deformation. When

a single walled nanotube is bent it eventually kinks like that shown in Figure 2.14a [89].

The kink also forms a radial compression that flattens the tube regardless of the original

diameter but this is radius specific as larger diameter nanotubes are more prone to

flattening [86, 90]. Therefore in a bundle of nanotubes some may flatten in response to

bending while smaller diameter tubes may remain round. Another interesting response

to bending can be seen in Figure 2.14b for a MWNT [91]. In this case the many walls of

the tube prevent and outright collapse of the tube diameter. Instead, the walls on the

compressive side of the bend begin to buckle, forming a corrugated pattern. This could

have an impact on properties because it could cause defects to form within the
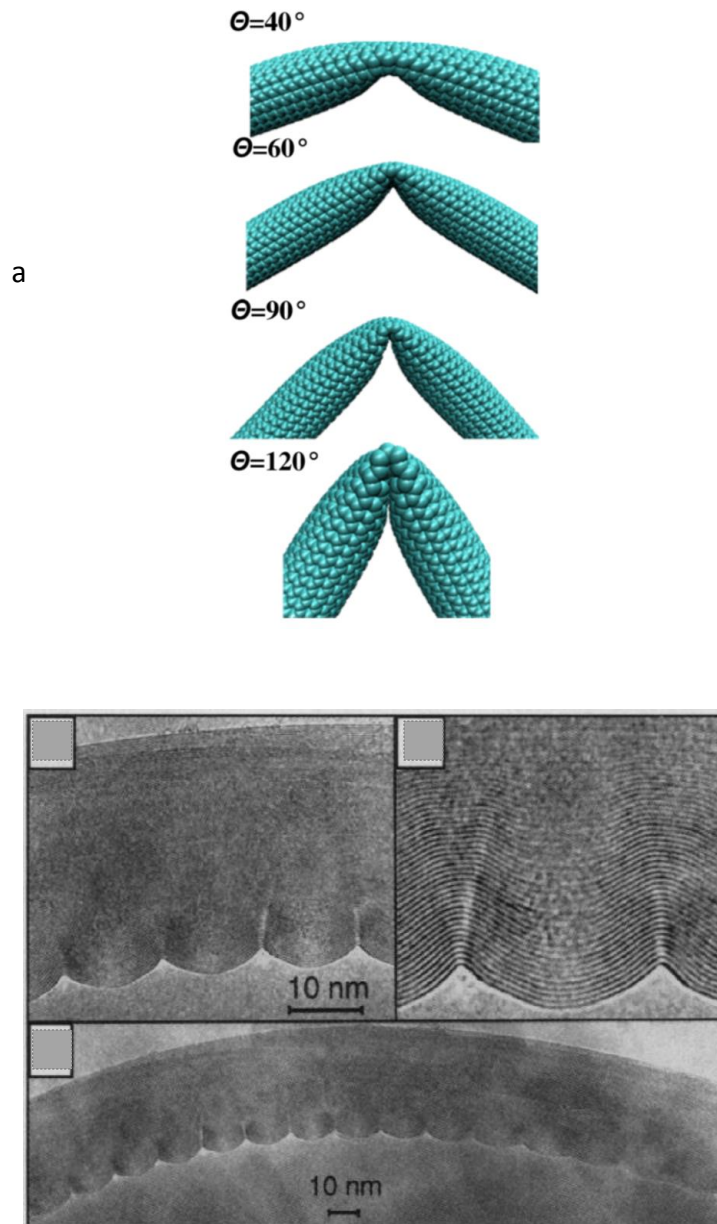
Figure 2.14: Structure of bent CNTs. a) SWNT subjected to bending that results in a collapsed cross-section [89] b) Bending in a MWNT resulting in buckling of the side wall [91].

structure. Also this kind of feature would resist sliding around a curved surface by

mechanical interlocking.

2.1.3 PROPERTIES

With the structure of carbon nanotubes described in the previous section it is now

useful to discuss the properties of isolated carbon nanotubes. The strength of carbon

nanotubes has varied widely between single walled, few walled and multi walled

nanotubes. However Qian et al. [92] did a good job reviewing the mechanical properties

of CNTs. There are a wide range of mechanical properties as defects, diameters and, to

a lesser extent, chiralities all play a role. However with that being said the modulus of

an individual nanotube is approximately 1 TPa [93-95] which is in the vicinity of single

crystal graphite at 1.06 TPa [96]. The strength of carbon nanotubes, on the other hand,

varies widely. Ding et al. [97] observed strengths between 10 and 66 GPa with an

average of 24 GPa. The modulus varied between 0.6 and 1.2 TPa with an average of 0.9

TPa. Elongation at failure ranged between 1% and 6.3% with an average of 2.6%. Yu et

al. [11] observed strengths between 11 and 63 GPa, modulus between 270 and 950 GPa

and elongation up to 12%.   The theoretical limit for elongation to failure is

approximately 20% [98, 99]. In [10] the strength of a SWNT was measure directly in

tension with a microelectromechanical systems attached to a TEM sample holder.

Considering the entire cross-sectional area of the nanotube, the stress reached 150 GPa.

Zhang et al. [100] formed long continuous carbon nanotubes and tested there tensile

strength by blowing a gas over the surface to produce tension though viscous drag. Calculations determined by considering only the outer most shell carrying load gave a breaking strength of 200 GPa. The strain at failure reached up to 17.5% and the young's modulus of 1.34 TPa.

Individual carbon nanotubes also have respectable thermal, electrical and optical properties. The theoretical thermal conductivity of a (10,10) CNT, based on molecular dynamics, is estimated at nearly 6600 W/m/K [101]. The measured thermal conductivity of a SWNT and MWNT have been established at 3500 and over 3000 W/m/K, respectively [7]. This exceeds the measured thermal conductivity of natural diamond at 2230 W/m/K and even exceeds the conductivity of C^{12} isotopically purified diamond at 3320 W/m/K [102]. However the introduction of defects into the carbon nanotube will rapidly reduce this thermal conductivity because a single defect accounts for such a large fraction of the cross-section. Jiang et al. [103] showed the thermal expansion of nanotubes is negative at low temperatures and at room temperature but this transitions to positive values around 400 K. These researchers also showed that as the diameter of the nanotubes decreases the extent of this negative thermal expansion also decreases. Interestingly armchair nanotubes have a radial coefficient of thermal expansion (CTE) less than the longitudinal CTE however the opposite holds for zig-zag nanotubes. However, the radial CTE is independent from chirality angle and instead it is the longitudinal CTE that is related to chirality. Maniwa et al. [104] measured the CTE of

single wall nanotube bundles with X-ray diffraction and found that there was a -0.15±2.0 x 10^{-5} K^{-1} CTE for the tube diameter, a 0.75±0.25 x 10^{-5} K^{-1} CTE for the triangular CNT lattice and a 4.2±1.5 x 10^{-5} K^{-1} CTE for the distance between tubes which was larger than the C-axis CTE of graphite (2.6 x 10^{-5} K^{-1}).

Electrical properties depend on the type of carbon nanotube as 2/3 of chiralities are semiconducting. Carbon nanotubes have been shown to conduct ballistically [105-107] and the mobility has been estimated to have an intrinsic value of >100,000 cm^2/Vs [108]. This is exceptional because it exceeds the mobility of other semiconducting materials like silicon at <1000 cm^2/Vs. This gives CNTs appeal for application in high speed electronics. Additionally Frank et al. [109] demonstrated a stabile current density of >10^7 A/cm^2 by measuring the electrical properties of nanotube inserted into a liquid metal. Single wall nanotubes have been shown to have a resistance of 10^{-6} Ωcm and a Fermi velocity of 8 x 10^5 m/s [110, 111]. The band gap of carbon nanotubes has been shown to depend on the diameter of the nanotube where smaller nanotube have larger band gaps and between 0.6 nm and 1 nm in diameter the band gap ranges from 1150 meV to 750 meV, Figure 2.15. Unfortunately, the application of CNT into semiconductor devices and for that matter applications where electrical conduction is a concern is hindered by getting electrons to enter and exit the CNT across the 3.4 Å VDW bond. Chen et al. [112] was able to form ohmic contacts with tungsten but it required welding.

Kim et al. [113] demonstrated that ohmic contacts could be formed on semiconducting

nanotubes
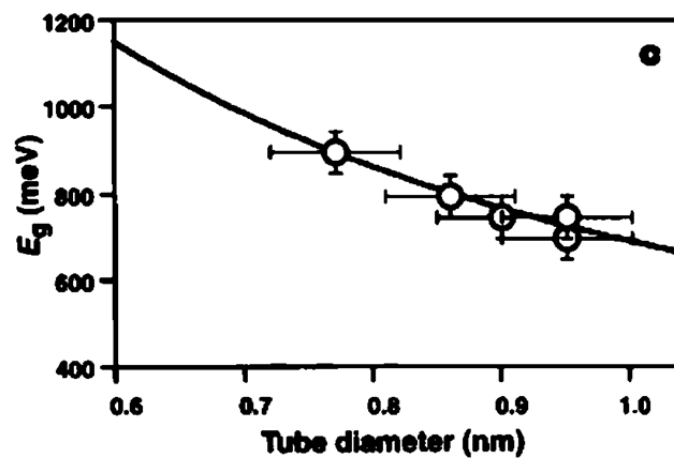
Figure 2.15: Diameter dependence of CNT band gap. Adapted from [114].

with rhodium and palladium when the diameter was greater than 1.6 nm but schottky

contacts were formed when the diameter was less than 1.6 nm. They also found that

ohmic contacts were hard to form for metallic nanotube less than 1 nm in diameter.

The optical properties of carbon nanotubes are a direct result of the electronic

structure of carbon nanotubes [73]. One of the most widely utilized optical property of

carbon nanotubes is the Raman effect where light is inelastically scattered by

interaction with molecular vibrations. An example of a Raman spectrum from a carbon

nanotube is given in Figure 2.16a [115]. In this spectrum there are three radial

breathing mode (RBM) peaks (marked with asterisks), the D peak for disorder induced

dispersive modes, the G peak for the in plane tangential vibration of carbon atoms and

the G' band which is the second order harmonic of the D band.   The radial breathing

modes are considered to be frequencies below 500 cm^{-1} and can be utilized to

determine the diameter of the corresponding nanotubes with the relationship of

$\omega_{RBM}=248/d_t$ [116]. The D band is at approximately 1350 cm^{-1}, the G band is between

1550 and 1605 cm^{-1} but usually its peak is at 1585 cm^{-1}, and finally the G' band is at

approximately 2700 cm^{-1}. Mechanical strain in the CNTs is often correlated to shifts in

the G' band [117, 118]. The other optical property of carbon nanotubes is their

florescence in the region of 800 to 1600 nm which is within the useful wavelength range

for fiber optics and biological imaging [119]. The 875nm emission from one of these

samples with excitation wavelengths between 250 and 650 nm is shown in Figure 2.16b.
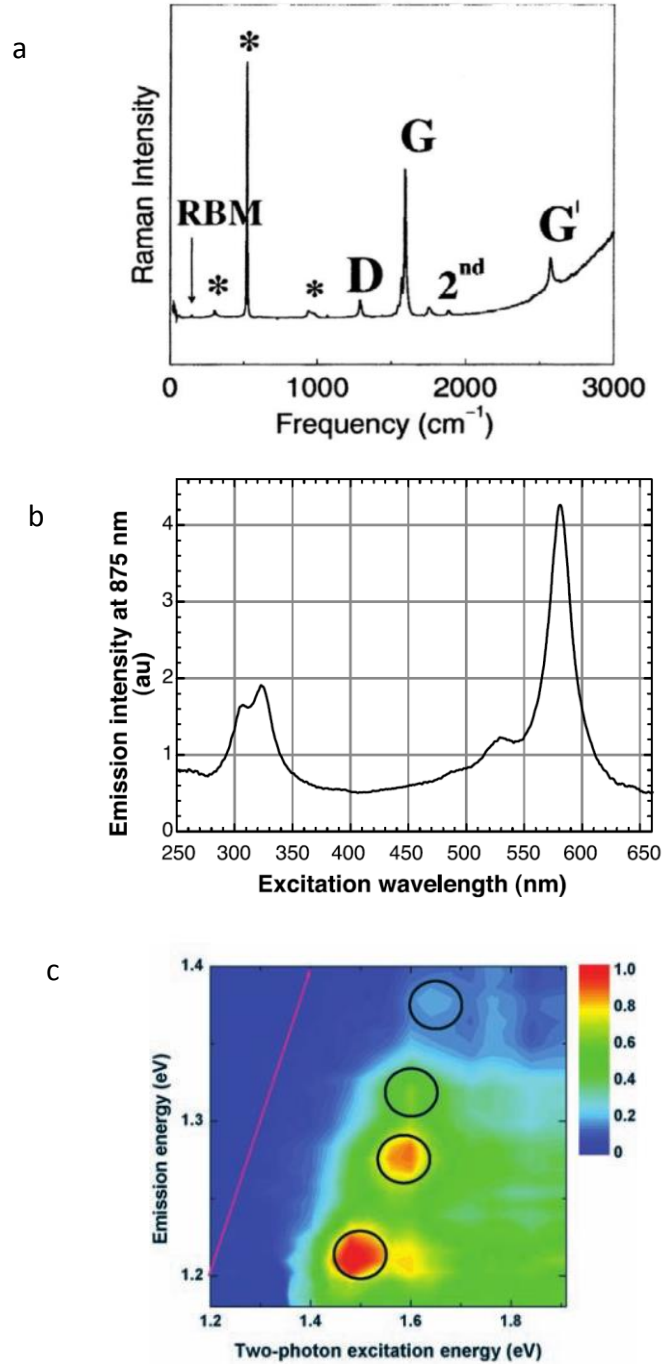
Figure 2.16: Optical Properties of CNTs. a) Raman spectrum from carbon nanotubes [115] b) Single fluorescence excitation spectrum for nanotubes [119] c) Contour plot of two photon excitation spectrum with emission for nanotubes circled [120].

These florescence emissions are a result of optically excited states that result from excitons [120]. Because the emissions are structure specific, excitation spectroscopy is possible. Photo excitation and emission data is shown in Figure 2.16c. Where the solid line at the left indicates where one photon absorption falls and the four circles correspond to (7,5), (6,5), (8,3), and (9,1) nanotubes.

Chemically the surface of carbon nanotubes is inert due to its graphitic structure but there are interesting interactions the nanotubes have with their surroundings. Zhang et al. [121] investigated the surface wetting of suspended carbon nanotubes by various metals deposited by electron beam evaporation. They found that titanium formed continuous films while nickel and palladium formed films with occasional gaps. This contrasted with gold, aluminum and iron which formed particles on the suspended CNTs. The binding energies with the carbon nanotubes were ranked as Ti > Ni > Pd > Fe > Al > Au. Collins et al. [122] investigated the sensitivity of carbon nanotubes to oxygen containing environments. They found that exposing the surface of carbon nanotubes to oxygen rapidly reduced the resistance of nanotubes and that the thermoelectric power varied linear with oxygen concentration. Although the oxygen physisorbed to the CNT, it could not be removed from the carbon nanotubes without heating, even with vacuum. The researchers had to heat the tubes between 110 °C and 150 °C to remove the oxygen. When exposed to oxygen above 200 °C they observed oxygen chemisorption. The reduction in resistivity with physisorbed oxygen was attributed to localized

increases in the density of states. There was a 0.3 eV band gap when clean and the DOS

was filled after oxygen exposure. They also observed that small band gap nanotubes

were more sensitive to oxygen exposure. The effect of the local electrical properties of

carbon nanotubes being effected by the interaction with the surrounding environment

is utilized for bio sensors. Rahman et al. [123] placed carbon nanotubes on top of gold

electrodes and coated the nanotubes with glucose oxide, forming electrolytic cells. The

glucose oxide interacted with glucose and, under a constant voltage, current changes in

the cell could be measured. There was a high sensitivity to the concentration of glucose

which was able to detect down to 1.3 µM and the response was linear with

concentration.

Finally the last topic to discuss for the properties of carbon nanotubes is the sliding

friction between tubes. Suekane et al. [124] studied the frictional sliding force between

a pair of carbon nanotubes in the arrangement shown in Figure 2.17. The apparatus

utilized an atomic force microscopy probes with CNTs attached to its tip, Figure 2.17a.

By pulling these apart the sliding frictional force could be measured directly, Figure

2.17c. This experiment was carried out in tow conditions the first where the tubes were

coated with residual amorphous carbon from the growth process, Figure 2.17e. In this

case the amorphous carbon acted like grit between the CNT surfaces and caused the

linear response of frictional force to overlap length of 0.07 nN/nm, Figure 2.17d.

Conversely when the carbon nanotubes were annealed to remove the amorphous
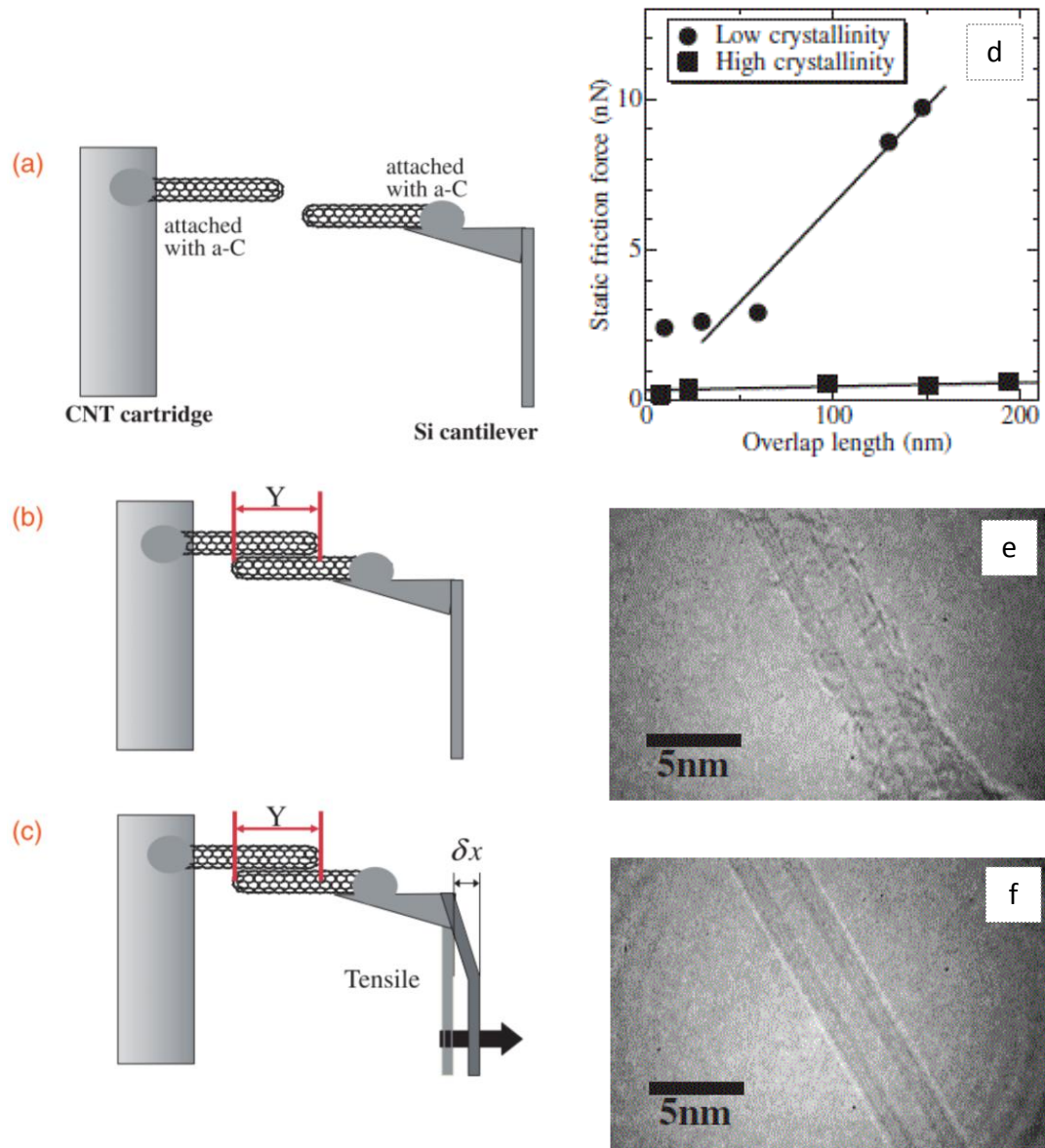
Figure 2.17: Static friction between CNTs. a) Arrangement for measuring static friction b) CNTs place into contact with a prescribed overlap c) CNT pulled to measure frictional force by cantilever deflection c) Graph of frictional force versus CNT overlap length for low and high crystallinity nanotubes e) TEM of low crystallinity nanotube f) Surface of high crystallinity nanotube. Adapted from [124].

carbon (Figure 2.17f) the friction dropped to 0.43 nN and it no longer showed an overlap dependence. This may have been a result of the loads being below detection. The researchers determined the friction force to be constant but if instead a frictional sliding force is fit linearly, with an intercept of 0 for no overlap length, the frictional sliding force could be estimated at ~0.0025 nN/nm.

2.2 CARBON NANOTUBE GROWTH

There are many methods used to grow carbon nanotubes like arc discharge, laser ablation, chemical vapor deposition, electrolysis and even pyrolysis. All the growth methods share some commonalities including a carbon source, a heat source, and a catalyst source that may not have been present in early growth methods but is now widely applied. Here the growth methods will be split into three groups. The first is high temperature methods including arc discharge and laser ablation where temperatures are high enough to vaporize graphite. The second group, chemical vapor deposition (CVD), is the broadest and the most applicable to the present research. Finally the third group is made up of miscellaneous approaches that are unique but have been less widely adopted.

2.2.1 HIGH TEMPERATURE GROWTH

The high temperature growth utilizes methods to evaporate carbon from graphite to rapidly produce carbon nanotubes. These methods tend to produce nanotubes with

high quality because the elevated temperature anneals the CNT structure so fewer defects remain in the nanotubes.

2.2.1.1 ARC DISCHARGE

The arc discharge method of carbon nanotube production has received significant attention since it was used by Iijima to discover nanotubes [3]. In this method two graphite electrodes are place in a vacuum chamber filled with an inert gas such as helium or argon at low pressures, Figure 2.18a. For example, Iijima used argon at 100 Torr for his first experiment. The graphite electrodes are placed collinearly with a small separation on the order of millimeters. A DC current is passed through the electrodes and an arc is formed. This high temperature arc, in excess of 3000 °C [40], vaporizes the graphite electrodes. Then carbon nanotubes and other carbonaceous species condenses on the negative electrode. The nanotubes are well formed but are coated with a hard grey shell. The nanotubes align approximately with the electric field but to isolate the nanotubes, the crust is removed and ground, then and dispersed in solvents with sonication. This forms a randomized solution of CNTs [76]. By controlling the inert gas atmosphere, gas pressure and voltage the yield and type of carbon species created can be controlled [125, 126]. The tubes that Iijima characterized in 1991 were multi walled with outer diameters of 6.7, 5.5 and 6.5 nm. Also, the nanotubes were approximately 1 μm long. This was improved upon by the addition of a catalyst to the cathode. Iijima and Ichihashi [6] used iron filings placed into a dimple in the cathode
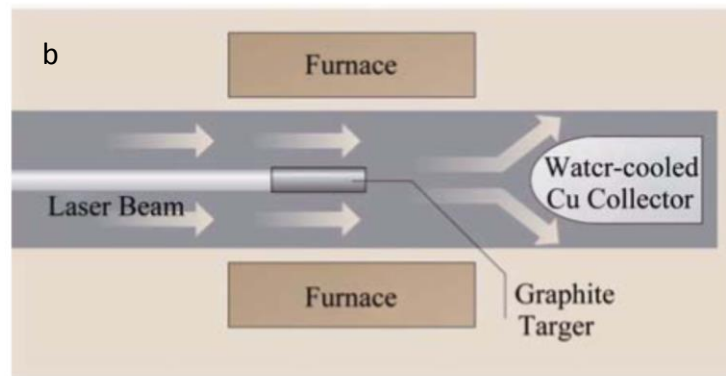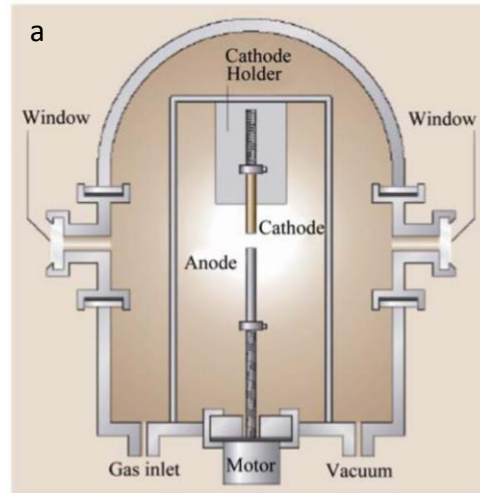
Figure 2.18: High temperature growth systems. a) Schematic for arc discharge growth furnace and b) schematic for laser ablation growth furnace. Adapted from [127].

and Bethune et al. [5] filled a hole, drilled in the cathode, with mixtures of iron, nickel or cobalt with graphite, finding that cobalt produced nanotubes. This catalyst reduced the diameter distribution of the carbon nanotubes grown. Iijima and Bethune found single wall tubes that ranged from 0.7 to 1.65 nm and Bethune et al. found ubiquitous 1.2 ± 0.1 nm SWNTs. Various transition metal catalyst metals can be used and Journet et al. [128] showed high specificity of SWNTs could be achieved by filling a hole in the anode with a mixture of 1 at% Y and 4.2 at% Ni mixed with graphite. However the total yield was 20%. The challenge with this approach is that the carbon nanotubes are found under a rigid crust that covers the negative electrode. This must be scrapped and collected before purification to retrieve the nanotubes. This means the process inherently generates unaligned nanotubes. Equipment has been suggested to increase the scale of CNT production by arc discharge where attachments are added to maintain electrode gap with linear motors [129] or to translate and rotate a large cathode [130] but the process is still performed in batches.

2.2.1.2 LASER ABLATION

The laser ablation process is a CNT growth method that was pioneered by the Smalley group to grow buckminsterfullerene's [1]. The use of the technique to produce carbon nanotubes was first demonstrated by Guo et al [131]. The system consists of a tube furnace with a flowing inert gas and a graphite target placed concentrically. The furnace is held at a temperature near 1000 °C, Figure 2.18c. A pulsed laser heats and

vaporizes the graphite target and, after CNT formation, a water cooled copper probe collects the nanotubes. This process also has demonstrated selectivity for single wall nanotubes with proper control of catalyst in the graphite target [132]. Furthermore, the process has been demonstrated to have some control over chirality [133-135]. However, this was not a recipe to produce a specific chirality but rather showing that the majority of nanotube formed had only a few specific chiralities instead of wide distribution. In Thess et al. [136] this method used a Co/Ni/graphite target placed into a heated tube furnace (1200 °C) with flowing argon. Laser pulses heated and vaporized the graphite target and the flowing gas carried the grown nanotubes to the collector. They achieved a 70%-90% yield. Like the arc discharge technique this method produces high quality nanotubes as a result of the high temperature vaporization of carbon that anneals out defects. However this processes has a low production rate, it is a batch process and it forms unaligned mats of nanotubes.

2.2.2 CHEMICAL VAPOR DEPOSITION

The chemical vapor deposition processes for growing carbon nanotubes relies on the thermal decomposition of carbon containing species at the surface of a catalyst. A carbon nanotube is then extruded into a tubular structure by the confinement that is imparted by the small catalyst particles. This growth mechanism was first suggested by Baker et al. [137] in the 1970's to explain the formation of carbon nanofibers. Jourdain et al. reviewed the growth mechanisms [138]. The CVD growth methods are widely

varied and there are many instances where the growth techniques are mixed. An

attempt is made to describe the methods that do not combine growth techniques, as

much as possible. Exceptions are made for instances where a specific structural

arrangement of carbon nanotubes is achieved as a result of the growth process. One of

these exceptions is for the CVD process of Nanocomp Technologies Inc. which is the

material supplier for the present work. Broadly the CVD growth process will be divided

into two categories. The first category looks at growth techniques that utilize supported

catalyst. In these methods an inert substrate holds the individual catalyst particles and

the interaction between solid, liquid and vapor controls the surface morphology of the

catalyst particle which therefore controls the structure of the growing carbon

nanotubes [139-141]. The second group contains methods with unsupported catalyst

that utilized the vaporization of metal inside a growth furnace or decomposition of

metalorganic molecules to form metal nanoparticles that float down a growth furnace

and nucleate the formation of carbon nanotubes.

2.2.2.1 SUPPORTED CATALYST

An early method of nanotube growth by CVD was performed with what is called a

fixed bed growth process. In this method an inert powder is coated with a metal

catalyst which is placed in a boat and positioned in a tube furnace. The flowing carbon

containing gas interacts with the catalyst and decomposes to form carbon nanotubes.

The yield of these processes is determined by weighing the powder before and after

carbon nanotubes have been formed. The supports are then typically removed from the

carbon nanotubes by dissolving in an acid bath. Colomer et al. [142] used cobalt, iron,

and Co/Fe alloy particles on top of magnesium oxide supports in a 1000 °C tube furnace

with flowing methane and hydrogen. This produced 70-80% SWNTs after the metal and

supports were dissolved with HCl. Kathyayini et al. [143] studied various combinations

of support materials and metal catalysts and found a wide range of yields between 2

wt% for iron nanoparticles on calcium oxide to 229 wt% with an iron/cobalt alloy on

magnesium oxide. These experiments were carried out with acetylene and ethylene at

700 °C and HCL was used to dissolve the supports after the material was removed from

the furnace. There are also many other variations on this process [144-146].

An extension of the above method is a process developed at the University of

Oklahoma, referred to as the CoMoCAT process. Like the name suggest cobalt and

molybdenum are used as the catalyst. This method was first published by Kitiyanan et

al. [147]. Incipient wetness impregnation was used to form cobalt and molybdenum

catalysts on silicon dioxide. It was found that all compositional ratios of Co and Mo

worked equally well to produce carbon nanotubes. The catalyst was calcined and then

placed in a horizontal tube furnace where CO was used as a carbon source. This

produced high yields of carbon nanotubes but these tubes were more defective than

comparable arc discharge and laser ablation nanotubes. Later this process was modified

in Resasco et al. [148] to show a scalable method of CNT production. In this case a

fluidized bed reactor was used where the powder was loaded into a vertical tube

furnace. Carbon monoxide was flowed from the bottom at a high enough rate to make

the catalyst float and bubble in a way that resemble a boiling liquid. The process

produced an 80% selectivity towards SWNTs and the tubes formed into very small

bundles which simplified dispersion. It was determined that the presence of both Mo

and Co were necessary to achieve activity and selectivity. Others have done work in this

area [149-151].

An interesting method that utilized a fixed catalyst support to grow nanotubes is an

approach that forms CNT arrays that resemble a forest or carpet. This process starts

with the deposition of a metal catalyst onto a fixed surface in a manner that produces

isolated metal particles when calcined. These particles can grow vertically oriented

arrays that resemble a forests of nanotubes. Figure 2.19a shows the production scheme

where a catalyst containing film is deposited onto an inert surface (e.g. Al_2O_3 on SiO_2

coated Si wafer). Nanotubes grown in a similar process are shown in Figure 2.19b. This

process was first described by Li et al [152] where a 50 μm tall array of carbon

nanotubes was formed by flowing acetylene and hydrogen at 700 °C over iron particles

in mesoporous silica that was formed from sol gel. It was also found that similar arrays

could be formed by using other substrate materials [153, 154]. The alignment of this

process can also be improved by adding plasma to form plasma enhanced chemical

vapor deposition (PECVD) [155] where perpendicular growth can even be achieved on
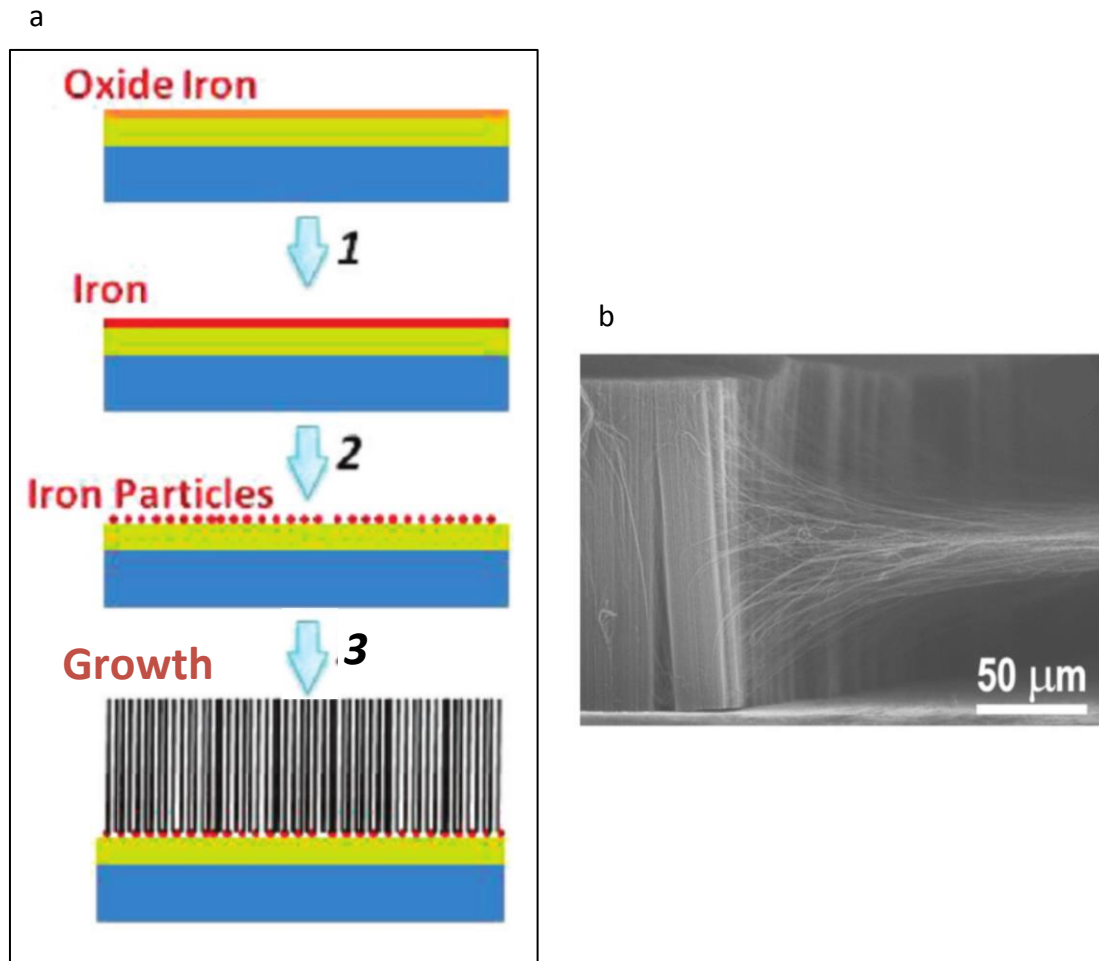
Figure 2.19: Forest growth. a) Process schematic for CNT forest growth. Adapted from [154]. b) CNT forest with nanotubes being pulled to the right. Adapted from [156].

curved substrates [157]. It was found that the vertical alignment in the PECVD process was dependent on the electric field generated by the plasma. Growth prior to igniting the plasma had poor alignment which later improved with the plasma [157].

The final method that will be discussed in this section is the horizontal growth of ultra-long carbon nanotubes formed in a floating catalyst kite mechanism. In this approach, which was demonstrated by Huang et al. [158], a small amount of catalyst particles are placed directly on the surface of a silicon wafer with a thin SiO_2 layer. With rapid heating, by quickly inserting the substrate into a heated tube furnace, the catalyst lifts off the substrate and then floats over the silicon surface moving along with the gas flow. The researchers grew an isolated nanotube 2 mm long in 10 minutes. The following year a 4 cm nanotube was reported [159], followed by 18.5cm [160], then 20cm [161] and recently a half meter [162]. If the wafer was rotated to change the gas flow direction the tube would turn and follow the new flow direction [163]. This approach certainly produces the best alignment and length of all the CNT growth methods but obviously growing individual tubes is a very low yield process and is not scalable.

2.2.2.2 UNSUPPORTED CATALYST

There are many methods of unsupported carbon nanotube growth that utilized various carbon feedstocks, a catalyst and a heat source to continuously produce carbon

nanotubes. These approaches are ideal because the feedstock can be introduced into

the furnace continuously. Some of the methods included below do not collect the CNTs

continuously but they are still discussed because this step could easily be added. The

formation of catalyst particles in a vapor is what makes these processes similar. The

distinction is that the catalyst enters the furnace as a vapor that then forms carbon

nanotubes. The methods that will be discussed are the HiPCO process, the Aerosol

methods, sublimation methods, and finally the liquid injection of carbon and metal

feedstock solutions. The purpose of this is to demonstrate the progression of growth

techniques that have led to the approach employed by Nanocomp Technologies Inc.

    The first method that will be discussed is the process trademarked as HiPco by the

researchers at Rice University. This method utilizes the high pressure

disproportionation of carbon monoxide over catalyst particles that form as a result of

the thermal decomposition of iron pentacarbonyl ($Fe(CO)_5$). This process was first

demonstrated by Nikolaev et al. [164] and further parameterized in [165]. The CO was

bubbled through the $Fe(CO)_5$ catalyst, which has a partial pressure of 7 Torr, and further

diluted with CO before introducing the gas into the hot zone of the growth furnace. This

produced a broader diameter distribution than laser ablation but the average diameter

was smaller. They also found that by increasing gas pressure the nucleation during

growth was faster and smaller diameter nanotubes could be formed. The tubes were 1

μm long based on observations with microscopy. Also, they found that rapid heating

rates were very important for this growth process. One of the challenges with this

process is the relatively high iron content (26 wt%) which could only be lowered to 9

wt% after washing with HCl [166]. The other inherent difficulty with this process is the

nanotubes form into a random powder which may be okay for forming CNT dispersions

but for aligned macro-structures of carbon nanotubes it makes processing a challenge.

Another difficulty is the risks of working with large volumes of CO.

The next method that will be discussed is hot filament CVD [167]. In this process a

heated iron wire is used to generate an iron vapor that agglomerates into catalyst

particles for subsequent CNT growth. Carbon monoxide is used as the carbon source

but the iron wire is kept in an inert atmosphere. The wire is heated restively to 400 °C,

such that the iron evaporates and nanoparticles are formed in the gas phase. These

particles are then carried into the co-flowing CO gas which disproportions on the iron

nano particles to form SWNT that are 0.6 – 2 nm in diameter on the 1 – 3 nm catalyst

particles. The nanotubes were 30 – 70 nm long. Large multiwall nanotubes are also

formed in this hot filament process with diameters up to 200 nm. Because the

nanotubes are short and they are grown from a vapor the resulting material is a loose

and randomly arranged powder.

The next approach for growing nanotubes utilized the sublimation of ferrocene as a

source of iron catalyst particles. This process was describe in several places [168-170].

The setup includes a tube furnace with at least two heating zones the first zone is held

49

at a relatively low temperature where solid ferrocene is placed and heating to 90 – 120

°C sublimes the iron metalorganic. It is then decomposed into iron nanoparticles when

transferred, by a carbon containing gas flow, to the high temperature zone. Unlike the

HiPco process, [169] showed that reducing the pressure reduced the carbon nanotube

size down to 1 – 2 nm. Fan et al. [170] showed that the addition of sulphur in the form

of thiophene increased the SWNT yield to 60% and they were able to achieve 20 g/h of

production. Like the other aerosol approaches this method produced random

arrangements of carbon nanotube powders that are not conducive to incorporation into

well aligned CNT structures without post processing.

The ferrocene sublimation process was simplified by mixing the ferrocene with a

liquid carbon precursor which could be injected directly into the growth furnace along

with a carrier gas. Andrews et al. [171] injected ferrocene and xylene at atmospheric

pressure into a quartz tube furnace. The catalyst solution was carried by argon with

10% hydrogen to grow MWNTs at 25 µm/h perpendicular to a quartz substrates. This

reference is meaningful because it is one of the earliest applications of the CVD process

that would eventually evolve into the method used by Nanocomp Technologies Inc.

Mayne et al. [172] used solutions of ferrocene and benzene blown with a sprayer to

generate aerosols that were carried through a single stage furnace to form MWNTs 30 –

130 µm long and 10 – 200 nm in diameter. The CNTs formed into a black flaky array of

nanotubes that resembled carpet. Zhu et al. [173] produced strands of carbon

nanotubes several centimeters in length with a solution of hexane, thiophene and ferrocene carried with hydrogen at 1423 K. In a similar approach Lupo et al. [174] used ferrocene in ethanol that was introduced into the furnace with a sprayer and carried by argon to decompose at 700 – 950 °C. This formed black films on the quartz tube that could be pulled from the tube walls to form long threads (12cm) of carbon nanotubes. Li et al. [175] from the University of Cambridge made a dramatic leap in this process. They injected the ethanol, ferrocene and thiophene feedstock into a hydrogen atmosphere tube furnace with a syringe pump. The furnace was heated to 1050 – 1200 °C and the process formed long interconnecting nanotubes that formed a floating aerogel. The aerogels were collected by a spinning rod or a drum that continuously collapsed the aerogel into a fiber or film, Figure 2.20a. These tubes are widely reported as being 1mm in length citing the supplementary material from Koziol et al. [176].

The preceding growth processes lead us to the Nanocomp Technologies Inc. patent by Lashmore et al. [177, 178] where a horizontal tube furnace is employed with a similar approach to the one used by the Cambridge group, Figure 2.20b. The major difference in the two systems is Nanocomps utilization of a porous catalyst support at the injector. The carbon containing gas passes through an inert porous structure that has been previously deposited with metal catalyst particles. This grows nanotubes that are later carried down the furnace for further growth and collection. This porous medium presumably plays multiple rolls including mixing of catalyst and carbon precursor along
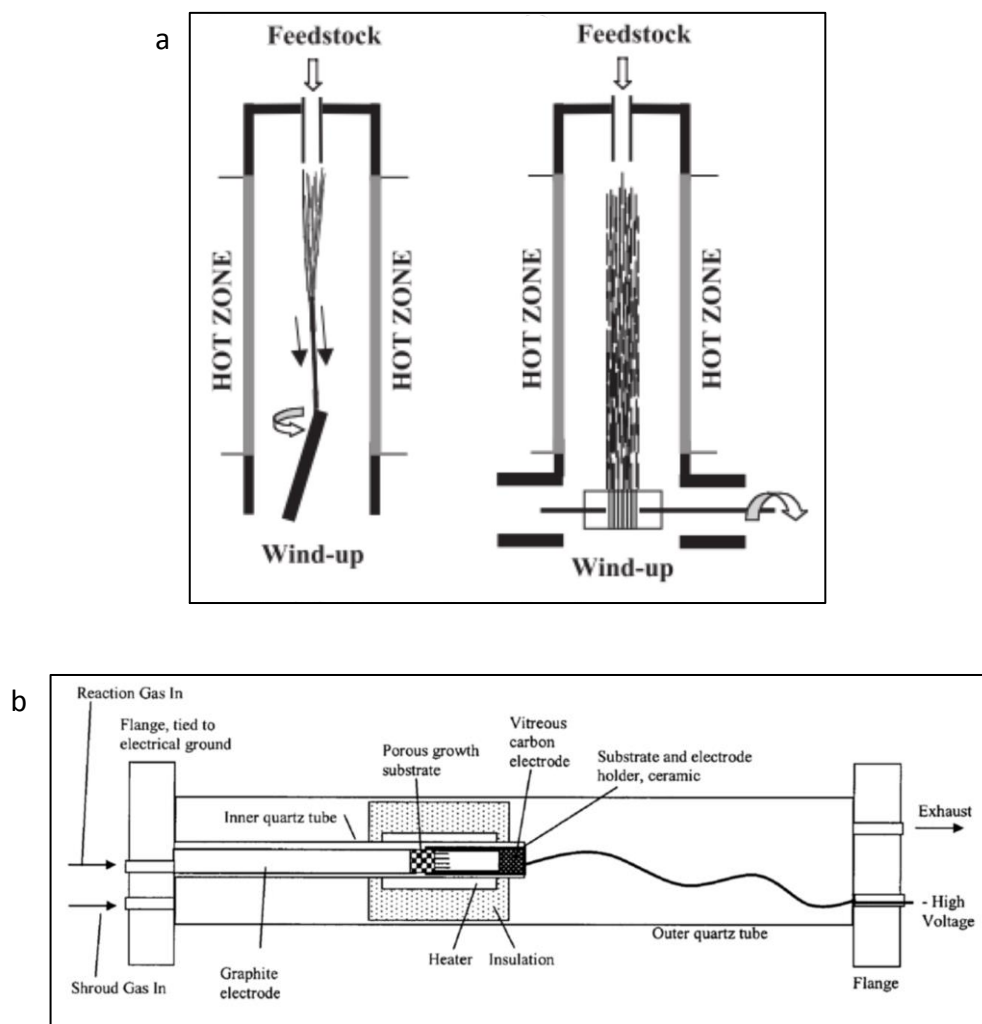
Figure 2.20: Aerogel growth. a) Schematic for continuous fiber production (left) and sheet production (right) from aerogel growth process [175] b) Schematic for Nanocomp growth furnace [177].

with rapid heating of the gas on the hot substrate. Rapid heating rates were shown to be critical for long horizontal nanotube growth [158]. The later effect was shown to be critical to the formation of carbon nanofibers by Ci et al. [179] where an evaporator was utilized at the injector before the carbon precursor and catalyst were passed into the growth furnace. The aerogel method produces random arrangements of carbon nanotubes because they are formed from a vapor. However, because the nanotubes are interconnected the network that is formed can be manipulated to achieve alignment.

2.2.2.3 OTHER METHODS

There are other unique methods for growing carbon nanotubes that are worth mentioning. These include pyrolysis, Flame synthesis, liquid hydrocarbon production and electrochemical growth. Chung et al. [180] demonstrated the pyrolysis of polypropylene into multiwall nanotubes with diameters between 4 and 16.5 nm. Solutions of polypropylene, xylene and iron nanoparticles were spin coated onto the surface of a silicon wafer to produce a film approximately 600 nm thick. A furnace was first heated to a moderate temperature to remove solvents and then heated further to the pyrolysis temperature for one hour at 6.7×10^{-5} mbar. The importance of this process is that it could be used to convert waste materials into new and useful nanostructures that can find application in electronics, composites etc. The flame synthesis method [181] impinges a flame from a hydrocarbon feedstock onto a

53

substrate that then heats a metal surface. In this case a 100 μm nickel plate is heated

on top of a ceramic disk at an adiabatic flame temperature of 1574 K. The unburned

hydrocarbons diffuse to the top surface where the heated nickel disk acts as a catalyst

to grow carbon nanotubes. This process is useful for its simplicity and its potential for

large scale production. In another unique approach carbon nanotubes can also be

created while submersed in liquid hydrocarbon. In [182] nanotubes were grown on a

silicon wafer that was cleaned with hydrofluoric acid and coated with 2 – 30nm of iron

by magnetron sputtering. The wafer was placed into methanol and ethanol baths that

were water cooled to prevent boiling. A current was passed through the wafer to

resistively heat the substrate to temperatures between 500 and 1000 °C. This grew

aligned arrays of carbon nanotubes with a prominent diameter of 20nm. Finally an

electrolytic approach can also be applied to the formation of carbon nanotubes. A

review of this technique was done by Chen and Fray [183]. The method on consists of

placing a graphite electrode into molten salt and passing a current through the salt.

Nanotubes are formed as the graphite decomposes. The nanotubes can be removed

from the salt at a later time by dissolving the salts in water. There are two mechanisms

to explain the formation of nanotubes in this growth process. The first involves the

redox of metal cations like sodium that can intercalate between the graphitic planes and

then expand when going from Na^{2+} to atomic Na. This expansion stresses the carbon

planes that then tear off and form carbon nanotubes. This mechanism is championed

by the researchers at the University of Cambridge. The other mechanism is supported

by researchers at Sussex University. In this mechanism the metal cations form carbides on the graphite surface followed by decomposition to metals and carbon nanotubes.

2.3 ASSEMBLIES OF CARBON NANOTUBES

In order to form macroscopic CNT assemblies, methods are needed to form a hierarchy that transitions from the nano dimensions of individual CNTs to macroscopic structures. To achieve this, CNTs are formed into assemblies that interconnect to form large three dimensional networks that can be used to carry loads. At the base of the hierarchy is the individual nanotube which can be single or multi walled, small diameter or large, short or long, straight or curved. The selection of the right nanotube to build the assembly can have a substantial effect on the final properties. The next level of the hierarchy is bundles of nanotubes. From these bundles of nanotubes single nanotubes and smaller bundles of nanotubes can split off and then join neighboring bundles. This creates an interconnected network of bundles that extends in all three dimensions. This is shown schematically in Figure 2.21. These networks are typically formed into sheets, yarns, fibers and foams. Here, yarns have twist added for strength as opposed to fibers which do not contain twist. These materials are broadly produced in either wet processes where structures are assembled from disperse CNT solutions or they are produced dry. In the later arrangement entanglements and van der Waals forces are relied upon to interconnect the structure.
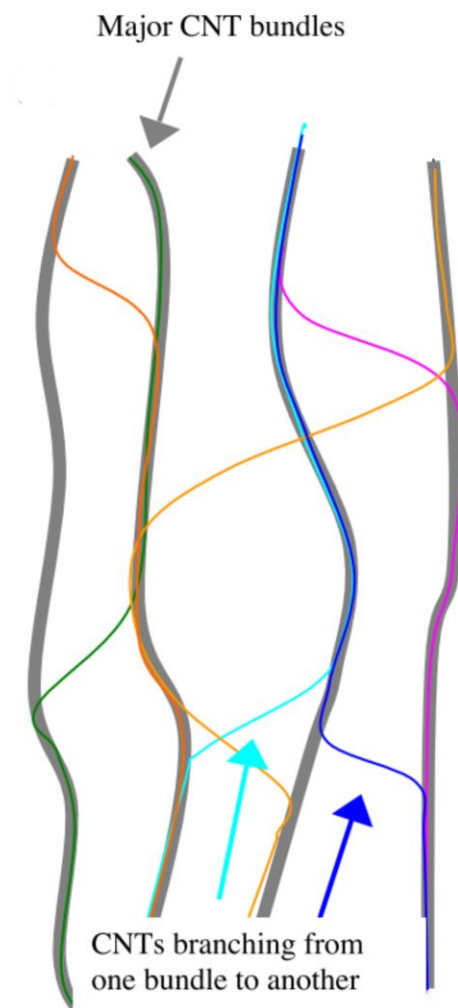
Figure 2.21: Bridging between bundles. A schematic of the bridges formed between CNT bundles. Adapted from the supplementary materials of [184].

2.4.1 WET PROCESSING

The earliest approaches to utilize carbon nanotubes in macrostructures was by the incorporation of carbon nanotubes into polymers to form particulate composites. Nanotubes have been dispersed into many polymers with many approaches ranging from sonication to melt compounding where there are significant improvements in strength, modulus and elongation to failure [185-187]. However, the concentration of nanotubes is still low and with increased additions of nanotubes, there are reductions in strength [188]. This reduction in strength was exemplified by Wong et al. [189] where composites made with polystyrene showed large agglomerations of nanotubes that acted as crack initiators, Figure 2.22. The dispersion can be improved by functionalizing the nanotubes with covalently attached side groups (e.g. hydroxides) to improve the bonding between CNT and polymer and inhibit the van der Waals agglomeration [190]. However this approach is still limited to only ~10 wt% of carbon nanotubes as a rapid rises in viscosity occurs. This was demonstrated by Shaffer et al. [191].

A simple approach to achieve high concentrations of nanotubes is to form macroscopic films of nanotubes in a process that resemble paper making. In [192] Wang et al. dispersed carbon nanotubes with sonication in surfactants and water until an ink like suspension was achieved. Filtration, aided with a vacuum, caused the nanotube to come out of suspension and form a film that was further washed to remove residual surfactant. The films could be peeled off the filter paper backing to
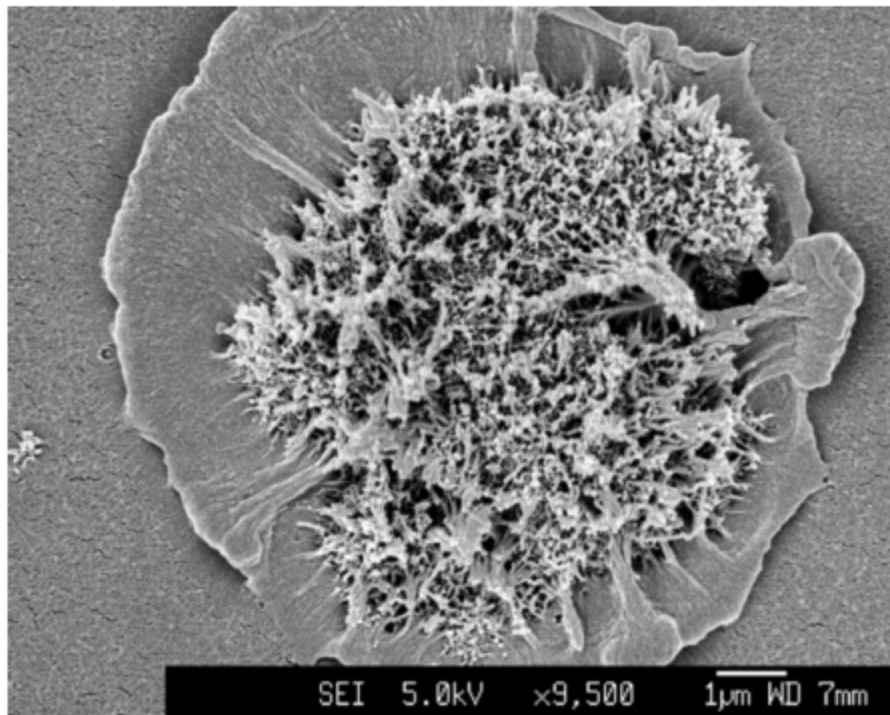
Figure 2.22: CNT agglomeration. An agglomeration is shown on the fracture surface of a CNT an polystyrene composite [189].

form a free standing CNT sheet. The sheets were then infiltrated with epoxy resin and cured in a hot press to form a composite. This approach resulted in high concentrations of nanotubes but the mechanical properties were low. The storage modulus was determined by dynamic mechanical analysis to be only 15 GPa at room temperature with 31.3 wt% nanotubes.

In another method that uses dispersed carbon nanotubes Vigolo et al. [193] developed the first method to produce CNT fibers by extruding a dispersed CNT solution into a moving coagulation bath. This method produced fibers with ultimate tensile strength and modulus up to ~150 MPa and 15GPa respectively. The coagulation bath contained polyvinyl alcohol (PVA) which remained in the fiber to form a composite. Post processing by stretching can be employed to further improve mechanical properties as was shown in [194] were strength and modulus was 230MPa and 40 GPa, respectively. Munoz et al. [29] showed that these fibers do not exhibit necking when strained therefore it was possible to impart high drawing ratios. These researchers produced fibers with 600 J/g of breaking energy as compared to Kevlar and Spectra at 33 and 50 J/g, respectively. As an extension of the previous coagulation process the CNT fibers were heated to 180°C and dried while drawing up to 850%. This generated crystallization in the PVA polymer and increased the fiber strength and modulus. These fibers had strengths of 1.8 GPa and modulus of 80 GPa. Also, reducing the diameter of the extrusion orifice can be used to increase strength and modulus to 2.9 GPa and 250

GPa, respectively [195]. It is also possible to form coagulation fibers with

ethanol/glycerol or ethanol/glycol instead of PVA [196]. This removed contaminants

that could interfere with conductivity and produced fibers with 52% less resistance (1.5

x 10^{-3} Ωm). Additionally fibers produced with PVA can be annealed following

coagulation and drawing to improve conductivity [197].

Direct dissolution of carbon nanotubes can also be achieved by the elimination of

VDW forces through surface protonation induced by super acids [198]. A high

concentration solutions of nanotubes with 102% sulfuric acid, chlorosulfonic acid, SO_3

and triflic acid, produced aligned domains like a liquid crystal that could be extruded to

form highly aligned CNT fibers [199]. This process is advantageous because higher CNT

concentrations (10 wt%) can be achieved when compared to surfactant based methods.

Behabtu et al. [200] employed this system by utilizing chlorosulphonic acid as a

dispersant. They produced highly aligned fibers by extrusion from a spinneret into a

coagulation bath. The average tensile strength and modulus were 1.0 and 120 GPa

respectively with an average elongation to failure of 1.4%. Furthermore, the

conductivity of these fibers was 2.9 x 10^6 S/m.

2.4.2 DRY PROCESSING

Dry processing means that the nanotube assemblies are formed directly from the

grown or growing nanotubes. There are some modifications for the formation

processes where solvents or other wet systems are utilized but these are not central to

the production of the carbon nanotube assemblies. There are two primary methods of

dry processing. The first is referred to as the CNT array process where specially grown

nanotube forests can be directly pulled to form and interconnected network of

nanotubes. The second is an aerogel process that grows nanotubes from a vapor to

form an interconnected network of nanotubes that floats from the growth furnace to a

collection system.

2.3.2.1 CNT FORESTS

In a process similar to that used to form silk thread the dry production of CNT yarns

was started in 2002 when researchers from Tsinghua University attempted to remove a

bundle of CNT's from a nanotube array [201]. Rather than removing a bundle of

nanotubes from the 100 μm tall array, the researchers were surprised to find a strip of

self-supporting nanotube fiber 30 cm long and 200 μm wide. In one application the

researchers used the yarns as a light emitting filament which was energized for 3 hours.

The yarn strength increased over 500% following the 3 hour thermal cycle which

suggested the possibility of welding between tubes.   By adjusting growth parameters,

the arrays can be grown strait or wavy [154]. With the proper amount of waviness the

edge of an array can be pulled to form an interconnected CNT assembly. This results

from the tubes entangling with their neighbors at the bottom and top of the array [202,

203] as shown in Figure 2.23a and b. Zhang et al. [204] incorporated a twist to the

filament as the CNTs were pulled from the array to form a yarn, Figure 2.23c. The twist
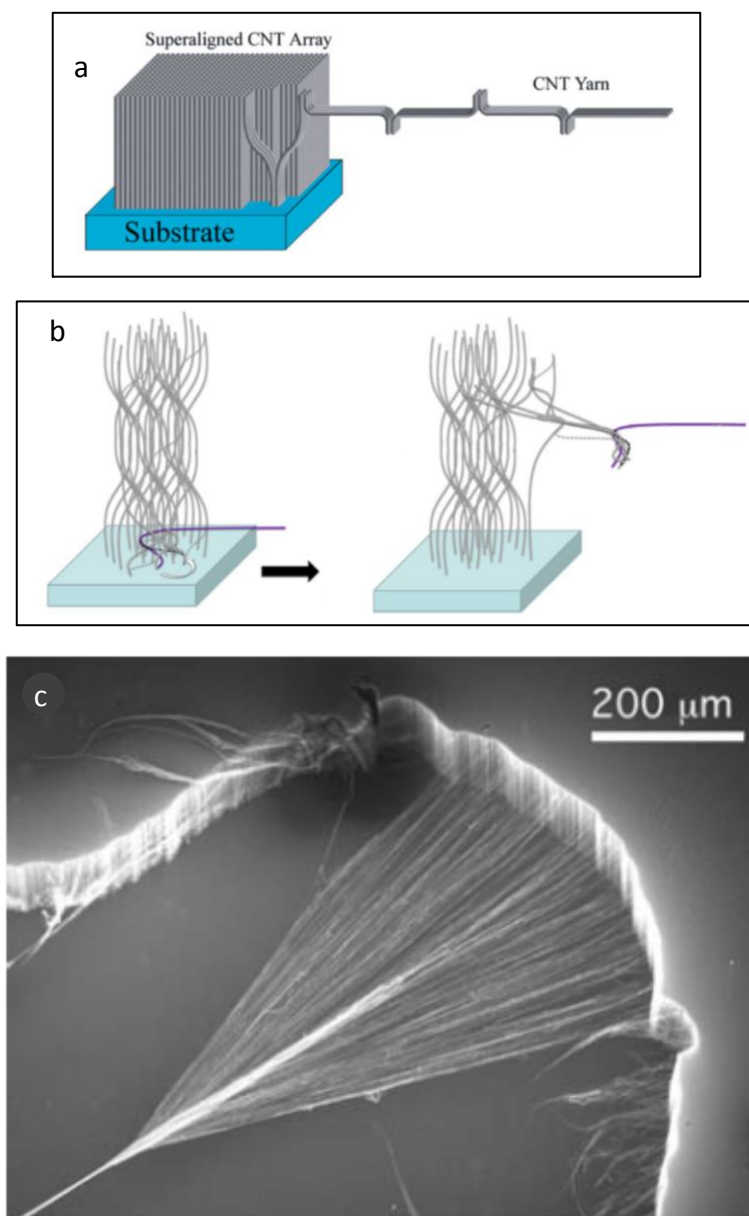
Figure 2.23: Fiber and sheet formation for CNT forest. a) Model for forest pulling based on van der Waals attraction [203] b) CNT entanglement driven pulling of CNT forest [202] c) Image of CNT fiber being pulled from a forest [204].

caused the nanotubes in the outer region of the yarn to be helically arranged. When the

fiber is placed in tension these outer nanotubes try to straighten and consequently a

radial force is generated that compresses the core of the CNT yarn and improves load

transfer.   This provided over 70% increase in strength in this report. Manipulation of

forest height and width was used to could control the yarn diameter between 1 and 10

μm and it was found that a 1 cm^2 forest could produce approximately 50 m of

continuous yarn. In [184] a detailed analysis of the twisting effects on the yarn structure

was performed. Fibers were formed from arrays by twisting between 5 and 25 turns per

mm. FIB cross-sections were made that clearly showed the formation of a densely

packed core of nanotubes corresponding the level of twist. Figure 2.24 is taken from

the report and shows a steady increase in nanotube density but at 20mm^{-1} a core

structure begins to form and at 25mm^{-1} a central core is clearly present with a diameter

approximately half that of the yarn. The maximum strength reached was 580 MPa with

a twist density of 15mm^{-1}. The addition of acetone promoted surface tension driven

consolidation which also improved mechanical properties.

In [203] the researchers introduced ethanol to the fan of nanotubes as they were

pulled directly from a 4 inch wafer. The surface tension caused the fan to shrink

together into a fiber as the ethanol evaporated. This condensing process is the same

mechanism that causes fabric to shrink in a clothes driers. It increased the packing

density of nanotubes significantly and reduced the yarns to diameters between 20 and
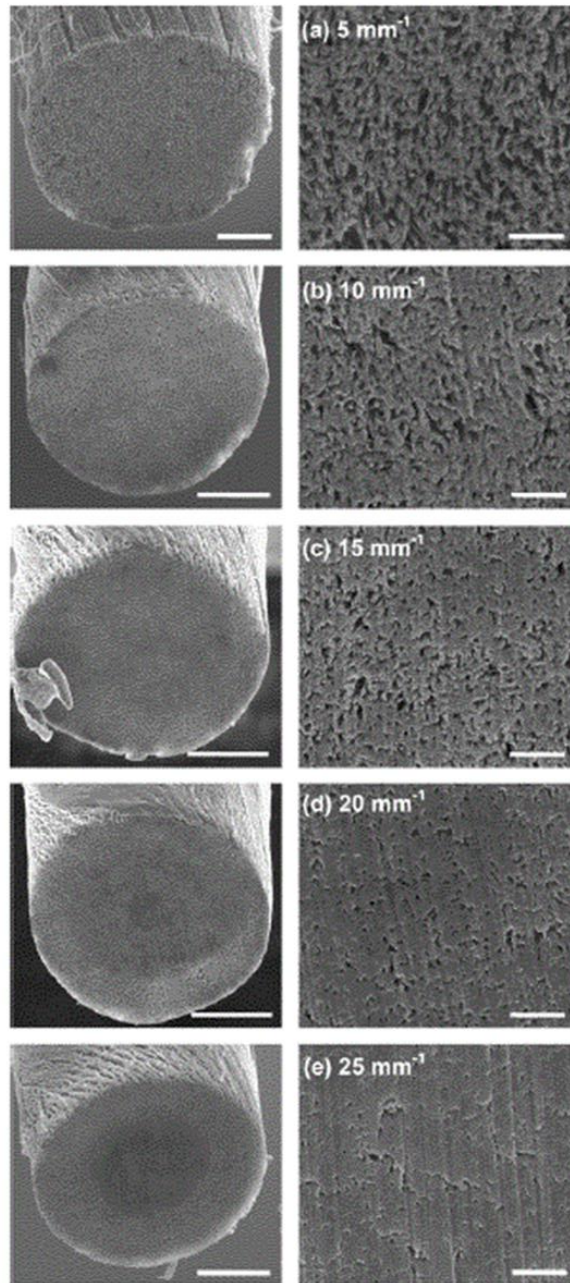
Figure 2.24: Yarn consolidation by twisting. The left column show shows the cross section of CNT yarns consolidated by twisting and the right column shows corresponding high magnification images of the cross-sections on in the right column. Left scale bars are 5μm and right scale bars are 0.5μm a) 5mm^{-1} b) 10mm^{-1} c) 15mm^{-1} d) 20mm^{-1} e) 25mm^{-1}. Adapted from [184].

30 µm to achieve strengths up to 600 MPa. Wrapping a yarn around a ceramic tube and

passing a current caused the yarns to glow in open air without failure. Following this

heating the yarn maintained its helical coil and the modulus doubled to 74 MPa

affirming the welding effect seen in [201].

It is also possible to form these CNT arrays into self-supporting sheets of low density.

A frequently observed method for nanotube sheet formation is an adaptation of the

process used to form yarns from CNT arrays. In [205] Zhang et al. demonstrated a

method to carefully pull a sheet of nanotubes from a CNT array. Grabbing the full width

of an array and neglecting twist or densifying processes made it possible for researchers

to form a meter long by 5 centimeter wide sheet. The sheets were strong webs they

referred to as an aerogel, capable of supporting water droplets despite being less than

20 µm thick and 1.5 mg/cm^3. Baughman's group reported in [206] the thermal and

electrical properties of MWNT sheets. Carefully coating the CNT sheet with ethanol and

controlling the evaporative densification produced sheets with thickness down to

100nm. These densified sheets showed superior electrical resistivity and less anisotropy

which was likely due to greater tube contact.   Densification in [207] help the

researchers reach 50nm but some variation in thickness is expected to originate from

the height of CNT array. As the starting array gets taller the areal density increases and

this will be reflected in the final sheet thickness. The reported specific strengths for the

sheets were approximately 465 MPa/(g/cm^3) for aligned and densified samples and 120 – 140 MPa/(g/cm^3) for as drawn sheets.

Another interesting aspect of these materials is its rate dependence. Zhang et al. [208] demonstrated that the failure strength of the CNT fibers was highly rate dependent such that tensile testing at a strain rate of 2 x 10^{-5} s^{-1} produced a tensile strength of 500 MPa while testing at a rate of 2 x 10^{-1} s^{-1} increased the tensile strength 140% to 1.2 GPa. This was achieved with a corresponding reduction in the elongation to failure. They also found no variation in the strength depending on the gauge length even when testing down to 1mm. This indicated the tubes could not span the gauge and improve mechanical properties. Furthermore, they observed permanent deformation with cyclic loading where each cycle had 100 MPa higher stress. All the cycles showed hysteretic loss. In the first few low stress cycles, the material returned to its original elongation however at 300 MPa the strain became permanent and the hysteresis loops grew larger with each cycle. This was in contrast to Naraghi et al. [209] that observed an immediate plastic deformation with cyclic loading.

Zheng et al. [210] investigated the effect that array morphologies had on the mechanical properties of CNT fibers. They found that fibers produced from wavy arrays had lower strength and modulus than those produced with straighter nanotubes. For all the samples there was a positive correlation between strength and modulus. Zhang et al. [211] showed that the length of carbon nanotubes has a significant effect on the

mechanical properties of carbon nanotube fibers. By testing arrays from 300 μm in length to 650 μm in length it was shown that the strength of the fibers increased from 300 MPa to 900 MPa. They also showed clearly that twisting improved not only the mechanical properties of the fibers but also reduced the resistivity.

Wang et al. [212] made composite CNT assemblies from an array and as the nanotubes were pulled from the array where it dragged over rods to improve alignment. The material was then collected on a rotating drum to form a multi-layer sheet while being sprayed with bismaleimide resin. After curing the sheet showed up to 41 W/m/K thermal conductivity and 570 S/cm of electrical conductivity. The mechanical properties of the material were exceptional at 3.5GPa strength and 266 GPa modulus without the need for functionalization to improve the load sharing between the CNTs and the resin.

A challenge with this material is that the process of growing nanotubes on a wafer and drawing fibers or sheets is inherently a batch process. This makes it difficult to scale into a production environment. To overcome this challenge Lepro et al. [156] demonstrated the ability to grow carbon nanotube forests on the surface of flexible stainless steel substrates. Fibers could be spun from the carbon nanotube array and then the substrate could be reinserted into the growth furnace to form additional CNT arrays as the catalyst remained active. This led to patents for a growth furnace incorporating a belt that could be used to produce carbon nanotube assemblies continuously [213, 214].

2.4.2.2 CVD AEROGEL

The aerogel method utilizes the aerogel growth CVD process developed by Windle's group at the University of Cambridge. As was described earlier, the carbon, metal, and promotor feedstocks are injected into the rear of a CVD tube furnace where an interconnected aerogel of carbon nanotubes is formed. This aerogel can be collected by spinning to form a yarn or collected onto a drum, layer by layer, to form a sheet [175]. The fibers spun in this report ranged in strength from 0.1 to 1.0 GPa with strains to failure that could exceed 100%. With a similar methodology Zhong et al. [42] showed that by growing the aerogel with a mixture of ethanol and acetone and pulling the resultant through a water bath followed by an acetone bath produced consolidated fibers with a layered structure. These fibers were between 0.4 and 1.25 GPa. This was in comparison to an earlier report by Koziol et al. [176] where fibers were pulled directly from the aerogel grown with ethanol and consolidated in line with a spray of. These fibers did not demonstrate the same layered structure as mentioned previously. These densified fibers showed dramatically higher strengths and with a 1 mm gauge length it was observed that the failure strength became bimodal with a high specific strength peak at 6.5 GPa/SG. The highest strength fiber tested had a strength of 8.8 GPa, a stiffness of 357 GPa and a toughness of 121 J/g. Additionally the fibers produced by this group were compared to other high strength fibers for knot strength in Vilatela et al. [215]. In this test a single over-hand knot is tied in the fiber and the strength is determined. The CNT yarns retained 100% of its strength with the knot as compared to

Kevlar, and Dyneema fibers which had only 20% and 50%, respectively. The reduced

strength was a result of compressive buckling in the fibers that weakened the structure.

This demonstrated the high toughness and true yarn like character of the CNT fibers.

Aerogel carbon nanotubes have also been transformed into composites. Cheng et al.

[216] produced carbon nanotube and bismaleimide (BMI) composites. They stretched

CNT sheets, produced by Nanocomp Technologies Inc, up to 40% elongation, and

infusing these stretched sheets with a solution of BMI and acetone. This was followed

with curing in a hot press after removing excess solvent in a heated vacuum oven.

These researchers achieved a strength of 2.1 GPa for their composite and up to 600

S/cm of electrical conductivity. This was compared to 500 MPa strength and 420 S/cm

in the unstretched material. The elongation at failure of the composite materials was

between 1.8 and 2.5%. This group also made composite sheets utilizing surface

functionalization with epoxide groups to improve the load sharing between the CNT

surface and polymer [217]. These composite sheets reached a tensile strength and

modulus of 3.1 GPa and 350 GPa, Respectively. This elongation to failure was 0.8%.

2.4.3 OTHER METHODS

Lupo et al. [174] demonstrated that long strands of carbon nanotubes could be

formed on the walls of a growth furnace. This process is similar to that used at the

University of Cambridge, but the tube extends well past the furnace allowing the

nanotubes to condense on the quartz walls. This produced a film of carbon nanotubes

that can be grabbed with a metal probe and removed from the tube wall as an interconnected film. The length of this film was only 12 cm but it could be twisted into a fiber. The film structure was only found on the cool region of the exposed quartz tube. The nanotubes retrieved from the hot zone were filled with large particles of carbon and iron. This process was used by Ma et al. [117] to produce CNT yarns and composite fibers filled with epoxy and PVA. The epoxy filed fibers had strengths ranging from 0.9 to 1.6 GPa and the PVA fibers ranged from 0.7 to 1.3 GPa. The modulus of the epoxy and PVA fibers were 30 – 50 GPa and 20 – 35 GPa, respectively. These researchers also performed in situ Raman measurements to determine the strain applied to the nanotubes. They determined that the cross-linking in the epoxy polymer allowed more load to be transferred to the nanotubes as compared to the linear chains in the PVA.

Gommans et al. [218] produced CNT fibers from a disperse solution of carbon nanotubes in dimethylformamide. A platinum electrode was placed into the solution in addition to a carbon fiber electrode that was attached to a retractable linear motor. A 1 – 2 V potential was placed across the electrodes with the carbon fiber attached to the positive potential. This caused the nanotubes to pick up negative charge from the surrounding bath and migrate to the carbon electrode. The electrode was slowly removed from the bath to form a fiber that is consolidated by surface tension. The physical properties were not determined but polarized Raman spectroscopy was used to demonstrate the structure was aligned.

Other approaches are used to create three dimensional foams. These materials can also be described as CNT aerogels in a similar fashion to silica aerogels from sol gel processing. Worsley et al. [219] formed foams by dispersing nanotubes into solution and adding sol-gel to bind the network together. Following super-critical CO_2 drying, the foam was pyrolized to form a conductive network. These foams were stiffer than alumina nanofoams and they showed high elasticity up to 76% compression. Bryning et al. [220] used a similar procedure to produce CNT foams but instead of using sol gel as a binder they used PVA. These reinforced aerogels had pore sizes in the range of tens of nanometers and they could support 8000 times their own weight. The foams were envisioned as chemical sensors, reaction catalyst and porous electrodes. The densities ranged from 10 – 30 mg/mL without PVA and 40 – 60 mg/mL with PVA. The conductivity of the sample without PVA was nearly 1 S/cm however reinforcement of the foam with PVA reduced the conductivity.

2.4 POST-PROCESSING FOR ALIGNMENT

There are many advantages to achieving alignment in carbon nanotubes as a result of their anisotropic mechanical, electrical and thermal properties. There are several ways to characterize the alignment of carbon nanotubes within composites and in CNT assemblies. The most basic is to measure the bulk properties along, and transverse to, the preferred direction of alignment. There are also methods using anisotropy in light absorption and Raman signal. Furthermore there are direct structural characterization

methods utilizing X-ray diffraction. These methods will be discussed in the following

sections along with some of the different methods used to impart alignment to carbon

nanotubes.

2.4.1 CHARACTERIZATION METHODS

A common approach to characterizing the alignment of carbon nanotubes is to

measure the intensity of the G band in polarized Raman spectroscopy parallel and

transverse to the direction of interest. In this case the Raman peaks are a result of

resonant enhancement which varies based on the angle between the electric vector and

the CNT longitudinal axis. This in turn varies the absorption by the nanotube, and as a

result, the intensity of Raman peaks. The maximum response occurs when the

nanotubes are aligned with the light polarization and minimum when they are oriented

perpendicular. Gommans et al. [218] developed a model to compare the intensity of

the Raman peaks when CNTs are aligned and unaligned with polarization. This gave a

percentage of nanotubes oriented within a given angle of the orientation axis. In

practice a simple ratio between the G peak intensity parallel and perpendicular to the

sample orientation often suffices [205, 221, 222]. This process is ideal because it is

quick, it can work on almost any CNT containing material and the calculations are easily

performed. However, the method is surface sensitive so the results are not necessarily

representative of bulk alignment. Furthermore, because the absorption changes

parallel and perpendicular to the polarization, so the sampling volume is different for the different orientations.

Another technique used for determining the alignment of carbon nanotubes in a CNT assembly or composite is X-ray diffraction. This application of this technique to CNT assemblies is barrowed from the analysis of polymer fibers and films where transmitted X-ray diffraction is regularly used to characterize the arrangement of polymer chains [223]. For an introduction to X-ray techniques and reciprocal space the reader is referred to [224]. The two techniques of concern to the characterization of carbon nanotube assemblies are wide angle X-ray scattering (WAXS) and small angle X-ray scattering. Because the spectrum produced by these X-ray techniques are in reciprocal space the structures being analyzed by WAXS are on the order of angstroms and nanometers while for SAXS the structures investigated are on the order to $1 - 10$ nm. As a result, the space between side walls of carbon nanotubes is readily characterized with WAXS because of its ~3.4Å value [67]. On the other hand, hexagonal bundles of individual nanotubes form a structure with characteristic feature sizes above 1 nm so these features lend themselves to characterization by SAXS. A schematic arrangement of the X-ray characterization is given in Figure 2.25. Firstly, the diffraction intensity is perpendicular to the structures inside the sample and these structures produce an intensity distribution around the angle χ. These are referred to as the azimuthal intensity profiles. Both WAXS and SAXS utilize area detectors that measure the

73
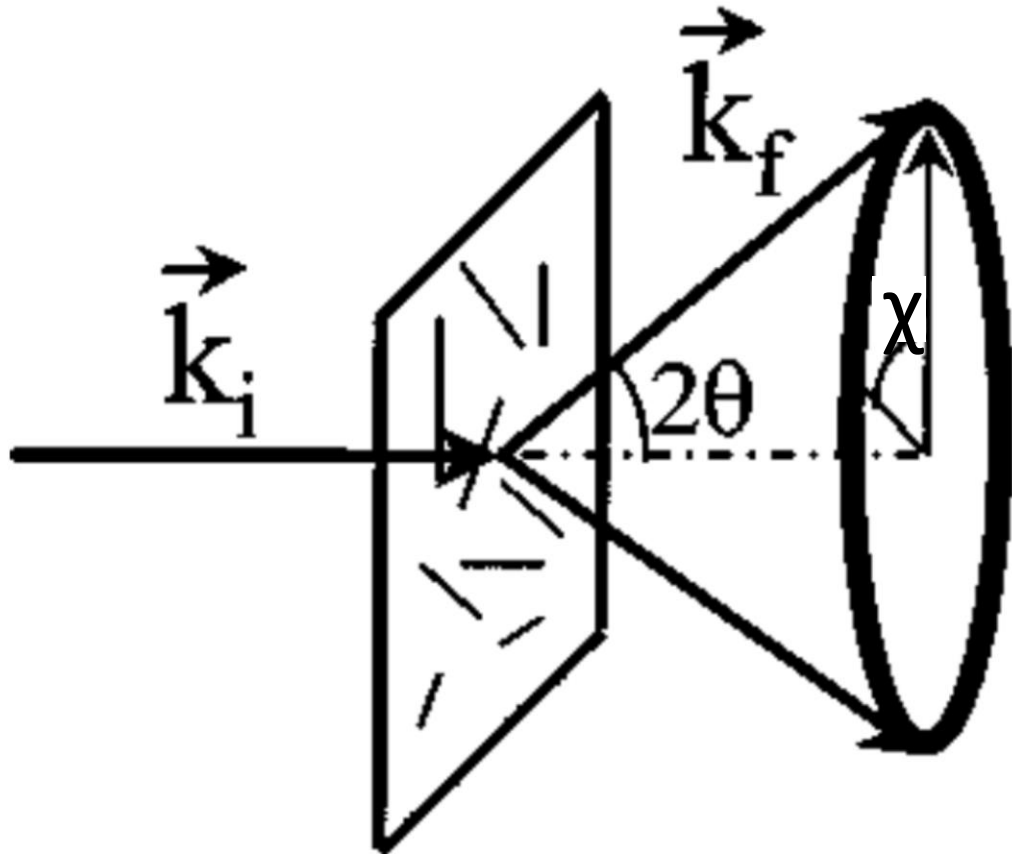
Figure 2.25: Arrangement for X-ray scattering. a) X-rays pass through CNT material and scatter by 2θ and the distribution is given by χ. Adapted from [225].

diffracted intensity from the carbon nanotubes in two dimensions. This makes it simple

to obtain the distribution of nanotubes around the incident X-ray beam by integrating

around χ with respect to the sample axis. The profiles are often integrated,

circumferentially, around 180° or 360° of the azimuthal diffraction rings to show either

one peak or two peaks, respectively [221]. The distribution is often quantified with

either a measure of the full width at half maximum (FWHM) or by the half width at half

maximum (HWHM). The HWHM is sometimes referred to as the mosaic angle. Another

commonly applied approach is the Hermans orientation factor (HOF) [226]. The HOF is

an average of the cosine squared distribution of crystals in the sample. The equation

has the form below;

$$HOF = \frac{3\langle\cos^2\psi\rangle - 1}{2}$$

(2.2)

Where,

$$\langle\cos^2\psi\rangle = \frac{\int I(\psi)\cos^2\psi\sin\psi\,d\psi}{\int I(\psi)\sin\psi\,d\psi}$$

(2.3)

For a structure perfectly aligned with the direction of interest the function returns a

value of 1, if the sample is randomly oriented the function returns 0 and if the

orientation is perfectly transverse to the direction of interest it returns a value of -0.5.

The difficulty with characterizing alignment of carbon nanotubes with X-ray diffraction is that samples that are dispersed such that the nanotubes are not in direct contact loose the reflections associated with 002 graphitic wall spacing. This leaves only the small angle scattering. However the nanotubes used in structural applications are rarely of a single diameter so the small angle scattering broadens and makes characterization more challenging. Furthermore, the small diameter single wall nanotubes that are the most desirable for their physical properties also have less wall flattening which reduces signal from 002 reflections. Fortunately, the material used for the present work is made up of nanotubes with substantial bundling and wall flattening. This simplifies the alignment characterization. A further advantage of X-ray diffraction is that the sample volume is large, providing good averaging. The X-ray spot size can be on the order of hundreds of microns and the sample thickness is ideally 0.5 to 1 mm. Also, because the beam passes through the sample it measures the entire volume and is not biased by surface effects. The downside of the approach is that in the laboratory setting it can take $10 - 20$ minutes to analyze a single sample. With longer sampling time, there is also scattering from air that produces background noise.

   The other methods for characterizing alignment are simple approaches of direct observation with microscopy and the measurement of anisotropic bulk properties.   It is not necessary to go into detail about how these characterizations are performed so

76

instead the techniques used to achieve alignment in carbon nanotube composites and assemblies will be discussed.

2.4.2 ALIGNMENT METHODS

2.4.2.1 Rubbing

Possibly the simplest method to obtaining alignment in carbon nanotubes was demonstrated by deHeer et al. [227]. In this report the authors dispersed CNTs into ethanol and then filtered the suspension to form a film. The film was then transferred to a plastic surface and aligned by lightly rubbing the surface with a thin Teflon sheet. These authors demonstrated anisotropic optical and electrical properties in the aligned material. This demonstrates one of the challenges in determining the alignment of a nanotube assemblies. It is easy to dramatically alter the surface alignment of nanotubes. Tran et al. [228] incorporated the rubbing process into the spinning of fibers from vertically aligned CNT arrays in a "capstan effect rod system". This method has the CNT fiber slide over the surface of several rods. This induces an increasing tension as the fiber pulls through the rod system and it induces transverse forces in the fiber to aid consolidation of the CNT network. They qualitatively demonstrated the alignment improvement by electron microscopy but they did see an increase in strength and modulus. The strength improved to 1.2 GPa from 500 MPa. The modulus was not enumerated but the increase was clearly evident in stress vs strain curves.

2.4.2.2 STRETCHING

Early on, carbon nanotubes were being dispersed into polymers to form composites. Ajayan et al. [229] found that cutting thin slices of a nanotube and epoxy composite induced alignment of both nanotubes within the polymer and nanotubes that were partially pulled out. In Jin et al. [225] the authors made composites with CNT concentrations of approximately 30 vol% with thermoplastic polyhydroxyaminoether film. These were mechanically stretched up to 500% elongation at 95 – 100 °C. They determined the alignment with WAXS and observed the distribution of the 002 reflection. They found that the FWHM reached 47°. Furthermore, they determined the percentage of aligned nanotube by integrating the total intensity under the azimuthal peaks and determined that 58% of the nanotubes were partially aligned after 330% elongation. They also showed that composites with lower concentrations of carbon nanotubes had narrower alignment distributions when stretched to equivalent levels of elongation. Du et al. [230] extruded fibers of polymethyl methacrylate with 2 wt% carbon nanotubes and applied drawing to impart alignment of the tubes. From SAXS these authors determined the FWHM of the CNT distribution and correlated this to the electrical properties of the fibers. The electrical percolation depended on concentration as expected but more interestingly the electrical conductivity was reduced as the alignment of the CNT was increased. This was a result of the percolating network being broken as the fiber aligned.

Koziol et al. [176] aligned CNT fibers by gradually increasing the rate at which CNT

aerogels were pulled from the growth furnace. As opposed to [216], they saw a uniform

relationship between the polarized Raman intensity ratio and the HOF. Both these

values increased gradually with winding rates of the CNT fibers. The Raman ratio

increased from 3 to 4 when increasing the winding rate from 5 to 20 m/min while the

HOF increased from 0.55 to 0.85. They also observed an increase in specific gravity with

winding rate as the CNTs packed closer together reaching a maximum of 0.9. In the BMI

and CNT composite sheets of Cheng et al. [216] the authors used both polarized Raman

and X-ray diffraction to quantify the alignment of stretched CNT sheets. The change in

the Ratio of G peak intensities changed abruptly above 30% stretch however the degree

of alignment from X-ray diffraction increased gradually with stretching ratio. At 20%

elongation these authors observed an HOF of 0.45 and at 40% elongation this increased

to 0.8.

This alignment with stretching was also observed by Miaudet et al. [231].   The SWNT

and MWNT composite fibers were formed with PVA by the coagulation of the

nanotubes in a manner following [193]. Miaudet et al. stretched the fibers to 850% at

180 °C. Fibers that were not hot stretched showed high toughness up to 870 J/g and

elongation to failure up to 430% but the initial mechanical properties were low. After

hot drawing the tensile strength and modulus were 1.8 GPa and 45 GPa, for SWNTs and

the strength and modulus were 1.4 GPa and 35 GPa, respectively for MWNTs. Before

hot stretching the HWHM was ±27° and after stretching the alignment of the PVA was ±4.3° and ±6.3° for the SWNT and MWNT fibers, respectively. The alignment of the nanotubes themselves was not as good at ±9° and ±11° for SWNT and MWNT, respectively. Sreekumar et al. [232] produced polyacrylonitrile (PAN) fibers with up to 10 wt% of nanotubes by wet spinning from a 500 µm spinneret. They characterized the alignment with X-ray diffraction and Raman spectroscopy and demonstrated the polarization of the material by infrared transmittance parallel and perpendicular to the fiber axis. They found that the CNTs had higher alignment than the PAN which they attributed to the higher rigidity and longer relaxation times of the nanotubes.

Zhang et al. [208] measured the mechanical properties of carbon nanotube fibers made by the forest twisting approach. The measured the alignment with the ratio of the Raman G band parallel and perpendicular to the fiber axis and observed a linear relationship between the ratio and their fiber strength. Zhang et al. [233] also used WAXD and polarized Raman to characterize the alignment of CNTs in yarns spun from forests. The Raman ratio for the spun fibers was 2.7 and the solvent densified fibers reduced to 2.2 and from WAXS the FWHM was 33° for the densified fiber.

2.4.2.3 ELECTRIC

Another avenue for achieving alignment in dispersed CNT composites is by applying an electric field. This has been achieved by placing electrodes within or at the edges of

a container of the CNT and liquid. Bubke et al. [234] observed optical polarization as a result of applying an electric field to a dispersion of carbon nanotubes in ethanol. A similar methodology was employed by Martin et al. [235] where both AC and DC electric fields were applied to dispersions of carbon nanotubes in epoxy. The AC electric fields showed better alignment of the CNTs as compared to irregular networks formed in the DC field. It was found that stronger electric fields lead to better conductivity of the samples but the cured samples were only suitable for dissipating electrostatic charge. The alignment also induced optical transparency in the composite.

2.4.2.4 MAGNETIC

Smith et al. [236] produced films of carbon nanotubes by passing a dispersion of carbon nanotube through a filter that was in a magnetic field of 25 T. They determined the alignment with WAXS and found that the thin ~1 μm films had a FWHM of 25° − 28° while thicker ~7 μm samples had a broader distribution of 35±3°. Also they found that the density of the aligned films were higher than unaligned films, presumably because of better packing of CNTs.   Fisher et al. [237] magnetically aligned carbon nanotubes in 7 T and 26 T magnetic fields. Using SAXS they determined FWHM of 33° and 34° for the 7 T and 26 T magnetic field, respectively. These corresponded to 42% and 40% of the nanotubes falling within the azimuthal peak, respectively. The ratio in the Raman G band was ~3 and ~4 for the 7 T and 26 T fields, and there was a 9x anisotropy in the resistance parallel and perpendicular to the alignment direction. This electrical

anisotropy dropped to ~6x after annealing. This work can be compared to [238] where a

24x anisotropy in electrical resistance was observed.

2.4.2.5 PUSH OVER

An interesting method used to align CNT arrays into a film was a "domino pushing"

method developed by Wang et al. [239]. In this approach a vertically aligned array of

carbon nanotubes is collapsed in one direction by a cylindrical roll. The roll is pushed

along the array to form a CNT sheet between a micropore membrane and the silicon

growth substrate. The CNTs stick to the membrane and lift off the growth substrate.

The free standing CNT film is then removed from the membrane by washing with

ethanol. These samples had a thermal conductivity of 331 W/m/K parallel to the

alignment and 72 W/m/K perpendicular. The electrical conductivity was 2.0×10^4 S/m

parallel and 1.1×10^4 S/m perpendicular. This process can be compared to one

developed by Bradford et al. [240] where a CNT array was pressed with a shearing

motion to knock over the entire array at the same time. They infused their samples with

epoxy to form a composite with 27 vol% of CNTs. These composites had a strength of

300 MPa but if a 5% stretch was performed on the samples prior to curing the strength

increased by a third to 402 MPa. Additionally, stretching increased the modulus by 50%

to 22.3 GPa. In the aligned CNT structures without resin the conductivity was 1.2×10^4

S/m parallel and 0.4×10^4 S/m perpendicular to the alignment direction.

2.5 MODELS FOR LOAD TRANSFER BETWEEN NANOTUBES

Individual carbon nanotubes have exceptionally high mechanical properties but the strength of their assemblies falls short as a result of their imperfect structures. To understand the upper bound of CNT assembly properties Cornwell et al. [51] developed a model for the mechanical properties of an ideal CNT bundle, Figure 2.26a. The model incorporated a hexagonally packed bundle of (5,5) nanotubes with individual tensile strengths of 110 GPa. The CNTs were shorter than the overall test length so a nanotube could not span the test gauge and skew results. Furthermore, the position of the tube ends were randomly positioned. Because the strength is dependent on the shear load between nanotubes, cross-links were added between nanotubes by insertion of randomly arranged carbon atoms. The concentration of these cross-links were set between 0.125% and 0.75% of the total number of atoms in the model. The stress was measured based on the cross-sectional area of the hexagonally packed bundle of nanotubes. The nanotubes had a radius 3.49 Å and the inter-tube distance was 3.33 Å as a result of the cross-links pulling the tubes together. The test with the longest tubes (800nm) and the highest cross-link concentration (0.75%) showed a tensile strength of 60 GPa, a modulus of 700 GPa, and elongation to failure of 15%. These mechanical properties are promising for the potential for carbon nanotube structure however these results are a long way from mechanical properties measured experimentally.
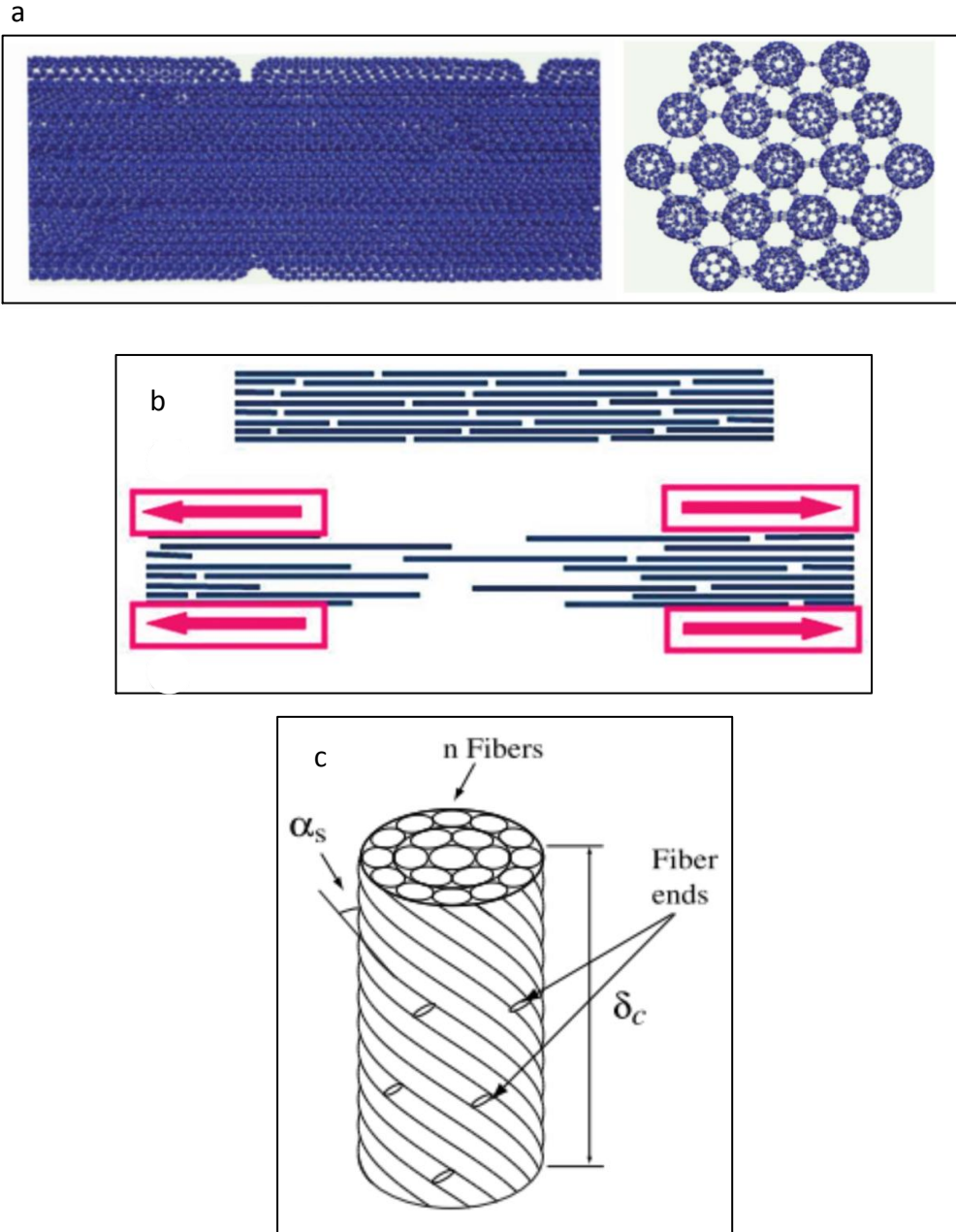
Figure 2.26: Nanotube fiber models. a) A cross-linked array of parallel and short CNTs cross-linked by carbon atoms [51] b) An assembly of parallel rigid rods that resist sliding apart by shear stress [241] c) A helical fiber that compresses the central fibers as the structure is placed in tension [242].

To better reflect the mechanical properties of fibers measured experimentally, Vilatela et al. [241] developed a model relying on the shear stress between carbon nanotubes, Figure 2.26b. They considered a system made up of parallel rods that transfer load to neighbors through shear. This shear stress was estimated from literature to be 0.05 MPa, though the data had significant spread from 0.04 to 69 MPa. The other consideration was the shear area between the rigid rods. These were given two fractional modifiers to reflect that a double wall nanotube has approximately half of its cross-sectional area available to transferring load. As a result of tube flattening, the second modifier considered the surface area of a nanotube that is in contact with neighbors. The model linearly followed results for the strength of CNT yarns with respect to nanotube length however there was no correlation with modulus. The poor agreement with modulus was attributed to comparing fibers produced by several methods. The fibers presumably had varying waviness of the nanotubes which altered modulus and not strength. They also estimated the maximum shear force that could be applied to a 1 mm long nanotube to be 21 N/m. This is less than the 42 N/m that was experimentally found necessary for nanotube breakage. This demonstrates that failure of constituent tubes is reasonably neglected in the model and the assumption that failure only occurs by sliding is sound.

Beyerlein et al. [243] built on a helical fiber model developed by Porwall et al. [242] by applying its approach to load transfer in helically arranged fibers. The authors

performed an analytical and Monte Carlo simulation of the probabilistic strength of a large twisted bundle of carbon nanotubes, Figure 2.26c. The bundle formed an ideal helical structure where the central tube was strait and each successive layer of nanotubes had increasing helicity up to the maximum helix angle of the outermost layer. The helical nature of the structure caused nanotubes at the core of the fiber to be compressed latterly. The failure strength of the fiber when disregarding friction was considered first. The individual nanotube strength was given a Weibull distribution. With a narrow dispersion in the strength, it was found that fibers had higher failure strength but also lost ductility. The failure localized, in spite of the lack of frictional load sharing. The failure of a nanotube caused stress increases in the outer neighboring tubes as a result of the higher helical angle. When considering friction, load could be transferred to neighboring nanotubes when an individual CNT would break. It also reflected the observation by Zhang et al. [211] that the fiber strength was reduced as the diameter of the helical filaments increased. Ultimately, the model predicted fiber strengths between 2 – 5 GPa.

It is also important to understand that the sliding forces between carbon nanotubes is not necessarily a constant value but can be altered by the arrangement of nanotubes. Qian et al. [151] used a molecular mechanics approach to investigate the resistance to pulling out a single carbon nanotube from a twisted hexagonal bundle, Figure 2.27a. By twisting the bundle of nanotubes the outer six tubes formed a helix. As a result of
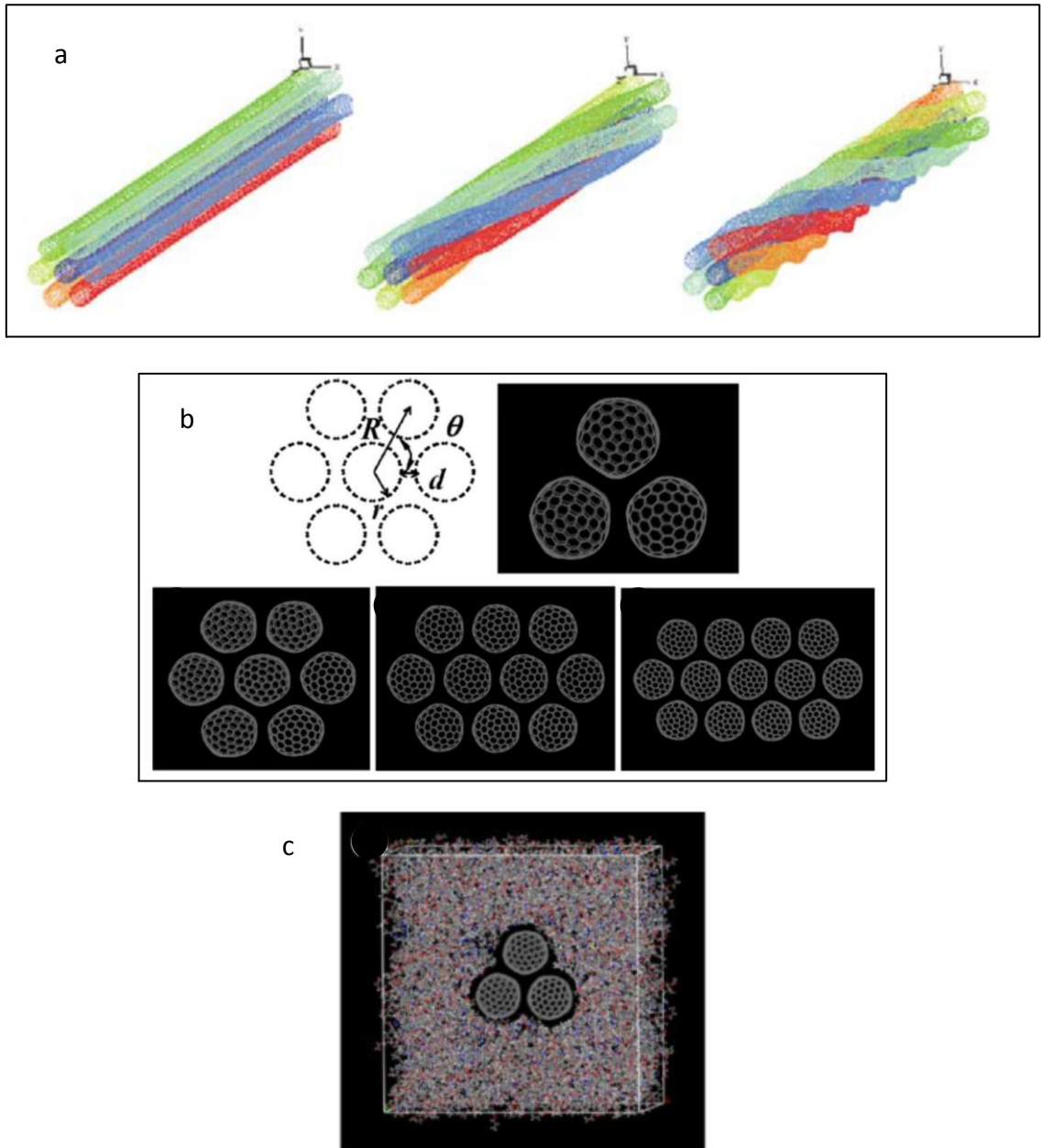
Figure 2.27: Models for CNT slip inside bundles. a) A twisted bundle of CNTs [151] b) Bundles of 3, 7, 10 and 13 nanotubes [244] c) Bundle of 3 nanotubes in epoxy polymer [244].

tensile forces on the curved members, tangential forces were generated that squeezed the central nanotube. Additionally, when the bundle is twisted, the nanotube walls deform and flatten which increased the contact area. There was almost no resistance to CNT pullout when the bundle was not twisted. However, as the bundle twists, the transferred load increases to a peak 30 times that of the untwisted structure. When the bundle is further twisted, the outer tubes actually over compress the central tube and extrude it from the core. This results in a negative value for the transferred load. The important take away from this model is that the configuration of the carbon nanotube bundle can have a dramatic effect on the load transfer between nanotubes.

Gou et al. [244] investigated the interaction between bundles of carbon nanotubes and an epoxy polymer that completely surrounded the bundles. The molecular mechanics model consisted of (10,10) carbon nanotubes arranged in triangular or hexagonal bundles of 3, 7, 10, and 13 nanotubes, Figure 2.27b. A model was also developed for a bundle of 3 nanotubes what were surrounded by epoxy polymer without covalent cross-linking, Figure 2.27c. The conclusion drawn from the bundles of 3 to 13 nanotubes without resin was that the number of nanotubes had no impact on the interfacial binding energy when pulling a single tube from the bundles. The polymer model with three tubes showed a somewhat different result. First when relaxing the model the polymer intimately wrapped around the carbon nanotubes but it was not able to penetrate to the center of the triangular bundle. This meant there were two

distinct surfaces, and correspondingly binding energies, between nanotubes and between nanotubes and the epoxy. The binding energy was investigated for when the entire bundle was pulled out from the epoxy and when a single nanotube was pulled out from the bundle breaking the bonding between the neighboring tubes and neighboring epoxy. Interestingly the binding energy associated with pulling a single tube from the structure was 40% higher than the binding energy when pulling all three nanotubes out from the polymer. This indicates that pulling a single nanotube in the bundle would result in the entire bundle being removed from the polymer.

CHAPTER 3: CHARACTERIZATION OF NANOCOMP MATERIAL

3.1 INTRODUCTION

The catalyst, nanotubes, bundles and bridges are the structures that form CNT

assemblies. The purpose of this chapter is to establish the structures within the CNT

material that will be used in the present research. A good understanding of the type of

features that can be expected within the CNT network is important because the work of

this dissertation is focused on the microstructure and mechanical properties of CNT

assemblies, CNT composites and how loads are transferred through the CNT networks.

Therefore this chapter looks at the CNT network in a hierarchical fashion starting from

the CNT catalyst and the structures they form, to the CNT networks, the linkages

between the nanotubes and how the three dimensional extended networks are shaped

and the effect this has on the overall structure.

3.2 RESULTS AND DISCUSSION

3.2.1 CATALYST AGGLOMERATIONS

Figure 3.1 shows three nuclei particles retrieved from the carbon nanotube growth

furnace. These samples were collected by placing a steel probe into the tube furnace

immediately after the feedstock injector. The material was then scraped from the probe

surface and placed into a glass vial with ethanol and subjected to ultra-sonication with a

150 watt probe operating at 100% power with a one second on and one second off duty

cycle. Specimens were then retrieved with a micropipette and drops were placed onto amorphous carbon coated TEM grids and allowed to dry in air. The samples were then imaged with an FEI Titan high resolution transmission Electron Microscope operating at 300 kV accelerating voltage.

Figure 3.1a shows a catalyst agglomerate made up of a central structure of amorphous carbon that contains iron catalyst particles and nanotubes that protrude radially. There are two well defined carbon nanotube structures. One nanotube grew upwards and to the left and a small bundle of nanotubes grew downwards and to the left. This catalyst agglomerate is an example of a base growth where the catalyst remained anchored and the nanotube grew outward with a closed end cap. In the inset image of Figure 3.1a, the rounded tip of the carbon nanotube is visible. The agglomerate also had many highly distorted tubular structures. However the presence of long range order and well defined wall structure was not observed in the central region.

Figure 3.1b shows an agglomerate where there was a clear distinction between the catalyst containing amorphous carbon core and the protruding carbon nanotubes. There is a bundle of nanotubes that grew downward and to the left by tip growth. The lower right inset image shows an image of one of these tip grown nanotubes. The upper left inset image of Figure 3.1b shows an assortment of other early stage carbon nanotubes with catalyst particles of various shapes (arrows). Most of these short
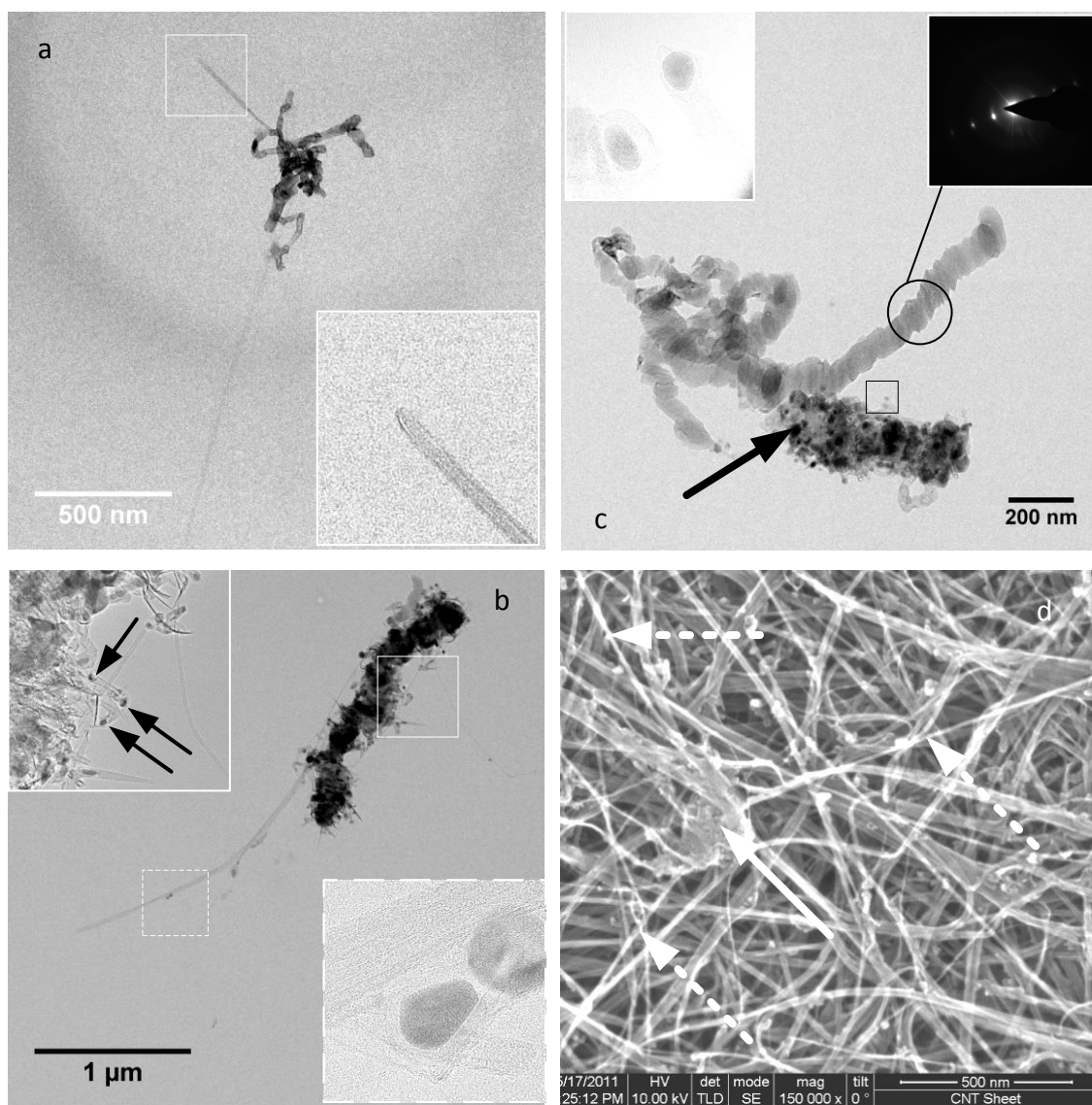
Figure 3.1: CNT catalyst agglomerate. a) agglomerate with base growth, b) agglomerate with tip growth and many short and poorly formed nanotubes, c) agglomerate with graphite nano particles and only isolated short CNT growth (arrow points to catalyst) and d) agglomerate (solid arrow) on surface of CNT sheet with protruding CNTs (dashed arrows)

nanotubes were base growth nanotubes indicating that tip grown and base grown nanotubes can form from the same catalyst agglomerate.

Figure 3.1c shows a third catalyst agglomerate that contains a region of amorphous carbon with many entrapped catalyst particles and a region of graphite nanoparticles. Within the central amorphous carbon region, the iron catalyst is the dark black spots. One of these catalyst particles is indicated with the arrow. This agglomerate showed no long range carbon nanotube growth and only a couple short carbon nanotubes with a tip grown configuration. The left inset image is a short tip growth nanotube with a distorted structure. In the upper right inset image of Figure 3.1c the diffraction pattern from the region of the graphite nanoparticles is shown. These particles were aligned such that the graphene basal planes were oriented perpendicular to the incident electron beam which was the source of the single family of diffraction. Additionally from the main image of Figure 3.1c the region of graphite nanoparticles had an irregular surface where the edges appeared jagged.

Figure 3.1d shows the surface of a CNT sheet where one of the catalyst agglomerates was identified. The core of the agglomerate is indicated with a solid arrow and three of the many protruding CNTs are indicted with dashed arrows. The iron catalyst particles are not distinguished like they were in the previous transmission electron micrographs. It is presumed that the catalyst is within the amorphous carbon because nanotube growth from an agglomerate was only seen when catalyst particles were present. It

should also be noted that the carbon nanotubes that are directly protruding from this catalyst agglomerate are strait and small diameter indicating the likelihood of them being individual or only a few nanotubes and having low defect density.

The meaningfulness of Figure 3.1 is that the agglomerates are a fundamental structure within the CNT assemblies and that carbon nanotubes grow from and are connected to these particles. Therefore the nuclei can act as an anchor site that fixes the intersection of carbon nanotubes into a set angle. These structures will resist the sliding of nanotubes which will hinder processing for alignment and consolidation.

3.2.2 NANOTUBES

The carbon nanotubes in the assemblies used for this research were grown in a floating aerogel method and it is often cited that the carbon nanotubes produced from this method are on the order of a millimeter in length [176]. This has not been measured in the present research and references could not be found of direct measurement of the length of carbon nanotubes in the Nanocomp material. Searching through literature lead to only one determination of the length of the nanotubes from the aerogel growth process. This was reported in the supplementary material of the paper by Koziol et al. [176]. The authors found a single nanotube on a TEM grid and by tracking the single nanotube determined it was 950 µm in length. Perhaps a better indication of the nanotube length is from [241] where a model was developed for the CNT length considering shear between CNTs. The model was compared with data from

forests of different length nanotubes that were fashioned into yarns and were then tested to determine tensile strength. This resulted in a linear relationship between tube length and tensile strength which suggests the length of the CNTs used for the present research are approximately 500 – 700 μm based on typical strength values around 1 GPa.

In Figure 3.2 transmission electron micrograph images of carbon nanotubes are shown to demonstrate the typical structure observed in the CNT assemblies. Figure 3.2a demonstrates three carbon nanotube with diameters of 2.4, 2.4 and 1.8 nm from left to right. These nanotubes had occasional splotches of amorphous carbon like the one indicated with the arrow. In Figure 3.2b a single carbon nanotube is shown. The diameter of this nanotube is 5.4 nm. Figure 3.2 is shown because the nanotubes are representative of the carbon nanotubes observed in the assembly. Most of the observed tubes were in the range of 3-5 nm with a few walls. There are instances where the tubes are larger and smaller but they are less common. Since the tubes are multiwall and are of diameters greater than 3 nm, determining diameter from the Raman radial breathing modes is not useful. The radial breathing modes that are visible represent only SWNTs which is a small fraction of carbon nanotubes. Figure 3.3b shows the Raman spectrum radial breathing modes for the carbon nanotube sheet used in this research. The RBM peaks can be used to measure the diameter of the nanotubes [73]. The peaks at 171 and 234 cm^{-1} correspond to nanotubes of 1.5 and 1.1 nm outer
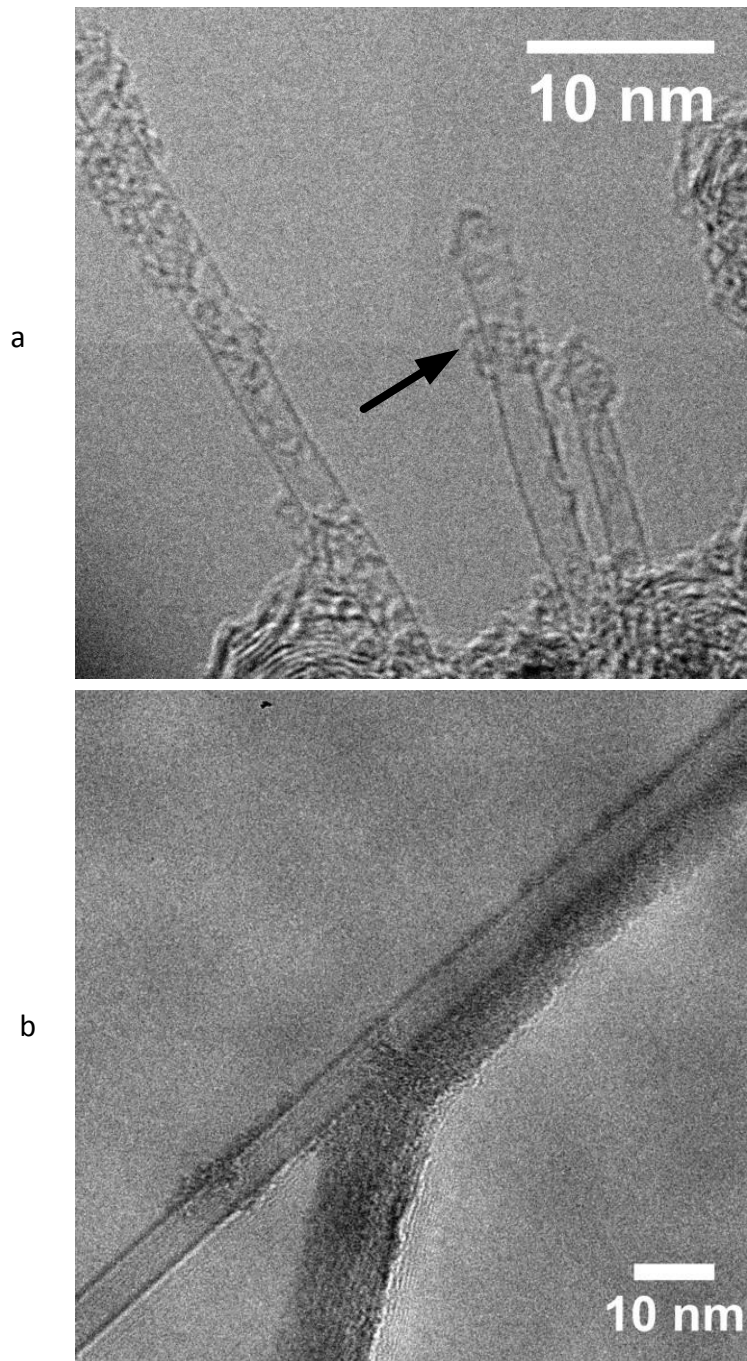
Figure 3.2: Nanotubes in Nanocomp material. a) Examples of single wall nanotubes with amorphous carbon indicated with an arrow and b) Few wall nanotube with 5.4 nm diameter.
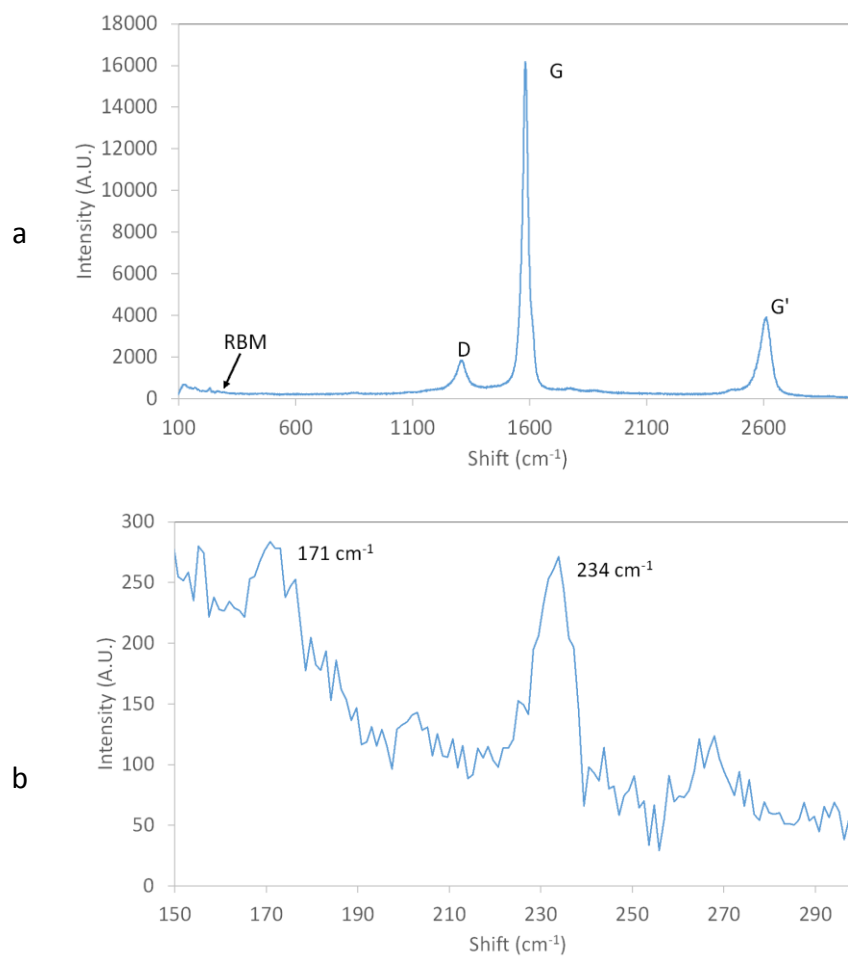
Figure 3.3: Raman peaks from CNT sheet: a) Raman spectrum with small RBM peaks and D, G and G' peaks. b) Magnification of the two RBM peaks

diameter, respectively. However, the RBM peaks only correspond to the small diameter

SWNTs which are not common given the low intensity of the RBM peaks in Figure 3.3a.

3.2.3 BUNDLES AND BRIDGES

The individual carbon nanotubes within the CNT assemblies adhere to their

neighbors to form bundles and as these bundles split and converge with other bundles

they form bridges that hold the network together. Figure 3.4 shows a typical

micrograph of CNT bundles and the bridges these bundle form to interconnect the

structure. These bundles ranged in size from 4 nm to 65 nm with an average of 22nm.

Two clear bridges are indicated with arrows where a small bundle splits from a larger

bundle an joins a neighbor. The structure is clear of large agglomerations of amorphous

carbon and catalyst, except for a small particle indicated with dashed arrow. The

structures in Figure 3.4 demonstrate the tortuous arrangement of the CNT assemblies

where bundles of nanotube are able to bend 90° or more in a tight radius.

3.2.4 ASSEMBLIES

There are three type of assemblies that are of interest to the present research and

they are sheets, ribbons, and yarns. Cross-sections of these three assembly types are

shown along with inset micrographs demonstrating their structure in Figure 3.5. Figure

3.5a shows a CNT sheet that had random orientation of CNTs and high porosity. The

cross section of the CNT sheet showed substantial porosity which was estimated at 80%
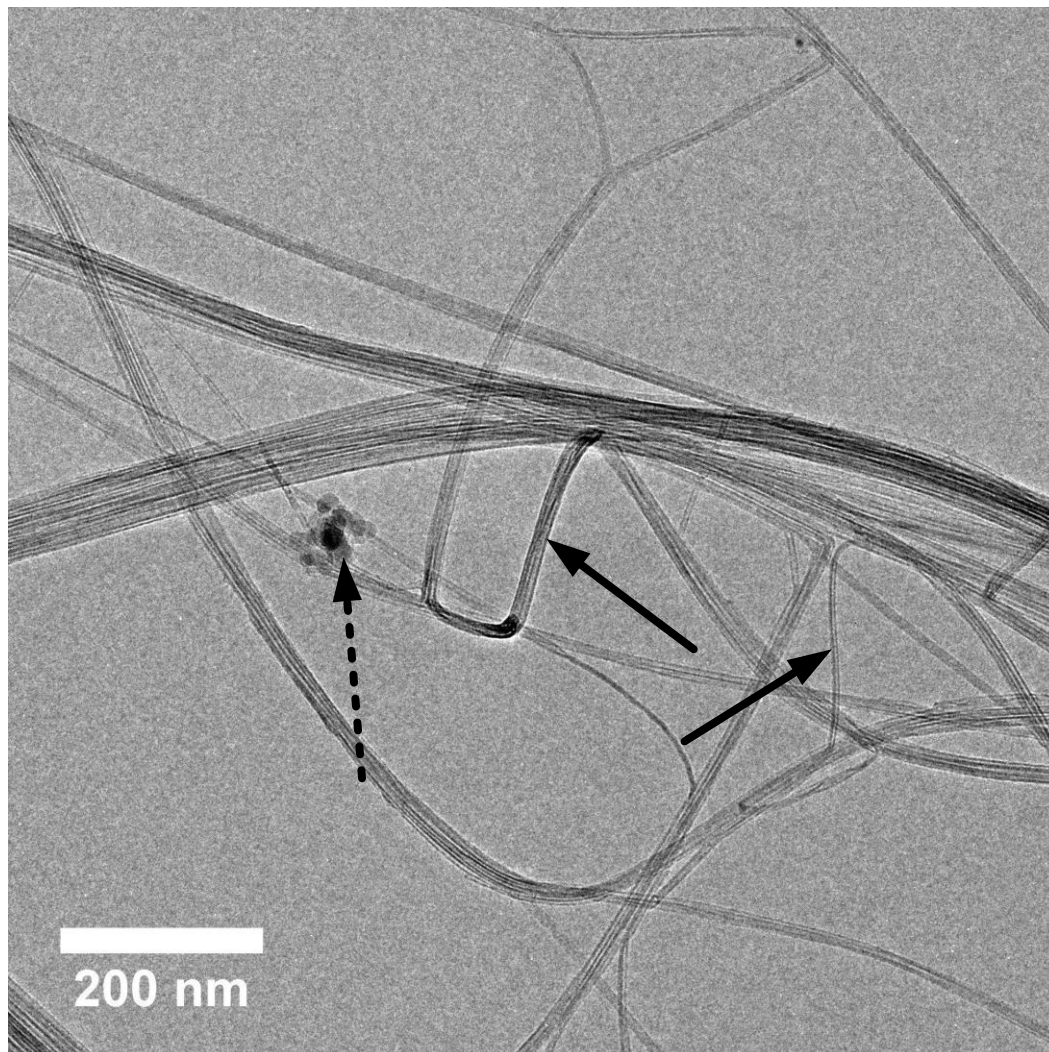
Figure 3.4: Bridges between CNT bundles. Solid arrow point to bridges that interconnect larger bundles and dashed arrow points to catalyst agglomeration.
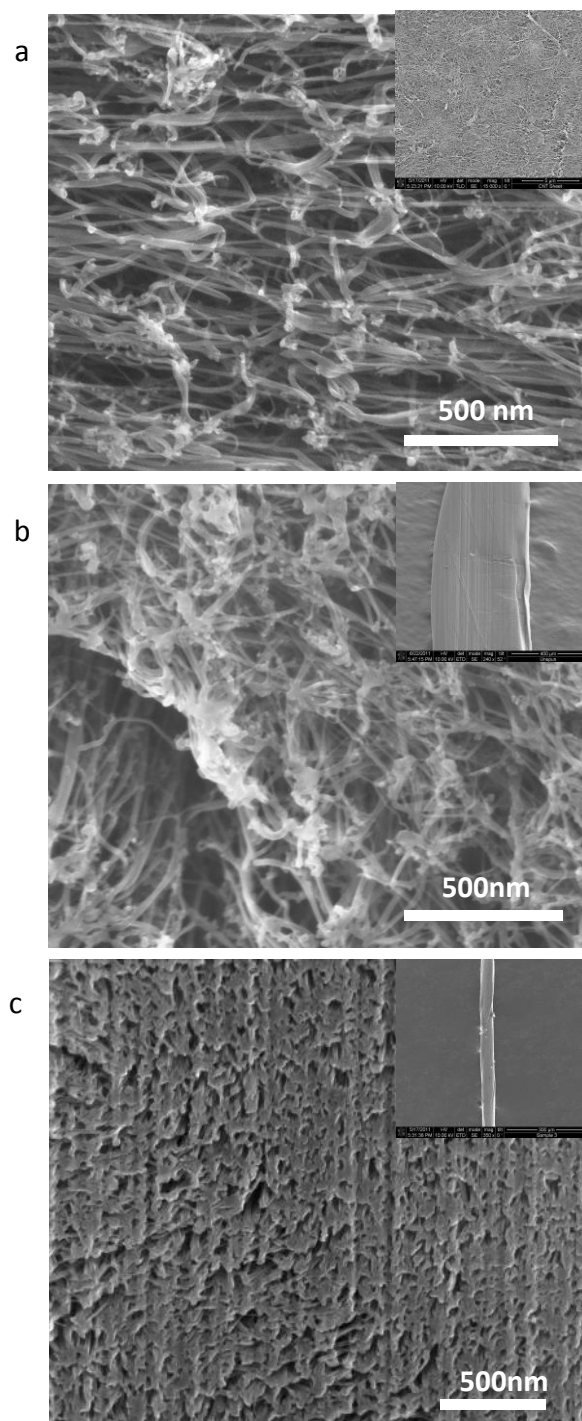
Figure 3.5: Assemblies of carbon nanotubes. Cross sections are shown with inset images of the surface for a) sheet b) ribbon and c) twisted yarn.

by image area analysis. However this value for sheet porosity can vary substantially

depending on the amount of pressure used to compress the sheet. Figure 3.5b shows a

cross sectioned CNT ribbon which is the material produced directly from CNT growth

furnace by collapsing the aerogel sock into a fiber. This particular sample was

approximately 20x500 μm but the width and thickness is variable. Reflecting the

aerogel sock collapse in the fiber production method, the CNT assembly shown in Figure

3.5b had lower porosity in comparison to the sheet material. In this particular sample

the porosity was 50% but again this is an approximation to demonstrate the reduced

porosity in CNT ribbons. The cross-section of a CNT yarn which was produced by

twisting a ribbon into a circular structure is shown in Figure 3.5c. The diameter of the

yarn was approximately 50 μm. In the image, the porosity was determined to be 20%.

It was reasonable for the porosity to be reduced in the twisted yarns as the twisting

process imparts a radial compression. This pushes the CNTs into contact where van der

Waals forces can maintain the new configuration.

3.6 CONCLUSION

The carbon nanotube assemblies used in the present research are made by a floating

catalyst aerogel processes. The materials are formed into sheets, ribbons and yarns by

the interconnected network of nanotubes formed by van der Waals driven bundling.

The nanotube material contains large agglomerations of catalyst and amorphous carbon

but the structure is generally clean away from these features. The network can be

thought of as a three dimensional fishing net where the CNTs are the filaments and the

"knots" are the catalyst agglomerations.

CHAPTER 4: PROGRESSION OF ALIGNMENT IN STRETCHED CNT SHEETS DETERMINED BY WIDE ANGLE X-RAY SCATTERING.

4.1 INTRODUCTION

Individual carbon nanotubes (CNTs) have shown exceptional mechanical properties [10]. These properties are a result of their unique structure and high aspect ratio, which has led to extensive efforts to incorporate them into composites [245]. When assemblies of CNTs are processed to make macroscopic structures, the strength is low, and strongly depends on the alignment of the nanotubes. This alignment serves multiple roles. The nanotubes orient such that stresses are distributed along their strong axial direction. They are packed tighter together so that the material fits into a smaller cross-sectional area. Furthermore, the alignment promotes greater contact area between nanotubes, which will increase load transfer throughout the network.

Carbon nanotube growth methods have a significant impact on alignment. The first approach used to produce carbon nanotubes [3] was an arc discharge between carbon electrodes. This method generated a coating of CNT on the cathode and, when collected, a randomly arranged powder was obtained [246]. Lower temperature growth methods, such as HiPCo [165] and CoMoCAT [148], are also available that utilize chemical vapor deposition (CVD) on transition metal catalysts to produce CNT powders. To form a continuous network of CNTs a CVD process has been reported [175] that uses

a "floating catalyst". This method produces an aerogel sock of millimeter long

nanotubes that may be drawn into sheets and yarns. However, there is still widespread

misalignment of the nanotubes [42]. One method to form aligned CNTs is to grow them

from a catalyst on a planar surface to form a structure that resembles trees in a forest

[201, 247]. By adjusting the growth parameters, including temperature, flow rate,

feedstock and catalyst composition, the vertical alignment can be controlled [154].

However, the growth rate slows with length, and because this arrangement does not

have planar alignment, these materials are not well suited for incorporation in laminar

composites.

Researchers have investigated many methods of post processing carbon nanotubes

to increase alignment. Hone et al [238] formed sheets of aligned CNTs by filtering

dispersed solutions in a strong magnetic field. They found that the electrical

conductivity varied by 24x perpendicular and parallel to the magnetic field. Vigolo et al.

[193] extruded dispersed solutions of CNTs through a syringe needle to form fibers.

Zhang et al. [203] used a process of drawing and twisting CNT arrays into consolidated

fibers. Bradford et al. [240] developed a process that resembled felling a forest of CNT

trees at the same time and in the same direction, to form aligned sheets. Cheng et al.

[216] employed mechanical stretching to align CNT sheets. These sheets were produced

by the floating catalyst method and were stretched before infusion with bismaleimide

resin. With so many methods available to align the carbon nanotubes, it is important to have an unambiguous method of characterizing the resultant structure.

A technique that is commonly applied to determine the structure of polymer films and fibers is wide angle X-ray scattering (WAXS). This method passes x-rays directly through a specimen to measure its crystal structure [223]. Nanotubes are well suited for WAXS because they are primarily found in bundles where the graphitic CNT walls flatten when contacting neighbors [84-86, 248]. These flattened walls produce the (002) reflections that directly correlate with the alignment of the nanotubes. Zhang et al. [249] used WAXS with copper K_α radiation to characterize the structure of CNT fibers that were coated with crystallized polyethylene. The primary diffraction peaks were produced by the polyethylene, but a peak attributed to CNT was located at $2\Theta = 25.5°$. Behabtu et al. [200] produced CNT fibers from a dispersion that was extruded through a spinneret into a coagulation bath. The diffraction peak for the CNTs was at $2\Theta = 25.3°$ and the full width at half maximum (FWHM) was 9.4°. Furthermore, the Hermans orientation factor (HOF) [250], which is an average of cosine alignment, was 0.96. The HOF has three characteristic values: an HOF of 1.0 corresponds to perfect alignment, 0.0 is random, and -0.5 is perfect transverse alignment. Futaba et al. [222] used WAXS and polarized Raman to characterize CNT arrays that were modified into various shapes by solvent consolidation with lithographic patterning. They demonstrated an HOF of 0.72

and 6.8x optical anisotropy in polar plots of the G peak intensity from Raman spectroscopy.

In this research, we systematically investigate the progression of CNT alignment in response to mechanical stretching. X-ray diffraction data is reduced to histograms and polar plots that give the distribution of oriented CNTs as a percentage of the total. This demonstrates the rearrangement that occurs when nanotube sheets are stretched to failure. Electron microscopy is also used to characterize the structural features that evolve during stretching.

4.2 EXPERIMENTAL METHODS

4.2.1 MATERIALS

Carbon nanotube sheet was received from Nanocomp Technologies Inc. (Merrimack NH). The sheet was produced by a aerogel CVD process similar to that of Cambridge University [175], where a floating nanotube aerogel, grown with an iron catalyst, was collected onto a rotating drum [251]. The drum was rotated at a surface velocity of 14.8 meters per minute to impart alignment in the drawing direction. The sheet was built up, layer by layer, until approximately 15 grams per square meter of material had accumulated.

Samples were cut from the sheet at 0°, 10°, 25°, 45° and 90° with respect to the drawing direction. The specimen were cut to a width of 5 mm and length of 30 mm.

The thickness was approximately 100 μm.   These samples were mounted to card stock paper frames with a 20 mm gauge length. Samples were also produced by mechanical stretching at 5 mm/min to generate alignment in the CNT network. These samples, which were also mounted in the paper frames, were stretched in a tensile fixture after cutting the frame. They were stretched to 5%, 10%, 20% and 30% strain, depending on the level of elongation that could be accommodated before failure. The paper frames where then rebuilt by adhering paper across the cut lines in the frame to maintain the elongation during further characterization.

4.2.2 CHARACTERIZATION

Thermogravimetric analysis (TGA) was performed with a TA Instruments Q50 at a ramp rate of 10 °C/min from 20 to 800 °C. The samples were placed in platinum pans and 100 mL/min of gas flowed over the samples with a 10:90 composition of nitrogen and air. The mass loss data along with its derivative were plotted versus temperature.

An Instron 5966 universal test system was used to evaluate the mechanical properties of the CNT sheets. Loads were applied at 5 mm/min with a 500 newton load cell, and stresses were calculated based on the measured cross-sectional area of the sample. The tensile strength was defined as the maximum stress achieved in each test. The modulus of the CNT structure was calculated based on a linear fit to the stress versus strain curve between 10% strain and the strain at failure, i.e. at the maximum stress recorded prior to sheet cleavage.

Electron micrographs were obtained with an FEI Nova 600, dual beam, high resolution scanning electron microscope (HRSEM). The system was operated in field immersion mode at 10 kV accelerating voltage, 0.54 nA beam current and a working distance of 5 mm. Wide angle X-ray scattering was performed on a Rigaku R-Axis SPIDER that had a cylindrical area detector with a radius of 127.4 mm and 100 μm x 100 μm pixel size. The system utilized a 2.0 kW copper source with a graphite monochromator and a 0.3 mm double pinhole collimator. It was operated at 50 kV and 40 μA to generate two dimensional intensity images. These images were then analyzed with AreaMAX 2.0 to generate integrated 2Θ and χ spectrums.

The χ spectrums were used to analyze the orientation of CNTs within the sheets. The background was subtracted by linear interpolation using 15° and 35° as the bounds and 25.8° as the centers of the azimuthal data. The integration was performed radially at ±1° in 2Θ and the spectrums, arranged circumferentially, spanned over 180° azimuthal angle in the left half of the WAXS image. This azimuthal data was then processed to form histograms and polar charts. For the histograms, the azimuthal data is folded at 90° where the intensities are added and then normalized into 5° bins showing the distribution of CNTs as a percentage of all CNTs sampled. The polar charts give the radial distribution where the azimuthal intensity at 2Θ = 25.8° is normalized and transformed into 5° increments from 0° to 180°. These charts illustrate the percentage

of CNTs oriented in each direction. To make the plot easier to interpret the radial data

was mirrored across the origin to produce a 360° distribution.

4.3 RESULTS

4.3.1 STRUCTURE OF CNT SHEETS

The thermogravimetric analysis of the CNT sheets is shown in Figure 4.1. The B curve

is the mass loss and the O curve is the derivative of the mass loss. Up to 450°C, the total

mass decreases by 4%, which is attributed to amorphous carbon present in the

specimen. This is generally considered to burn off below 400°C [252]. The first peak

due to this gradual burn off is located at 320°C in agreement with other findings [253,

254]. Between 450 °C and 800 °C, the mass drops to 12.9% of the total originally

present. The remaining material is Fe_2O_3 which indicates there is 9.7 wt% iron catalyst

in the CNT sheet. The derivative mass loss shows three additional peaks, located at 573,

642 and 690 °C, constituting 19%, 30% and 47% of the carbon material, respectively.

These peaks are attributed to different types of nanotubes, which will be discussed in a

later section.

Figure 4.2 is provided to demonstrate the structure of the CNT sheet before

deformation. It shows a high magnification micrograph of the surface of a 0° sample

arranged such that the vertical direction is the drawing direction. Individual nanotubes

are not observed, instead bundles can be seen approximately 35 nm in diameter on

average.   There is no obvious alignment of the CNT network. Samples cut at 10°, 25°,
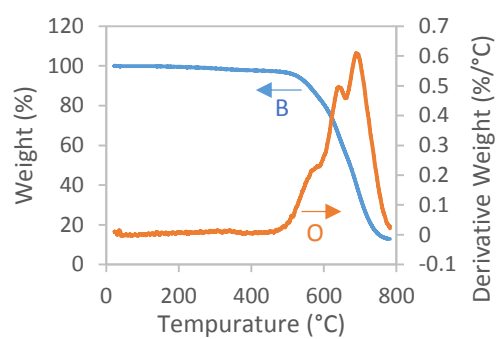
Figure 4.1: Thermogravimetric data for CNT Sheets. The blue (B) is mass loss and the orange (O) curve is derivative mass loss.
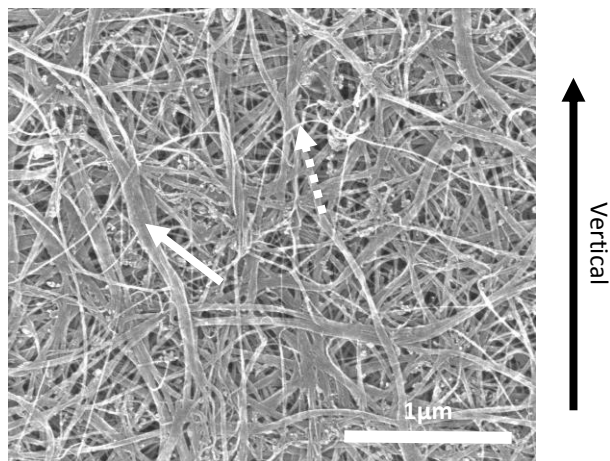
Figure 4.2: Surface of CNT sheet as received. Vertical direction is the drawing direction. The arrows indicate bundles of nanotubes.

45°, and 90° to the drawing direction have a similar arrangement of nanotubes, where the only difference is that the structure is rotated by the corresponding cut direction. The solid arrow points to a large bundle of nanotubes, and the dashed arrow points to a small bundle.

In Figure 4.3, X-Ray data is shown from a CNT sheet that has been stretched to failure. The two dimensional intensity map from the WAXS analysis is shown in Figure 4.3a. The peak at the center (i) is small angle scattering from the (10) hexagonally packed nanotubes. The inner ring of intensity (ii) corresponds to the (002) spacing between the graphitic planes of nanotubes. The outer ring (iii) corresponds to diffraction from the residual catalyst. Figure 4.3b shows the integrated two theta spectrum from the left side of the two dimensional intensity map in Figure 4.3a. The integration bounds are radially between 5° to 50° 2Θ, and circumferentially between 85° to 95° χ, where 0° χ is at the top of Figure 4.3a. The primary peak, located at 2Θ = 25.8°, corresponds to the (002) graphitic plane spacing at 3.45 Å. This agrees with previously published results, where 3.44 Å was found [255]. The diffraction intensity between 2Θ = 42° and 47° is assigned to residual catalyst in the form of Fe_3C. The five most intense reflections from Fe_3C have 2Θ values of 45.0°, 43.8°, 42.8°, 44.6°, and 45.8° [256]. Additionally, graphite has a 101 reflection at 44.3° for copper K_α radiation. Finally, the peak near 5° is from small angle scattering by the (10) hexagonally packed CNT. The intensity drops on the left side of the peak as a result of the beam stop used to block the

112
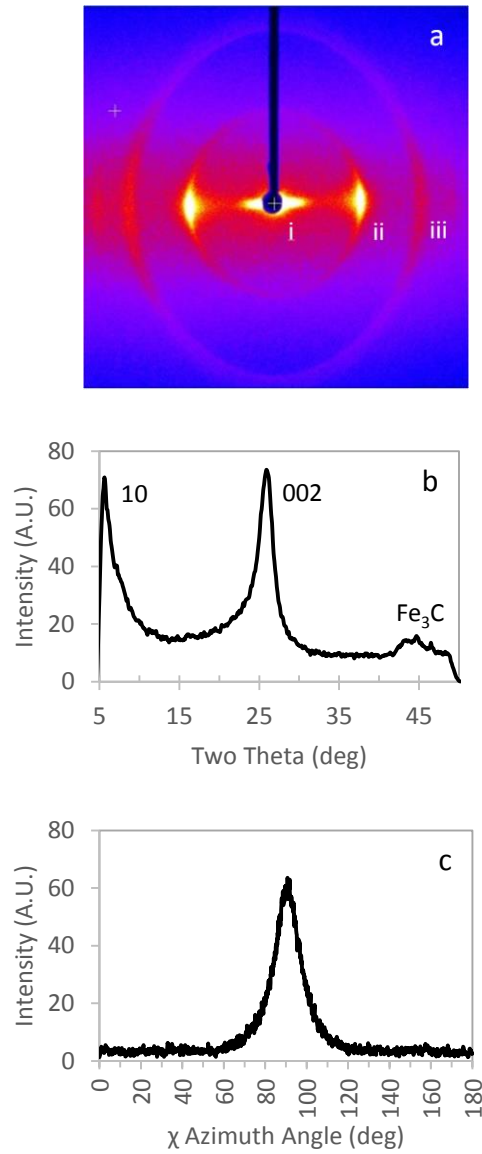
Figure 4.3: X-Ray data from stretched CNT sheet. a) Two dimensional intensity map from WAXS. b) Integrated two theta intensity spectrum. c) Integrated intensity of 002 peak around χ in the left hemisphere.

transmitted beam. The azimuthal χ spectrum, integrated circumferentially around the left half of the (002) diffraction ring, is shown in Figure 4.3c. In this spectrum, the peak is located at 90° and has a FWHM of 14.2° when fitted with a Lorentzian curve.

Figure 4.4 shows the distribution of nanotube orientations when cutting the sheet along the drawing direction (0°). In this histogram, the vertical axis is the fraction of total nanotubes in the sample, and the horizontal axis is the angle between the drawing direction and the diffracting CNTs. The bins of the histogram indicate the percentage of nanotubes that were oriented, with respect to the drawing direction, between the upper and lower bounds of each 5° bin. The dotted horizontal line is located at 5.55%, which indicates the fraction for a random distribution. In this sample 14.3% of the nanotubes are within ±10° of the cut direction, and the HOF is 0.075. The histogram for samples cut at 10°, 25°, 45° and 90° to the drawing direction show approximately the same level of alignment. However, the alignment was shifted such that a sample cut at 90° would have 7.6% of the nanotubes are within ±10° of the cut direction.

4.3.2 MECHANICAL PROPERTIES

Figure 4.5 shows stress versus strain curves for the five sample cut directions. The blue (B), red (R), green (G), violet (V) and orange (O) curves correspond to the 0°, 10°, 25°, 45° and 90° samples, respectively. Each curve is the average of at least 4 individual samples. This Figure reveals the increase in strain to failure and reduction in modulus as the sample cut angle increases. Bar charts showing the tensile stress, stiffness and
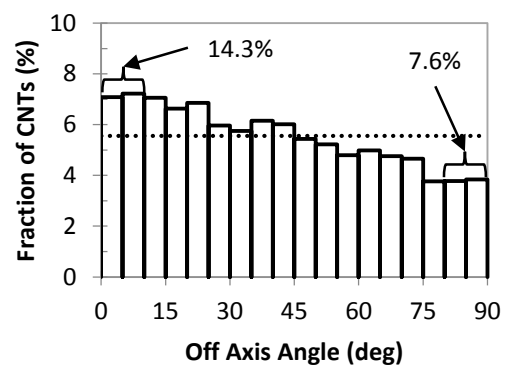
Figure 4.4: Histogram for distribution of CNTs as received in 0° ply. The horizontal dotted line at 5.55% indicates the location for perfectly random alignment.
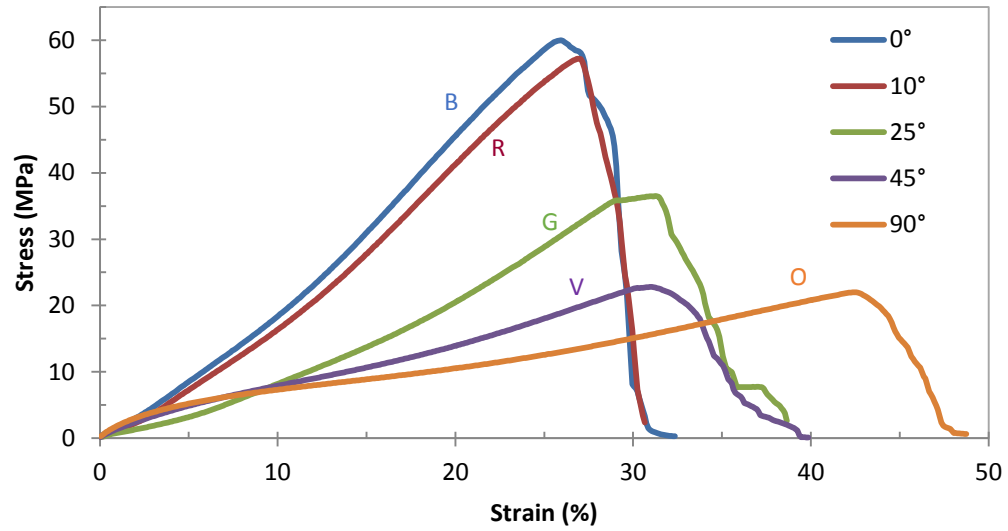
Figure 4.5: Stress vs strain curves for the five off axis ply orientations. The blue (B), red (R), green (G), violet (V) and orange (O) curves correspond to 0°, 10°, 25°, 45°, and 90° samples respectively.

strain at failure for the five orientations are presented in Figure 4.6. The mechanical

properties are summarized in Table 4.1. The peak stress of sheets cut at the five

different orientations are shown in Figure 4.6a. The highest stress recorded was for the

0° sheets at 63.4±2.8 MPa. The stress drops from 58.0±2.1 to 40.6±3.4 to 24.3±3.0 to

22.6±0.5 MPa as the cut angle increases from 10° to 25° to 45° to 90°. The modulus

(Figure 4.6b) shows a similar trend, falling from 271±11 MPa for the 0° orientation to

47±1 MPa for the 90° orientation. On the other hand, the strain at failure increases

from 27.6% at 0° to 43.8% at 90°. The strain at failure of the 0° and 10° samples were

equivalent within standard deviation, as were the 25° and 45° orientations.

4.3.3 ALIGNMENT OF 0° SAMPLES

Figure 4.7 shows electron micrographs of 0° samples before testing (Figure 4.7a) and

after 5% strain (Figure 4.7b). Prior to stretching, the surface had many subtle wrinkle

lines and a few large creases like the one indicated with an arrow in Figure 4.7a. In

between these features, the structure had a uniform matted surface. The inset

micrograph shows high magnification of the surface before stretching, in which no

obvious alignment is observed. In Figure 4.7b, after 5% elongation, the subtle wrinkles

are gone, and only the large crease lines remain (indicated by an arrow). Again the inset

is a high magnification of the surface which shows no apparent alignment. The effect

the wrinkles and creases have on the mechanical properties will be discussed later.
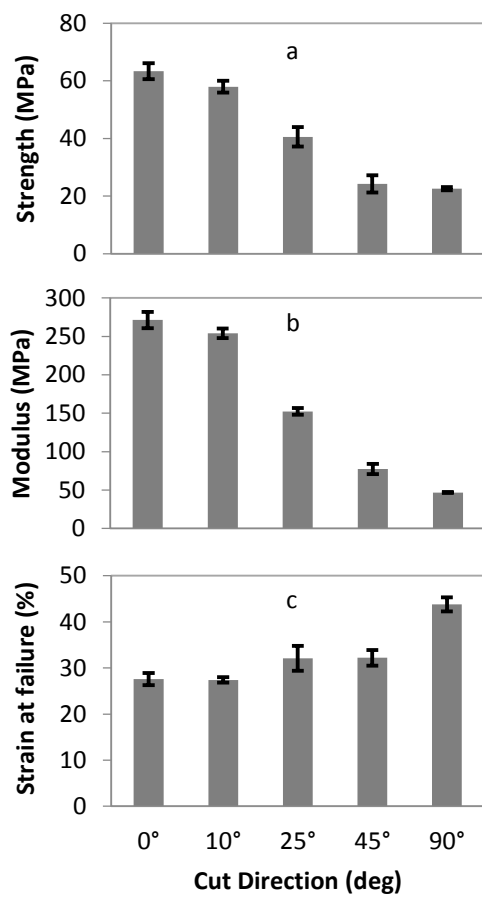
Figure 4.6: Mechanical properties of CNT sheets versus sample cut direction: a) The peak stress at failure. b) The modulus measured from the slope between 10% elongation and failure. c) The strain at failure.

Table 4.1: Effect of cut angle on the mechanical properties and alignment of CNT sheets.   ** Value measured after failure

| Cut Angle | Tensile Strength | Modulus | Strain at Failure | Density** | HOF** | ±10° Aligned** |
Degrees	MPa	MPa	%	g/cm³	--	%
0	63.4 ± 2.8	271 ± 11	27.6 ± 1.3	0.37 ± 0.01	0.24 ± 0.001	50 ± 0.7
10	58.0 ± 2.1	254 ± 6	27.4 ± 0.6	0.42 ± 0.05	0.30 ± 0.004	52 ± 0.5
25	40.6 ± 3.4	152 ± 4	32.1 ± 2.7	0.40 ± 0.03	0.24 ± 0.002	51 ± 1.2
45	24.3 ± 3.0	77 ± 7	32.2 ± 1.7	0.31 ± 0.02	0.22 ± 0.008	42 ± 0.5
90	22.6 ± 0.5	47 ± 1	43.8 ± 1.5	0.34 ± 0.01	0.22 ± 0.05	41 ± 0.6
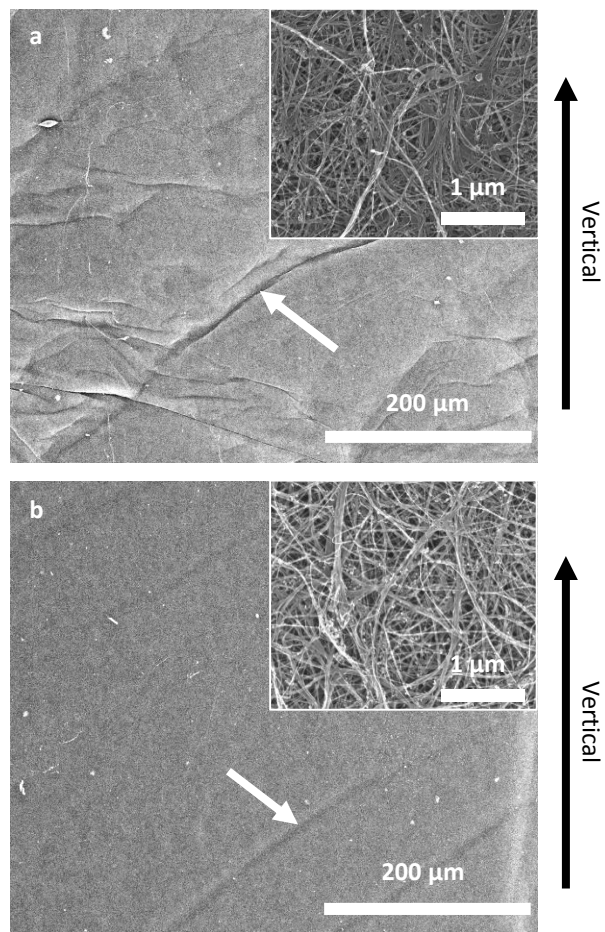
Figure 4.7: SEM micrographs of the 0° sample surface. a) Sheet as received. b) After 5% elongation in the vertical direction.

Figure 4.8 shows the alignment achieved when stretching a 0° sample to failure. The

micrograph in Figure 4.8a reveals the orientation of the nanotube bundles after being

stretched to failure in the vertical direction. The location investigated in the micrograph

is away from the fracture tip to demonstrate the maximum alignment achieved.   The

bundles align vertically with extensive wall-to-wall contact. There are, however, a few

kinked CNT bundles, such as the one indicated by the arrow. The histogram in Figure

4.8b reveals the corresponding distribution. In this case, 50% of the nanotubes are

oriented within ±10° of the stretching direction. The samples with cut direction of 10°

and 25° have similar levels of alignment, with 52% and 51% of the nanotubes orientated

within ±10° of the stretching direction, respectively (c.f, Figure 4.4). This may be

compared to 14% alignment when no mechanical stretching has been performed.

4.3.4 ALIGNMENT OF 90° SAMPLES

Micrographs of the surface of 90° samples before testing and after 5% strain in the

vertical direction are shown in Figure 4.9. The inset micrographs correspond to high

magnification images of the sheet surface. The unstrained sample in Figure 4.9a

exhibits a matted surface with wrinkles. There are also creases, as indicated with a

broken arrow. The sample strained to 5% elongation, Figure 4.9b, shows multiple

streaks along the stretching direction, as indicated with a solid arrow. These streaks are

waves produced by transverse compressive stress. The period of the wave formation is

approximately 70 μm in the direction perpendicular to stretching.
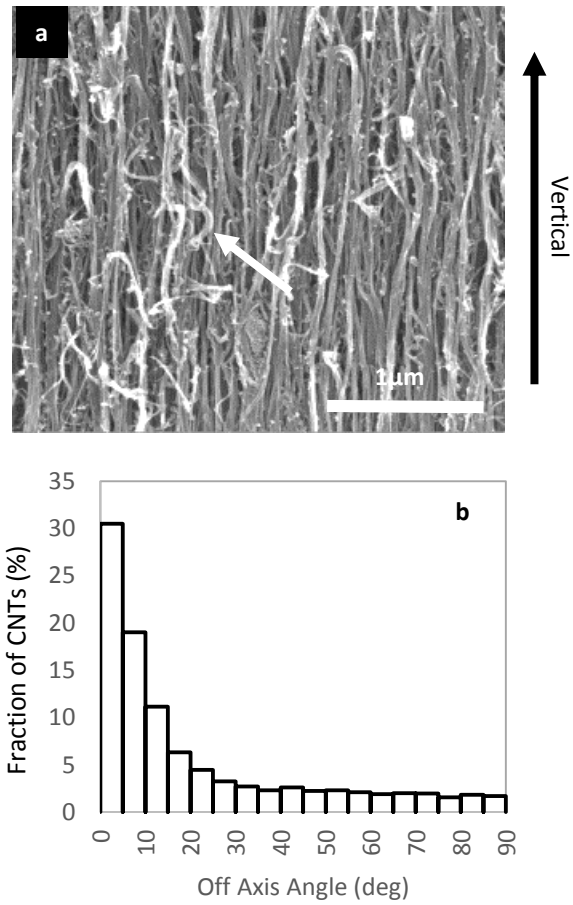
Figure 4.8: Alignment of CNT sheet at failure for samples cut at 0°: a) micrograph b) histogram
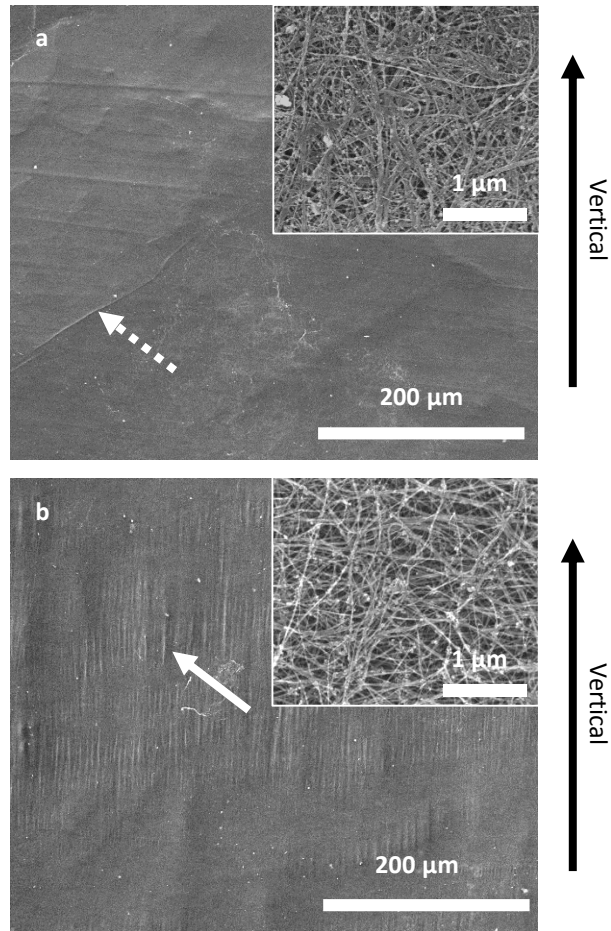
Figure 4.9: SEM micrographs of the 90° sample surface. a) Sheet as received. b) After 5% elongation in the vertical direction.

Figure 4.10 shows the alignment obtained when stretching the 90° sample to failure in the vertical direction. The micrograph in Figure 4.10a reveals the sheet surface at high magnification in an area away from the fracture tip. In this instance the nanotube bundles have a chaotic arrangement that contains many kinks between oriented bundles. The arrows trace a bundle of nanotubes that bent back and forth twice at an angle of nearly 180°. A dashed circle also highlights another instance of a bundle with two 180° kinks in close proximity. The structure appears more porous than the 0° sample, which agrees with the reduced density at failure (see Table 4.1). The histogram in Figure 4.10b shows the angular distribution of carbon nanotubes in the 90° sheets when stretched to failure. In these samples, 41% of the nanotubes are oriented within ±10° of the stretching direction. Furthermore, the samples cut at 45° to the drawing direction had 42% of the nanotubes within ±10° of the stretching direction (see Table 4.1). This represents 10% less orientation than the 0°, 10° and 25° samples when stretched to failure.

4.3.5 Rearrangement of CNTs during Stretching

Polar plots are presented in Figure 4.11 for the 360° orientation distribution of 0°, 45°, and 90° samples before stretching, with 10% strain, and when strained to failure. The plots demonstrate the progression of CNT alignment with respect to the vertical stretching direction. The distance from the center is the magnitude of alignment and it corresponds to the percentage of nanotubes oriented in a particular radial direction.
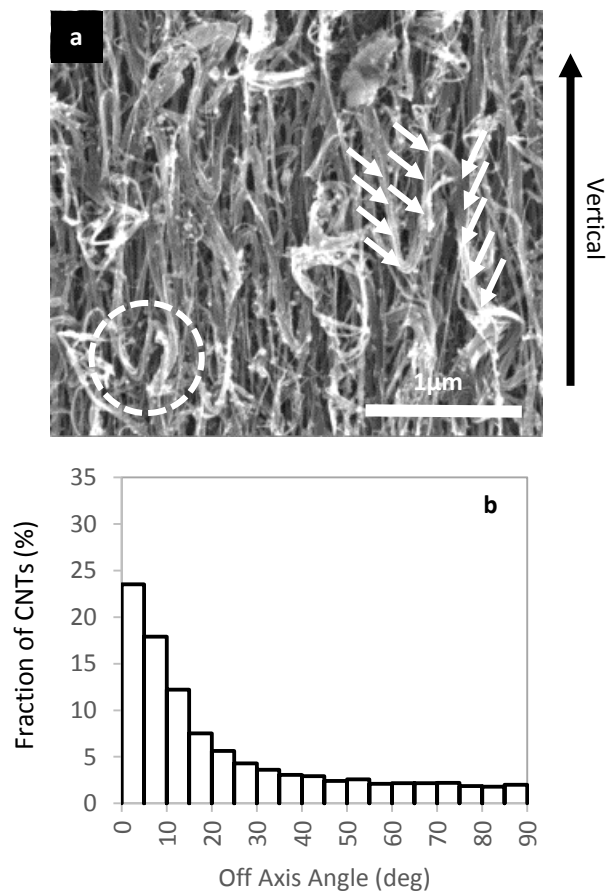
Figure 4.10: Alignment of CNT sheet at failure for samples cut at 90°: a) micrograph b) histogram
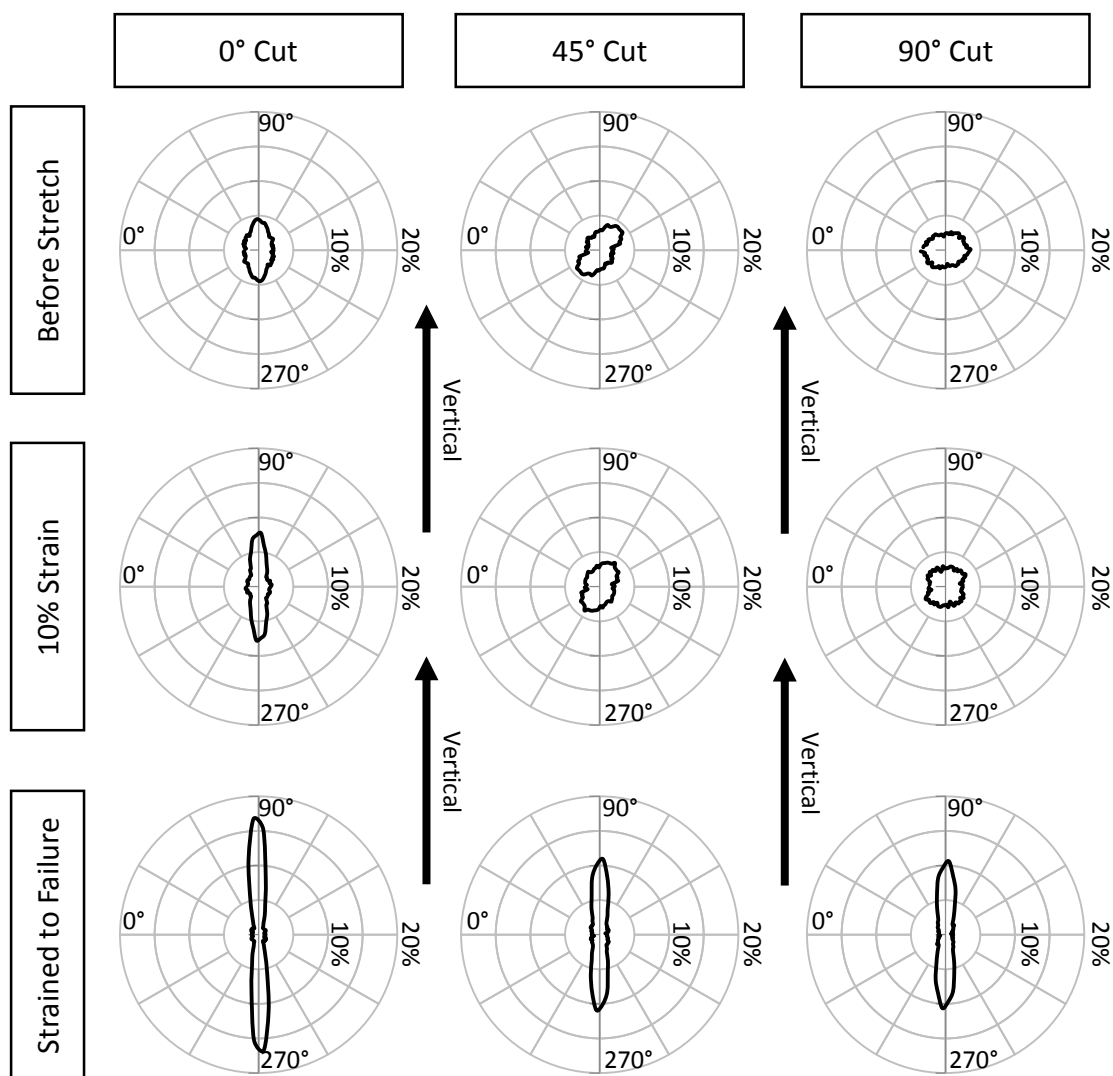
Figure 4.11: Polar orientation plots showing the progression of CNT alignment for samples with cut directions of 0°, 45° and 90°.

Rings are used to segment the magnitude into 5% increments. The radiating lines are at 30° increments around the plot. The percentage of CNTs in each direction has a lower magnitude than the histograms in Figure 4.8 and Figure 4.10, because the polar plots are differentiating between positive and negative orientations with respect to the stretching direction. The plots are also mirrored across the origin to provide a better sense of the 360° arrangement of nanotubes.

The unstrained 0° sample in the top left corner shows a slight initial orientation in the drawing direction with a maximum alignment of 4.5% in the 85° to 90° bin. After 10% strain, the distribution of CNTs clearly changes, such that a larger percentage of CNTs are oriented in the vertical stretching direction. At failure, the lower left plot shows the nanotubes have oriented towards the stretching direction at a peak magnitude of 17%. The 45° and 90° samples, center and right column, respectively, exhibit an indirect path towards alignment when stretched. In these plots, going from the initial structure to 10% strain in the top and middle rows results in little change in maximum alignment. The 45° sample has 4.3% maximum alignment in the 125° to 130° bin. This dropped to 4.1% in the 120° to 125° bin after 10% strain. The 90° sample has a maximum alignment of 3.6% in the 175° to 180° bin. This reduced to 3.4% in the 145° to 150° bin after 10% strain. At failure the alignment in a single direction for the 45° and 90° samples reaches maxima of 13.7% and 12.1%, respectively. This analysis was also carried out for 10° and 25° samples. In these instances, the 10° sample behaves like the 0° sample, but with the

small reorientation occurring at strains of 5%. The 25° sample shows behavior more like that of the 45° and 90° samples, where rearrangement of the CNT bundles occurs before alignment of the network in the vertical direction.

4.4 DISCUSSION

4.4.1 CARBON NANOTUBE MATERIAL

Deconvolution of peaks in Figure 4.1 reveal that the amorphous carbon that burned off below 450°C only amounts to 4% of the carbon in the sample. The three peaks located at 573, 642 and 690 °C are attributed to three different types of carbon nanotubes. This is in spite of the fact that the peak at 573 °C is near the 565 °C burn off point for carbon soot [191, 257]. This is because the 573 °C peak accounts for 19% of the mass and this amount of soot would have been evident in microscopy. The assignment agrees with previous work [258], where CNT produced by CVD growth with xylene and ferrocene had a TGA peak at 580 °C. These researchers found that a 1600 °C anneal increased the decomposition temperature of their multiwall nanotubes to 625 °C. Whereas 2200 °C and 2800 °C anneals increased the decomposition temperature to 740 °C. Therefore, the three peaks at 573, 642 and 690 °C are due to three grades of CNTs that grow simultaneously. It is postulated that higher decomposition temperatures would result from nanotubes with fewer defects.

4.4.2 ALIGNMENT

In spite of the modest alignment of the sheet as received (14% aligned to ±10°), the strength of the 0° sheet is 1.8x higher than the 90° sheet and the modulus was 4.9x higher. Stretching in the 90° direction was originally envisioned as a method to make CNT sheet processing less laborious by choosing processing directions that had lower resistance to deformation. After this work it is clear that, in spite of less resistance to deformation and higher elongation before failure, the final alignment is inferior. Although the 90° and 45° samples achieved less alignment prior to failure, the alignment did appear to be a good indicator of when the CNT sheet reaches the limits of deformation. This is exemplified in the first 10% of elongation of the 90° samples, which exhibit little change in alignment in the polar plots of Figure 4.11. This indicates further deformation is possible. By contrast, the 0° sample is significantly aligned at 10% strain, indicating that there is less elongation available before failure.

4.4.3 DEFORMATION

The observation of crease removal, variation in modulus, and similar levels of alignment at failure leads to the conclusion that deformation of the CNT sheets occurs in three phases. The first is the removal of wrinkles and creases without alignment of the underlying network. The wrinkles are removed before the creases, as shown in Figure 4.7b, but both of these features disappear prior to alignment of the CNT network. Further deformation occurs with rearrangement of the network. This rearrangement

continues until the CNTs are maximally aligned, then there is no other mechanisms

available to accommodate stretching, and the bundles slip apart. The 0° and 10°

samples did not exhibit the first stage of wrinkle and crease pullout. This implies that

the wrinkles and creases are oriented away from this direction so that alignment of the

sheet begins immediately with stretching.

In Figure 4.9, waves in the 90° sample are seen as a result of compressive stresses

transverse to the tensile direction. We believe this deformation results from the slightly

higher concentration of CNTs oriented perpendicular to the stress direction. These

tubes are placed under compression by contraction in this direction. As a result of the

high aspect ratio of the nanotubes, buckling occurs with eventual formation of kinked

structures as seen in Figure 4.10. The packing of the CNTs is hindered by the kinks and

the density of the stretched material is reduced slightly in the 45° and 90° cut samples.

Conversely, the 0° cut samples had only 7.6% of the nanotubes oriented transversely,

which was enough to reduce kinking and improve alignment, density and strength.

4.5 CONCLUSION

Carbon nanotube sheets that were partially aligned by high draw rates during growth

were stretched to failure at 0°, 10°, 25°, 45° and 90° with respect to the draw direction.

It was found that the mechanical properties were highly dependent on the cut direction,

decreasing from a tensile strength and modulus of 63.4±2.8 MPa and 271±11 MPa at 0°

to 22.6±0.5 MPa and 47±1 MPa at 90°. The sheet as received has 14% of its nanotubes

aligned within ±10° of the drawing direction. Stretching to failure in the drawing

direction results in 50% of the nanotube aligning within ±10°. Utilizing wide angle X-ray

scattering as a method to unambiguously determine the alignment of CNT networks

gave insight into how the CNT network deformed in response to stretching.

CHAPTER 5: FABRICATION AND CHARACTERIZATION OF SOLID COMPOSITE YARNS FROM CARBON NANOTUBES AND DICYCLOPENTADIENE POLYMER.

5.1 INTRODUCTION

Carbon nanotubes (CNTs) have a unique structure that could be advantageous in forming high strength composites [245]. The ultimate tensile strength (UTS) of a single wall carbon nanotube has been measured to be 150 GPa [10]. Typical multi-walled carbon nanotubes have strengths between 20 and 80 GPa, Young's modulus between 0.9 and 1.2 TPa, and elongation to failure between 5 and 15% [92]. However, the utilization of these properties is a challenge because van der Walls (VDW) forces are relied upon to transfer load between individual CNTs and macroscopic structures. In the case of continuous CNT assemblies, the structure begins with individual nanotubes that agglomerate into larger bundles [259]. These bundles become interconnected in a loose network that resembles a fishing net [260]. The network extend three dimensionally into macroscopic assemblies such as sheets, yarns, ribbons and foams [261].

Fibrous assemblies of carbon nanotubes were originally prepared from dispersed solutions that were injected with a syringe pump into a moving coagulation bath [193]. This yielded filaments with UTS and Young's modulus up to ~150 MPa and 15 GPa, respectively. Jiang et al. [201] found a more direct fabrication route by growing aligned arrays of carbon nanotubes that form fibers or films when CNTs are drawn from the

array. Zhang, Atkinson and Baughman [204] incorporated twist, which stabilized and consolidated the structure, to produce nanotube yarns with ultimate tensile strength over 480 MPa. The mechanical properties were boosted by consolidation because the contact area between nanotube bundles increased such that load transfer through VDW forces improved. This consolidation is often achieved through twisting [184], but can also be achieved by evaporating solvents to generate surface tension between bundles [262]. To form assemblies continuously, a system was developed at the University of Cambridge where Li et al. [175] collected nanotube aerogels grown from a vapor. These aerogels could be transformed into sheets or yarns by collection with rolls or densification by solvent spray. Yarns produced with this method had ultimate tensile strength between 100 MPa and 1 GPa using a conversion from linear density to tensile stress, and assuming a nanotube density of 2.0 g/cm^3.

Polymer incorporation has been shown to improve the mechanical properties of CNT assemblies by increasing load sharing between nanotubes. Dispersion-based fibers that incorporated polyvinyl alcohol (PVA) to form a composite showed increased toughness [28]. Twisting the composite fibers further improved the UTS 50% over yarns without polymer [204]. Ma et al. [117] developed a process to incorporate epoxy and PVA resins into carbon nanotube yarns. After consolidation by twisting, the tensile strength achieved was approximately 500 MPa without resin and 1.2 GPa for both epoxy and PVA. Despite the strength being the same for the two polymer systems, shifts in Raman

radial breathing modes showed cross-linked polymers transfer more load between

nanotubes [117].   Within a closed resin transfer molding system, Chang et al. [263]

fabricated laminates of CNT sheets by infusion, where viscosity was reduced by the use

of solvents. Their thickest laminate of 6000 sheets could not be infused as flow through

the nanoporous CNT material was insufficient, but laminates of 4000 sheets had

ultimate tensile strength and Young's modulus of 231 MPa and 20.4 GPa, respectively.

Viscosity often hinders the fabrication of CNT composites because of issues with

infusion and voids left after evaporation.

Dicyclopentadiene (DCPD) is a promising candidate for infusion into CNT materials

since it has a low viscosity (~10cPs). It has high toughness when compared to other

thermosetting polymers [264], and low density (~1g/cm^3) [265]. It also has high cross-

link density [266] for improved load transfer.   Dicyclopentadienes' aromatic structure is

comprised of cyclopentadiene and strained norbornene with one shared edge [267] and

it can be polymerized in air using a ruthenium catalyst [268]. One of the pioneering

works forming a nanotube composite based on DCPD resin was done by Jeong and

Kessler [269]. The samples contained up to 0.4 wt% of dispersed and functionalized

CNT powders in DCPD polymer.   Compared to the pristine resin, CNT addition increased

the energy to failure by 925% and failure changed from local crack propagation to

ductile necking. However the peak stress remained approximately 65 MPa as a result of

the low overall concentration of nanotubes.

In this work, we have eliminated the aforementioned issues by using a bottom up approach to the incorporation of dicyclopentadiene and assemblies of carbon nanotubes. We describe the fabrication of high volume fraction, consolidated, nanocomposites by infusion and polymerization of DCPD throughout carbon nanotube yarns. The mechanical properties of the composites were determined by tensile testing. The microstructure of the materials before and after incorporation of the resin was characterized by electron microscopy.

5.2 EXPERIMENTAL METHODS

5.2.1 MATERIALS

Carbon nanotube ribbons and sheets were obtained from Nanocomp Technologies Inc. (Merrimack, NH). The growth parameters are proprietary, but the production process is similar to a method developed at the University of Cambridge [175, 178]. The growth furnace and feedstock formulation were similar for both the sheets and ribbons, and therefore, the CNTs in the two material forms were chemically indistinguishable. The ribbons and sheets differed only in the collection process that formed them into their material format [177]. As a result, they were used interchangeably to analyze structure and chemistry. The ribbons were 1 tex (g/km), the sheet was 15 g/m^2, and the resin used was primarily dicyclopentadiene with a lesser amount of other constituents. For room temperature processing, 24 wt% tricyclopentadiene (CAS# 36806-65-2) was added to the resin. This reduced the melting point below 32.5°C [266]. In addition,

antioxidants were incorporated to prevent the formation of peroxides [267]. The

polymerization reaction was catalyzed by a 2nd generation Grubbs catalyst with

molecular weight 792.87 au [268]. Ninety six (96) micrograms of crystalline catalyst

powder was suspended in 2 grams of mineral oil that was, in turn, used to polymerize

100 grams of DCPD resin.

5.2.2 YARN FABRICATION

To form CNT yarns without resin, ribbons were grasped by the ends in a twisting

fixture. Initially 25 MPa tension was applied to impart strain alignment. Then a number

of turns were introduced until approximately 1 helical revolution per millimeter was

achieved. The tension was then increased to 50 MPa, where untwisted portions

remaining from the previous step were aligned. A final twist was then introduced to

achieve approximately 2 revolutions per millimeter.

Composite yarns were fabricated by placing nanotube ribbons into catalyzed resin,

mixed at 1 part catalyst to 50 parts resin by weight, and soaking for 5 minutes to allow

time for infusion. Then the wet ribbon was removed from the DCPD bath and

application of stretch and twist was done in a manner similar to the CNT yarn described

earlier. While tension was maintained and once the resin formed a gel, the yarn was

placed in an oven at 120°C for 3 hours to form a cured nanocomposite. The yarn

samples were then segmented into individual specimens for mechanical testing, and

mounted to paper frames with a 10 mm gauge length.

5.2.3 CHARACTERIZATION

The mechanical properties were measured in tension using an Instron 5966 universal test system with a displacement resolution better than 0.1 µm. Samples were affixed into custom grips and the paper frames cut just prior to testing. Loading was performed at 5 mm/min with a 50 N load cell. A conversion from linear density [270] was used to calculate tensile stress according to equation (5.1),

$$\sigma_T = A\frac{P_{load}}{\lambda} \times \rho_{cnt} \tag{5.1}$$

where σ_T is the tensile stress (N/m^2), P_{load} is the measured load (N), λ is the linear density $(tex = g/km)$, ρ_{cnt} is the density of nanotubes (2.0 g/cm^3 [175]) and A adjusts units with a value of 10^9 cm^3/km•m^2. With this approach, porosity is ignored, thereby allowing measurement of the stress on the CNT bundles.

The nanocomposite structure was characterized by high resolution scanning electron microscopy. Two systems were utilized: a FEI Nova NanoSEM 230 with 1.0 nm resolution in immersion mode, and a FEI Nova 600 dual beam HRSEM with focused ion beam (FIB) which was used for cross-sectioning. The FIB had 10.0 nm gallium ion beam resolution and 1.1 nm electron beam resolution in immersion mode. For sub-

nanometer characterization, a FEI Titan high-resolution transmission electron microscope was utilized with 300 kV accelerating voltage. Finally, Raman spectroscopy was performed with a Renishaw inVia instrument equipped with a 532 nm laser.

5.3 RESULTS

5.3.1 CNT ASSEMBLIES

In Figure 5.1a, the surface of a CNT sheet is shown to exemplify the randomly oriented structure of CNT assemblies. The material was porous with approximately 100 to 200 nm spacing between the bundles that were themselves 10 to 50 nm in diameter. The sheet in Figure 5.1b was stretched to 30% elongation in the horizontal direction. The picture shows how the CNT network aligned to applied stresses in a manner reminiscent of a stretched fishing net. In these assemblies, non-CNT material may be identified at higher magnification, as shown in Figure 5.2.   In Figure 5.2a, an arrow points to an amorphous carbon agglomerate on the surface of the CNT sheet, located at the junction of several bundles. In figure 5.2b, a high resolution TEM micrograph of an amorphous carbon aggregate shows the presence of residual iron catalyst (black circular spots) within the amorphous structure. At even higher magnification (Figure 5.2c), amorphous carbon can be seen coating the surface of an individual nanotube.

In order to quantify the amount of amorphous carbon in the CNT assemblies, Raman spectroscopy was utilized. The spectrum shown in Figure 5.3 spans 1100 cm^{-1} to 1900 cm^{-1} to encompass the G and D peaks that correspond to graphitic and non-graphitic
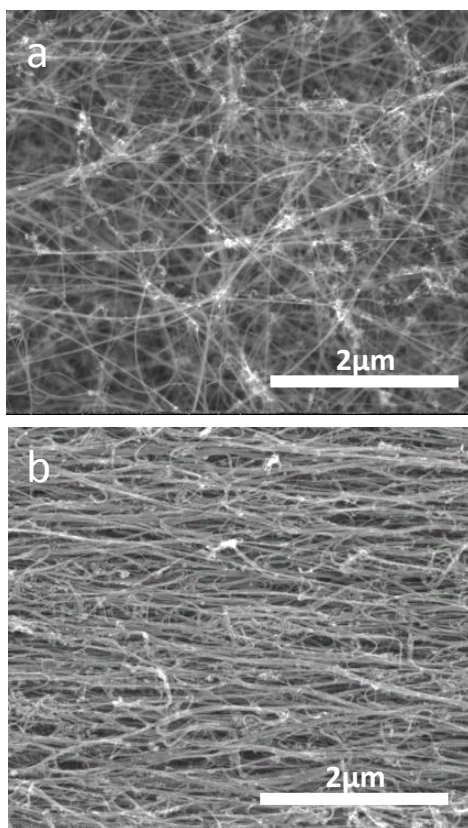
Figure 5.1: Carbon nanotube sheets (a) before and (b) after elongation to 30% strain.
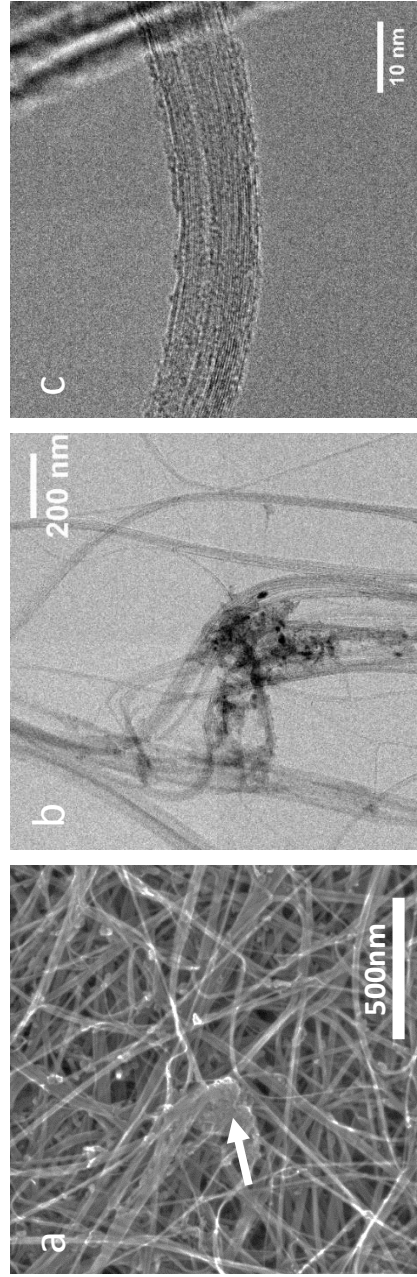
Figure 5.2: (a) Carbon nanotube sheet with amorphous carbon agglomerate highlighted by an arrow, (b) higher resolution image of an agglomerate revealing iron catalyst particles, and (c) single carbon nanotube covered with a rough layer of amorphous carbon.
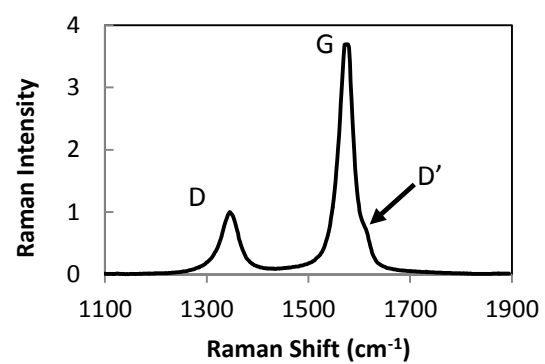
Figure 5.3: Raman spectrum of G, D and D' bands from CNT sheet.

carbon, respectively. Additionally, the spectrum contains the D' peak which accounts for the shoulder on the right edge of the G peak. The ratio of the intensity of the G peak to the intensity of the D peak (I_G/I_D) was 3.69 indicating a reasonably good graphitic structure with minimal defect sites.

Surface wetting by DCPD was studied with resin contact angle on the CNT sheets. This was performed at room temperature and without modification of the material. Before the liquid contacted the sheet, it had a uniform matted finish. When contacted with a 50 µL droplet of DCPD, a low angle drop (~10°) was momentarily formed, then disappeared into the sheet after about 5 seconds. The final contact angle could not be measured as the liquid infused too quickly into the porous structure to capture a static image. Once the DCPD absorbed, the central surface region contacted by the droplet was consolidated, thereby forming a depression in the sheet.

Figure 5.4 shows a HRTEM micrograph of a bundle where the cured resin had uniformly coated the CNT surface. Figure 5.4a shows a kinked carbon nanotube bundle coated in polymer. There are no large particles or steps on the surface, indicating a continuous film. The region boxed in (a) is magnified in Figure 5.4b, and it shows the structure of the carbon nanotubes that have been distorted by the kink into oval and flattened cross-sections. The amorphous film of polymer indicated by the arrow is seen coating the CNT bundle. The coating thickness was between 2 and 5 nm.
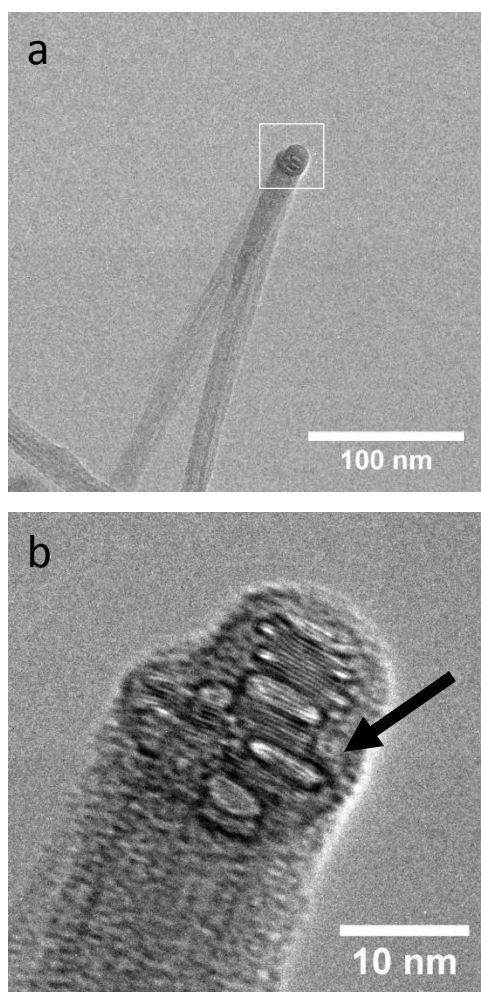
Figure 5.4: Transmission electron micrographs of CNT bundles sheathed by DCPD polymer: (a) kinked bundle, (b) magnification of the kink boxed in (a).

5.3.2 YARNS

Figure 5.5 shows cross-sections of CNT assemblies before and after being twisted into a yarn. In Figure 5.5a, the untwisted structure of a ribbon had a rectangular cross section approximately 20 x 500 μm. Figure 5.5c shows the approximately 40 μm diameter scrolled structure generated by twisting a nanotube ribbon into a cylindrical yarn. The solid arrow indicates a fold where the original ribbon surface had contacted itself. The broken arrow indicates a void with a cross-sectional area of ~800 μm^2. Figure 5.5b shows that the pores within the untwisted CNT ribbon were on the order of 100 nm in diameter. Figure 5.5d, which has the same magnification as Figure 5.5b, shows the porosity within the stretched and twisted CNT yarn. Here, the pores between the nanotube bundles were on the order of 10 nm in diameter.

A cross-section of an infused, twisted and cured composite yarn is shown in Figure 5.6. It had a solid cylindrical structure approximately 45 μm in diameter, Figure 5.6a. A magnification of the region boxed in Figure 5.6a is shown in Figure 5.6b and it reveals the presence of a few isolated, nanometer sized, pores as indicated by the arrow. Nevertheless, the rest of the surface is smooth and indistinct because the spaces between the nanotube bundles have been filled with polymer. In both micrographs, the faint vertical striations are an artifact of the directional ion beam used for milling.

In Figure 5.7, stress - strain response curves are presented for the cured composite yarn, the twisted yarn, the uncured composite yarn, and the DCPD polymer. The
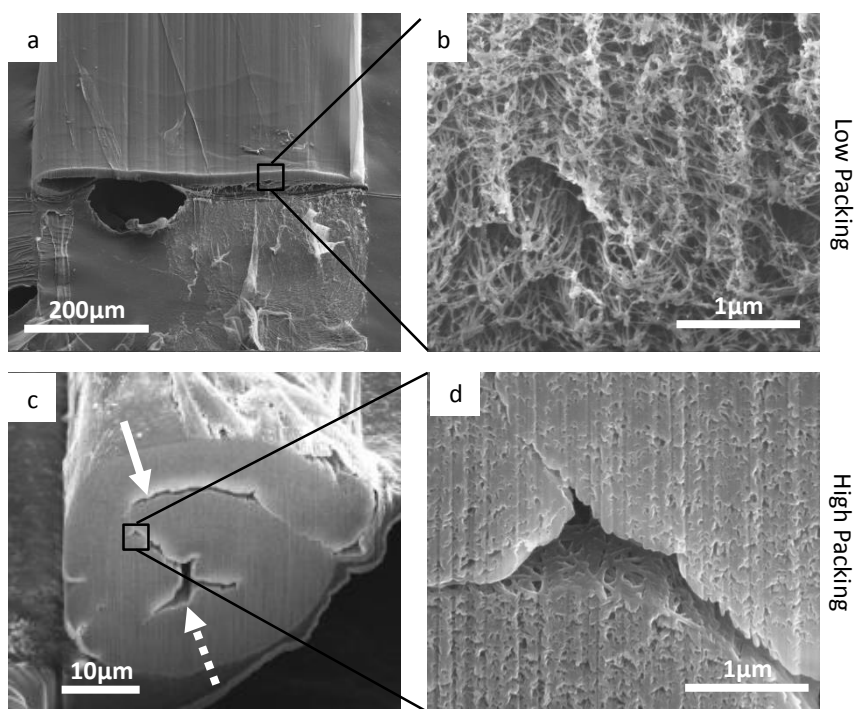
Figure 5.5: Cross section SEM images of carbon nanotube yarn: (a) untwisted ribbon, (b) higher magnification image revealing porosity, (c) twisted ribbon with folded structure (solid arrow) and large voids (broken arrow), (d) and higher magnification image revealing tighter packing and limited porosity.
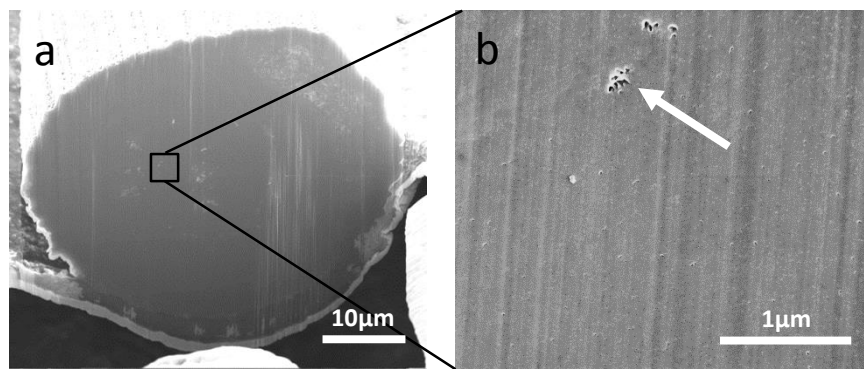
Figure 5.6: Cross section SEM images of composite yarn. (a) Entire solid structure, and (b) Higher magnification showing a few isolated pores, highlighted by an arrow.
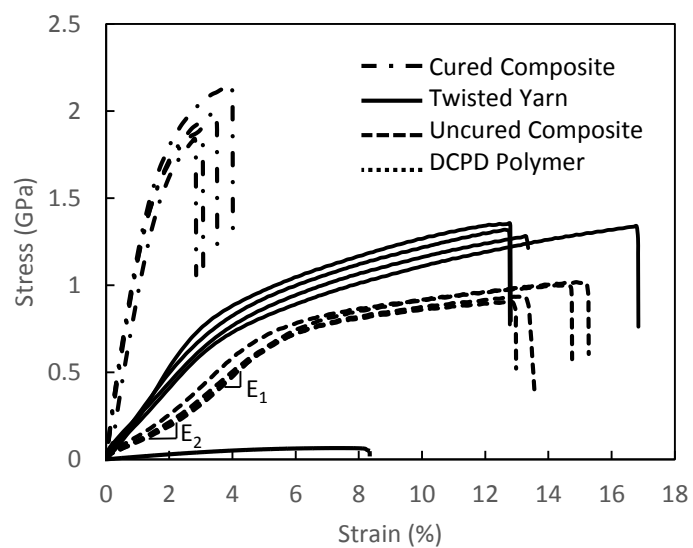
Figure 5.7: Stress-strain response for twisted CNT yarn, cured composite yarn, uncured composite yarn, and DCPD polymer.

mechanical properties for these samples are provided in Table 5.1. The Young's

modulus, ultimate tensile strength and strain at failure for the twisted nanotube yarns

are 23.1±4.0 GPa, 1.32±0.03 GPa and 14.0±1.7%, respectively. The uncured composite

yarns had two linear moduli. The first, E_1, was 59% lower than nanotube yarns at

9.4±0.8 GPa and the second, E_2, was 35% lower at 15.1±0.6 GPa. The tensile strength of

the uncured composite is reduced by 19%, while the strain at failure does not differ

significantly, 14.1±0.9%. The polymerized DCPD had a modulus of 1.49 ± 0.02 GPa,

ultimate tensile strength of 0.06 ± 0.01 GPa, and elongation at failure of 8.4 ± 0.7%.

Introducing DCPD into twisted CNT yarns to form a cured composite increased ultimate

tensile strength 49% over nanotube yarns to 2.0±0.1 GPa. The average Young's modulus

increased fourfold over the twisted yarn to 110±4 GPa. The elongation at failure of the

composite yarn was 3.4 ± 0.4%.

The fracture regions of a twisted and a nanocomposite yarn are shown in Figure 5.8.

The twisted CNT yarn without polymer infusion fractured over a large area. The fracture

spiraled back from the tip, approximately 250 μm, to the point indicated by the arrow in

Figure 5.8a. At higher magnification (Figure 5.8b), the nanotube bundles were seen to

pullout from the yarn, yielding a filamentary structure indicated by the broken arrow.

The tip of a composite yarn (Figure 5.8c) shows a fairly clean fracture without cracks

forming along the fiber axis. At higher magnification (Figure 5.8d) the pullout of CNT

Table 5.1: Mechanical properties for cured composite yarn, twisted CNT yarn, uncured composite yarn, and DCPD polymer.

Sample	Modulus GPa	Ultimate Tensile Strength GPa	Strain %
Cured Composite	110 ± 4	2.0 ± 0.1	3.4 ± 0.44
Twisted Yarn	23.1 ± 4.0	1.32 ± 0.03	14.0 ± 1.7
Uncured Composite	E_1: 9.4 ± 0.8 E_2: 15.1 ± 0.6	0.96 ± 0.05	14.1 ± 0.9
DCPD	1.49 ± 0.02	0.06 ± 0.01	8.4 ± 0.7
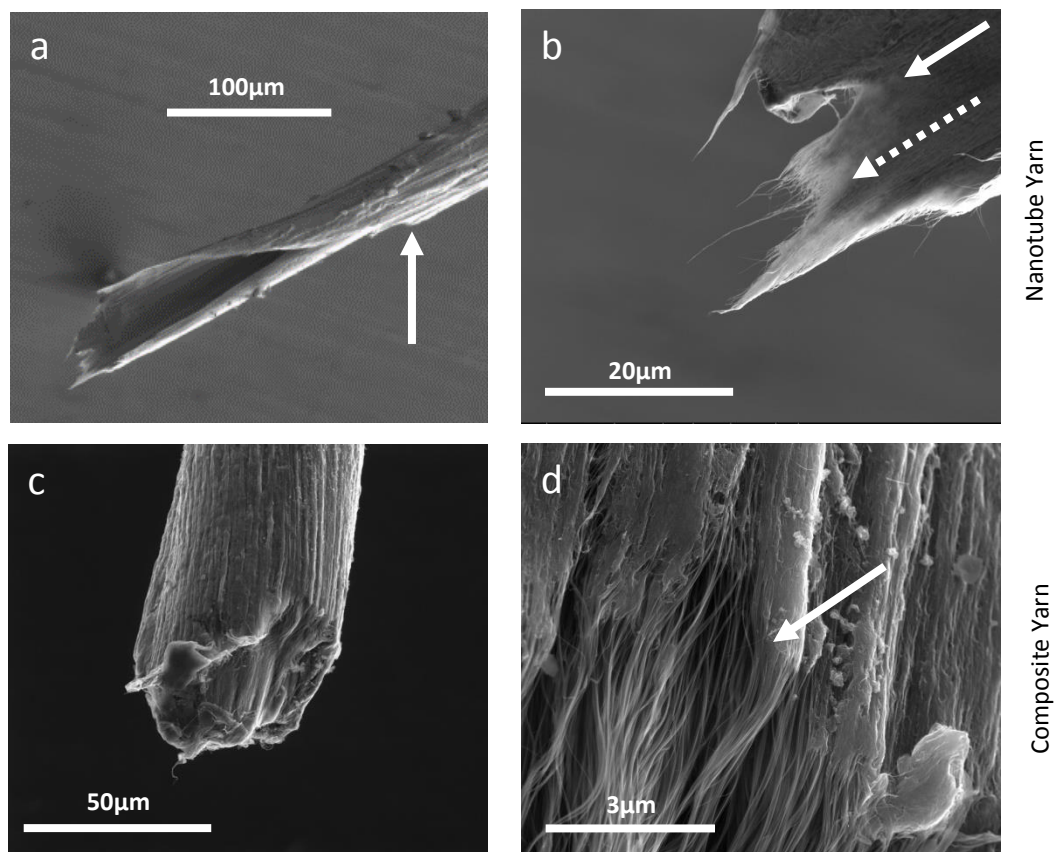
Figure 5.8: Electron micrographs of the tips of carbon nanotube yarns after fracture: (a) twisted yarn with damage extending ~250 μm to the point indicated by the arrow; (b) tip of twisted yarn with filamentary structure indicated by broken arrow, and undisturbed structure by a solid arrow; (c) composite yarn with ~25 μm long damaged region; and (d) tip of composite yarn with arrow indicating end of resin with pulled out CNT bundles.

bundles from the composite yarn can be seen (solid arrow). The length of the pulled-out CNT was approximately 25 μm.

5.4 DISCUSSION

5.4.1 NANOTUBE ASSEMBLIES WITHOUT RESIN

When CNT yarns are twisted, radial compression causes consolidation of the network [184]. This moves adjacent bundles into contact where electrostatic forces keep them aligned together. The consolidation is evident when one compares Figure 5.5b to 5.5d. Where the pore diameter in untwisted ribbon was approximately 100 nm versus only 10 nm in the twisted material. The folds were produced when twisting the ribbons into yarns, but the lack of bonding between the surfaces allowed them to separate. These folds are likely to reduce the mechanical strength of the yarn.

Without the presence of covalent bonds between nanotubes [51], or cross-linking from polymer resins the load sharing in the yarn results from sliding friction between CNT bundles [271]. There are a few features contributing to this frictional force. The first is the presence of amorphous carbon on the CNT surface, which has been shown to increase friction when compared to the surface of pristine nanotubes [124]. Additionally, the amorphous carbon agglomerates that reside at network joints act like knots in the fishing net and resist rearrangement of the CNT bundles. To understand the structural rearrangement during deformation, sheet specimens were tested. These served as model systems, because the structure is simplified when twist is not present.

151

Under stress, the nanotubes move in response to applied force when resin is not present. However, it is the friction that prevents the bundles from slipping apart, and the joints between the CNT bundles cause the network to stretch like a fishing net. As a result of this net structure, the CNT yarns initially exhibited a linear stress – strain response. However the net can only elongate so far and eventually the only means available to accommodate increased strain is for the bundles to slide apart. This resulted in the yield point followed by strain hardening observed in the CNT yarn curves in Figure 5.7.

   The fracture surface of the neat CNT yarn (Figure 5.8a) had a spiraling structure which was a result of the twisting process. When the yarn is twisted the core compresses radially. This causes the fibers at the core to be pushed into intimate contact, yielding better load sharing that increases strength. The surface is not under compression, so it is the weakest point in the yarn and is susceptible to crack formation. A crack will start at the weakest point and travel towards the strongest point in the progression to failure. Referencing Figure 5.8a, failure begins on the outer surface at the point indicated by the arrow. Then, the crack spirals to the core of the yarn due to the helical structure between folds. The lack of bonding across the folds (Figure 5.5c) is likely why fracture does not occur straight across the yarn perpendicular to the load.

5.4.2 Uncured Composite

The incorporation of resin into the CNT network was done to bind the structure together and increase load sharing. The DCPD fully wetted the CNTs as expected due to their similar chemical composition. When infused into the CNT but before polymerization, the DCPD acts as a lubricant during yarn stretching and twisting. As a result, the stress-strain curve of the uncured composite yarn is lower than that of the neat twisted yarn (Figure 5.7). The lubricated CNT fishing net stretches and deforms more freely, and gives rise to an initial modulus that is 59% lower than the twisted yarn. However, just like a fishing net that is being stretched, it can only move so far before the structure aligns and stiffens. This is the reasoning behind the increasing modulus of E_2 in the uncured composite yarn. However, once the net has fully stretched, yield occurs and the bundles slip apart to accommodate further deformation. Lubrication by the DCPD resin reduced the tensile stress by 19% relative to the twisted Yarn. Nevertheless, the elongation at failure was the same for the uncured composite and the twisted yarn.

5.4.3 Cured Composite

The cured composite yarn, as shown in Figure 5.6, had a solid cross section, with polymer filling all the voids between the CNT. This prevented the nanotubes from rearranging in response to stress, and distributed the load throughout the network. Within the composite yarn, the scrolled structure is still present because the same twisting process is used for consolidation. Nevertheless, the fracture is localized, and

did not propagate along the axis for the yarn. After failure, the pulled out nanotubes remain adhered to their neighbors to form enlarged bundles as shown in Figure 5.8.

The tensile tests show that the cured composite yarn better utilized the mechanical properties of the nanotubes. This effect is unique to this material as mechanical properties in carbon fiber reinforced composites are intermediate between those of the fiber and the matrix, according to the rule of mixtures [272]. In the composite yarn, infusing DCPD into the CNT network yielded a modulus of 110 GPa far exceeding that of the polymer (1.5 GPa) and the twisted yarn (23 GPa) independently.

5.4.4 CAPSTAN STRENGTHENING

The restriction of bundle rearrangement by the polymer can account for the increased Young's modulus of the composite yarn, but does not account for the increased tensile strength. Instead this could be explained by mechanical interactions reminiscent of a rope wrapped around a capstan. In a capstan mechanism, a rope is wrapped around a cylinder, and tension tightens the rope against the cylinder inducing a normal force that increases friction [273]. Mathematically this is described by the capstan equation (5.2),

$$T_{Load} = T_{Hold}e^{\mu\varphi}$$
(5.2)

where T_{Load} is the stress applied to the rope, ɸ is the angle swept around the cylinder, μ is the coefficient of friction, and T_{Hold} is the lower holding stress opposite the capstan. In Figure 5.9, a schematic of the capstan mechanism is given. It shows how a CNT bundle could be arranged to transfer load during nanotube pullout in a twisted yarn (Figure 5.9a) and a composite yarn (Figure 5.9b). In this circumstance, the CNT bundles are the rope and the DCPD polymer, if present, is the capstan.

Without cross-linked polymer filling space between bundles, Figure 5.9a, the nanotubes will align with the load and eventually slip relative to each other. The CNT bundles are not curved so ɸ is zero, and the maximum holding stress must equal the frictional shear stress (T_{fric}) between the nanotubes. The twisted yarns exhibited a UTS of 1.32 GPa, so considering this as T_{Load} means T_{hold} could only apply 1.32 GPa to the nanotube to prevent pullout. For the composite, case (b), curvature is fixed in the network by filling all the pores with polymer. In this instance, the tortuous arrangement of CNTs is approximated as two cylinders roughly 10 nm in diameter, with the bundles in contact over 2π radians. The CNT overlap contributing to T_{fric} is assumed to be 25 μm from the observed pullout in Figure 5.8. The length in contact with the 10 nm capstans is insignificant when compared to the length contributing to the holding friction. Setting T_{Hold} equal to the ultimate tensile stress of twisted yarns and using a coefficient of friction equal to 0.08 [274-277], the calculation indicates that T_{Load} is 2.2 GPa. This is in
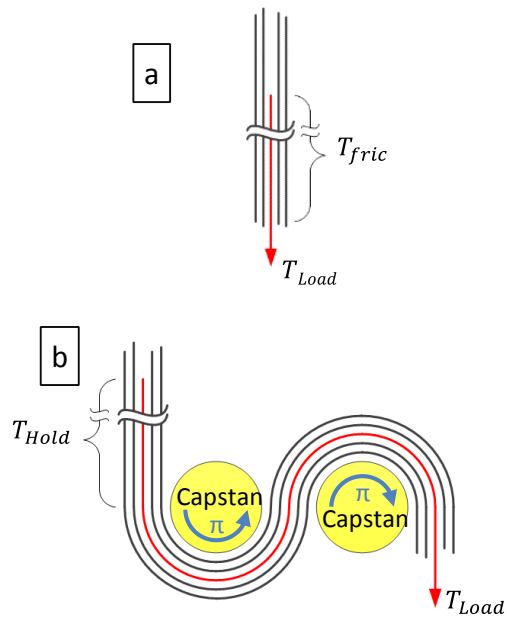
Figure 5.9: Schematic of the capstan mechanism for utilizing nanotube mechanical properties: a) pullout of CNT (arrow) from a bundle aligned by stress and b) pullout of CNT (arrow) when curved 2π radians around DCPD polymer capstan.

reasonable agreement with our experimental results for the composite yarns, in which the UTS equaled 2.0±0.1 GPa.

5.5 CONCLUSION

Dicyclopentadiene resin was found to fully infuse into CNT yarns forming nanocomposites with superior load transfer and improved mechanical properties. This novel resin system, with low viscosity and high CNT surface wetting, also provided lubrication during yarn processing that can be used in the future to improve microstructure and obtain higher strength. This approach also eliminated the need for evaporating solvents that reduce viscosity. Therefore, it has potential to be more cost effective and environmentally friendly when compared to traditional composite resins. In this work the Young's modulus and ultimate tensile strength of the cured composite yarns increased 4x and 1.5x, respectively, relative to CNT yarns that had only undergone mechanical consolidation. The increased tensile strength was accounted for by a capstan mechanism which provided a new explanation for why the CNT yarns do not follow a simple rule of mixtures like traditional composites systems. With these insights into the relationship between microstructure and mechanical properties, methods can be developed for this new composite system to form even stronger materials.

CHAPTER 6: STRENGTH OF DICYCLOPENTADIENE AND CARBON NANOTUBE COMPOSITE SHEETS.

6.1 INTRODUCTION

Individual carbon nanotubes (CNTs) have exceptional physical properties due to their unique chemical structure [10, 278, 279]. Theoretically, an idealized CNT structure made up of single wall nanotubes that are perfectly aligned, hexagonally packed, and tightly cross-linked with sp^3 bonds would have a tensile strength of 60 GPa, a modulus of 700 GPa and an elongation to failure of 15% [51]. However these values remain unrealized in real CNT assemblies. Using a conversion with linear density to measure the stress on nanotubes, the highest measure strength for a large assembly of carbon nanotubes was made by Koziol et al at nearly 9 GPa [176]. However this value was for a 1 mm gauge length and when increasing the gauge to 20mm the average stress was on the order of 1 GPa. The dramatic reduction in stress from 60 GPa to 1 GPa is due to poor load transfer, chaotic arrangement and nonideal packing of carbon nanotubes. Furthermore nanotubes often contain defects that can reduce their inherent strength.

Suekane et al. [124] measured the static "friction" force between carbon nanotubes by sliding apart two nanotubes with varying overlap. The carbon nanotube coated with amorphous carbon had higher sliding friction at approximately 10 nN of static sliding friction for 150 nm of overlap. This was compared to CNTs that were annealed to remove the amorphous carbon. These had a "friction" that was independent of overlap

length and equaled 0.43 nN. Clearly surface roughness and increased contact area between nanotubes plays a significant role in the load transfer between nanotubes.

Vilatela et al. [241] developed a model to predict the strength of carbon nanotube yarns that relies on van der Waals forces for shear stress and load transfer. The model calculated the specific strength of yarns based on an assembly of parallel rigid rods that applied shear stress between neighboring CNT bundles. Using only the outer surface reduced the shear area, and thus reduced overall strength to values that have been experimentally observed. Comparing the model to other experimental results gave a linear correlation between strength and nanotube length. However, there was no correlation between stiffness and CNT length. This was attributed to the variable micro-structure that resulted from comparing fibers produced with different processes.

To study load transfer, Ma et al. made composite CNT yarns with poly vinyl alcohol (PVA) and epoxy resins [117]. These researchers investigated the shift in the Raman G' mode, in situ, while applying strain to the PVA and epoxy composites. They determined that a cross-linked polymer more effectively utilizes CNTs by transferring more load to individual tubes. Highly cross-linked polymers of bismaleimide resin were used to achieve the highest measured strength for a CNT composite at 2.1 GPa [216]. With epoxide functionalized nanotubes this same group reached 3.1 GPa [217]. Wang et al. [212] used CNTs grown as a vertically aligned array to produce a CNT/BMI composite that yielded 3.8 GPa tensile strength.

To study load transfer without cross-linking, Qian et al. [151] modeled the interaction between nanotubes when twisting a rope of seven hexagonally packed nanotubes. The increased radial forces between nanotubes, increased the transferred load such that the binding energy increased from 0.05 eV/Å to 1.7 eV/Å. Gou et al. [244] computed, the binding energy between epoxy (Epon 828 with Epicure W) and bundles of nanotubes. The polymer did not penetrate the bundles of nanotubes so CNT to CNT and CNT to epoxy interfaces existed. By calculating the energy during pull out, it was determined that the energy between CNTs was stronger than the energy between CNT and polymer. This indicated that an attempt to pull a single nanotube from the structure would result in the removal of the entire bundle. Therefore, the interface between the CNTs and the polymer did not effectively transfer load to the CNTs. Mu et al. [280] found that the molecular weight of the polymer had an effect on the load transfer. If the polymer had a radius of gyration greater than the diameter of the nanotube such that it could wrap around the nanotube, the load transfer was improved and modulus increased. However, long chain polymers are difficult to infuse into a CNT network. Monomers that can be infused as a result of low viscosity and then polymerized in place provide a superior method of forming composites with high concentrations of carbon nanotubes.

Herein, we investigate the load transfer in a series of CNT composite sheets with and without infused dicyclopentadiene polymer and with varying levels of alignment. Raman spectroscopy, dynamic mechanical analysis, gas chromatography/mass

spectroscopy and tensile strength testing in tension were used to characterize the

materials. The microstructure and fracture surfaces were characterized with scanning

electron microscopy, and alignment was quantified by wide angle X-ray scattering.

Finally we use a capstan mechanism to explain the load transfer in the composites and

suggest a level of kinking within the aligned CNT networks.

6.2 EXPERIMENTAL PROCEDURE

6.2.1 MATERIALS

The carbon nanotube sheets were supplied by Nanocomp Technologies Inc.

(Merrimack NH). These sheets were formed by growing nanotubes with a "floating

catalyst" chemical vapor deposition process. They were collected on a drum rotated at

15 m/min to accumulate an areal density of 15 grams per square meter. This rotation

speed drew the material from the furnace to impart alignment.

The dicyclopentadiene (DCPD) used in this work was supplied by Sigma Aldrich (CAS #

77-73-6) with a purity greater than or equal to 96%. The structure of dicyclopentadiene,

shown in Figure 6.1a, is a dimer of cyclopentadiene (CPD) that is formed through a Diels-

Alder reaction. This dimer of cyclopentadiene has a melting point of 32.5 °C and a

boiling point of 170 °C [266]. When melted, DCPD has a low viscosity on the order of 10

cPs [265]. Tricyclopentadiene (TCPD, Figure 6.1b), was added to the resin by a Diels-

Alder reaction of CPD and DCPD in a heated pressure vessel [267, 281, 282]. This

processing generated molar concentrations of 8% trimer and 92% dimer (Figure 6.2) and
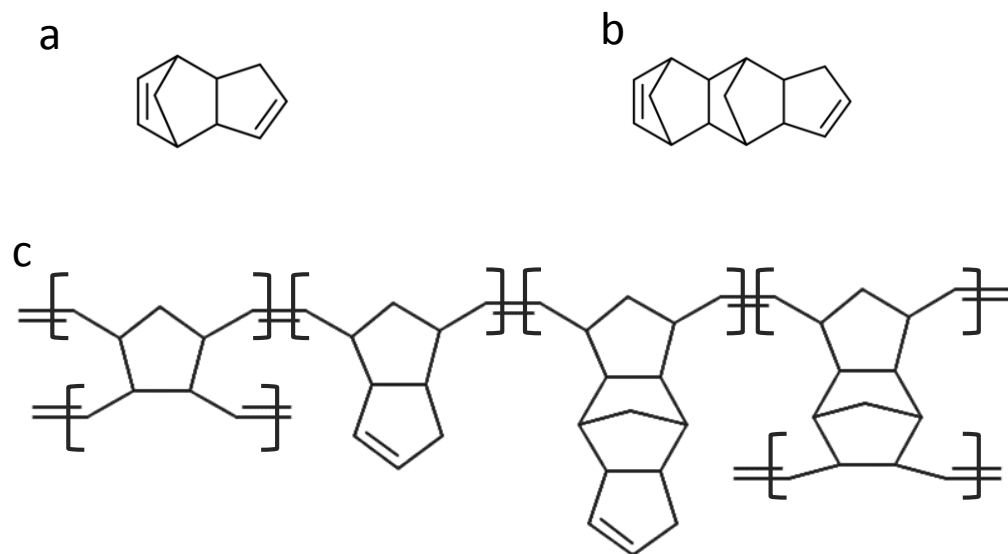
Figure 6.1: Structure of DCPD resin: a) dicyclopentadiene dimer. b) Tricyclopentadiene trimer. c) Polymerized DCPD resin structure.
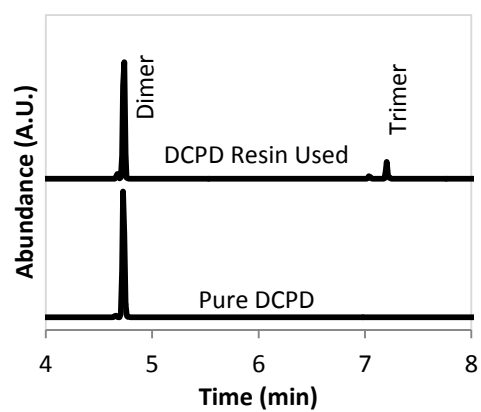
Figure 6.2: Gas chromatograms of pure DCPD and resin used in composite.

reduced the melting point to 0 °C. The four types of species found in polymerized DCPD are depicted in Figure 6.2c. A second generation ruthenium based catalyst (CAS# 246047-72-3) with an atomic weight of 848.97 A.U. was used for polymerization. The crystalline catalyst was added to toluene to produce a solution where 10 mg of catalyst was dissolved into 1 g of toluene. This solution was used at a ratio of 0.1 mg of catalyst solution to 10 grams of resin.

6.2.2 SAMPLE FABRICATION

Specimen were produced by stretching in the same direction as the sheet was drawn during growth. As received sheet was considered unstretched. Five percent (5%) and fifteen percent (15%) sheets were produced by stretching the material to 5% and 15% strain, respectively. This stretching was performed on a specimen with a 150 mm gauge length and a 25 mm width at 5 mm/min. To form a composite, sheets were immersed in DCPD resin that was then degassed with vacuum for 60 seconds. The wet sheet was then placed in a flat mold and compressed at 14 MPa in a hot press, while held under vacuum with a composite molding bag. The heating cycle was 1 hour at 60 °C, 3 hours at 140 °C, and then cooling down to 25 °C before removing pressure. Two layers of Teflon tape were used as a release ply and filter paper was used as bleeder ply. The neat and composite specimen were cut into smaller samples for mechanical testing. The neat samples without resin had widths of 4-5 mm while the composite samples had

widths of 3-4 mm. Both were cut to a 30 mm length and mounted to paper test frames with a 20 mm gauge length.

6.2.3 CHARACTERIZATION

Raman spectroscopy was performed with a Renishaw InVia Raman spectrometer. The system utilized a 785-nm laser and a Leica microscope with a 50x objective to form a laser spot size of 1 µm. Spectra were recorded in extended mode between 1000 and 3000 cm^{-1}. To avoid thermal damage to the nanotubes, the laser power on the sample was maintained at 0.01 mW.

Thermogravimetric analysis (TGA) was performed with a TA Instruments Q50 (New Castle, DE) at a ramp rate of 10 °C/min from 20 to 800 °C. The samples were placed in platinum pans and 100 mL/min of gas flowed over the samples with a composition of 10:90 nitrogen and air. The mass loss data along with its derivative were plotted versus temperature.

Dynamic mechanical analysis was performed with a TA Instruments Q800 (New Castle, DE). Samples were tested in a single cantilever configuration under flowing air and deformed sinusoidally at 1 hertz. The temperature was isothermal for 2 minutes at -140 °C then ramped to 150 °C at 5 °C/min. The tan δ data was plotted versus temperature.

An Instron 5966 universal test system was used to evaluate the mechanical

properties of the CNT sheets. Loads were applied at 5 mm/min with a 500 newton load

cell and stresses were calculated with equation (6.1),

$$\sigma_T = A \frac{P_{load}}{\lambda} \times \rho_{cnt}$$

(6.1)

where σ_T is the tensile stress (N/m^2), P_{load} is the measured load (N), λ is the linear

density $(tex = g/km)$, ρ_{cnt} is the density of nanotubes (2.0 g/cm³ (Li, Kinloch, &

Windle, 2004)) and A adjusts units with a value of 10^9 cm³/km•m². The linear density

was determined by equation (6.2)

$$\lambda = Bwt\rho_{Sheet}$$

(6.2)

Where w is the specimen width (mm), t is the specimen thickness (µm), ρ_{Sheet} is the

measured density of the CNT sheet, and B adjust units with a value of 1

cm³/mm•km•µm.   For the composite specimens, the sample density was normalized

for the CNT weight fraction determined by TGA. This was done to measure the stress on

the CNT network as it is the primary load carrying component. The tensile strength was

defined as the maximum stress achieved in each test. The modulus of the CNT structure

was calculated based on a linear fit to the stress versus strain data. For the neat CNT

sheet, this was determined in the linear portion between 10% strain and the strain at

maximum stress. For composites, the elastic region in the first 0.5% of elongation was used to calculate the modulus with a linear fit.

Electron micrographs were obtained with an FEI Nova 600, dual beam, high resolution scanning electron microscope. The system was operated in field immersion mode at 10 kV accelerating voltage, 0.54 nA beam current and a working distance of 5 mm.

Wide angle X-ray scattering was performed on a Rigaku R-Axis SPIDER that had a cylindrical area detector with a radius of 127.4 mm and 100 μm x 100 μm pixel size. The system utilized a 2.0 kW copper source with a graphite monochromator and a 0.3 mm double pinhole collimator. It was operated at 50 kV and 40 μA. These images were then analyzed with AreaMAX 2.0 and the data was processed as described in Chapter 4.

6.3 RESULTS

6.3.1 STRUCTURE OF COMPOSITE

Figure 6.3 shows the Raman spectrum of the CNT sheet from 1200 to 1800 cm^{-1} to encompass the graphitic G, nongraphitic D, and D' peaks [71]. The G peak was located at 1580 cm^{-1} and the D peak was located at 1309 cm^{-1}. The ratio of G intensity to D intensity, I_G/I_D, had a value of 7.9. The shoulder on the right side of the G peak is the D' peak. Cancado et al. [283] developed an equation to quantify the average distance between defects in graphene based on the I_D/I_G ratio and laser wavelength [283]. With
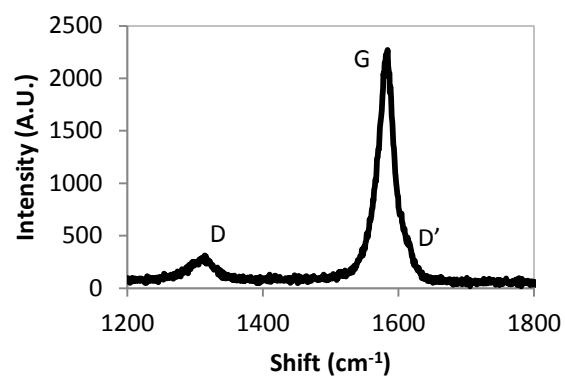
Figure 6.3: Raman spectrum of D, G and D' bands from CNT sheet.

this calculation the average distance between defects in the CNTs investigated herein was 73 nm.

Figure 6.4 shows the surface of the composite made from sheet without stretching. In this case the resolution of the nanotubes is reduced because the structure is filled with resin. The nearly random arrangement of nanotubes was unchanged from that of the neat CNT network. The arrow points to a small bundle of CNTs with dark regions of polymer on either side. There were also pores observed on the surface that are highlighted with circles. The 0% composite sheets had a density of 0.81 g/cm^3 while the composites made with 5% and 15% stretched sheet had densities of 0.85 g/cm^3 and 1.01 g/cm^3 respectively, Table 6.2.

Thermogravimetric analysis of the CNT sheet, DCPD polymer and composite are shown in Figure 6.5. The horizontal axis is the temperature from 0 °C to 800 °C. The left vertical axis is the mass loss as a percentage of the original sample mass. The right vertical axis is the derivative of the mass loss with units of %/°C. In Figure 6.5a, the TGA data is given for the CNT sheet. In this case there were three clear peaks located at 575, 642 and 690 °C, corresponding to three grades of nanotubes. Additionally, there was a small and broad peak centered at 320 °C that resulted in 4% mass loss up to 450 °C. This was attributed to amorphous carbon [252]. After the test, 12.9% mass remained. This mass was Fe_2O_3 which indicated 9.7 wt% residual catalyst. In Figure 6.5b, the TGA data is given for the polymerized DCPD. Up to 183 °C the sample gained 1% mass due to

169
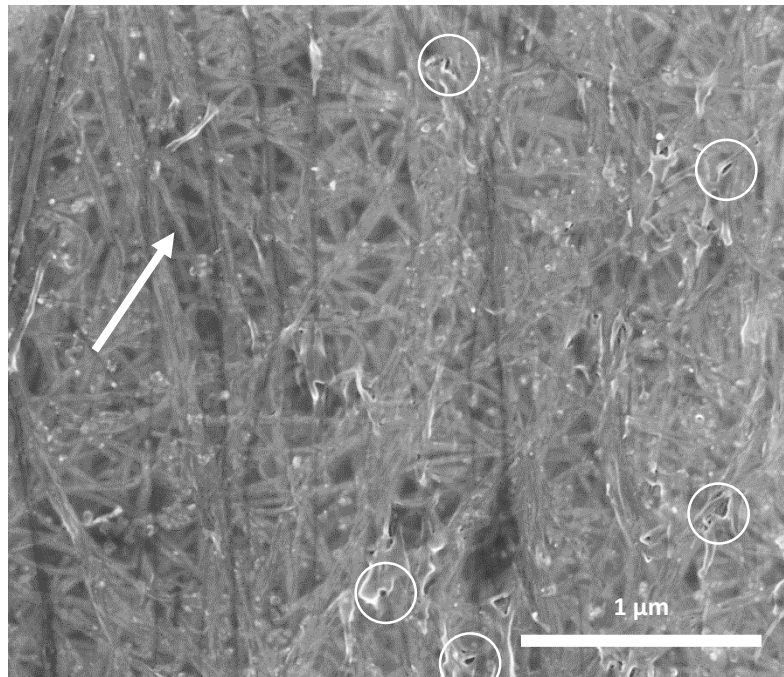
Figure 6.4: Surface of unstretched composite. Arrow points to a bundle of CNTs below the polymer surface and circles highlight voids.
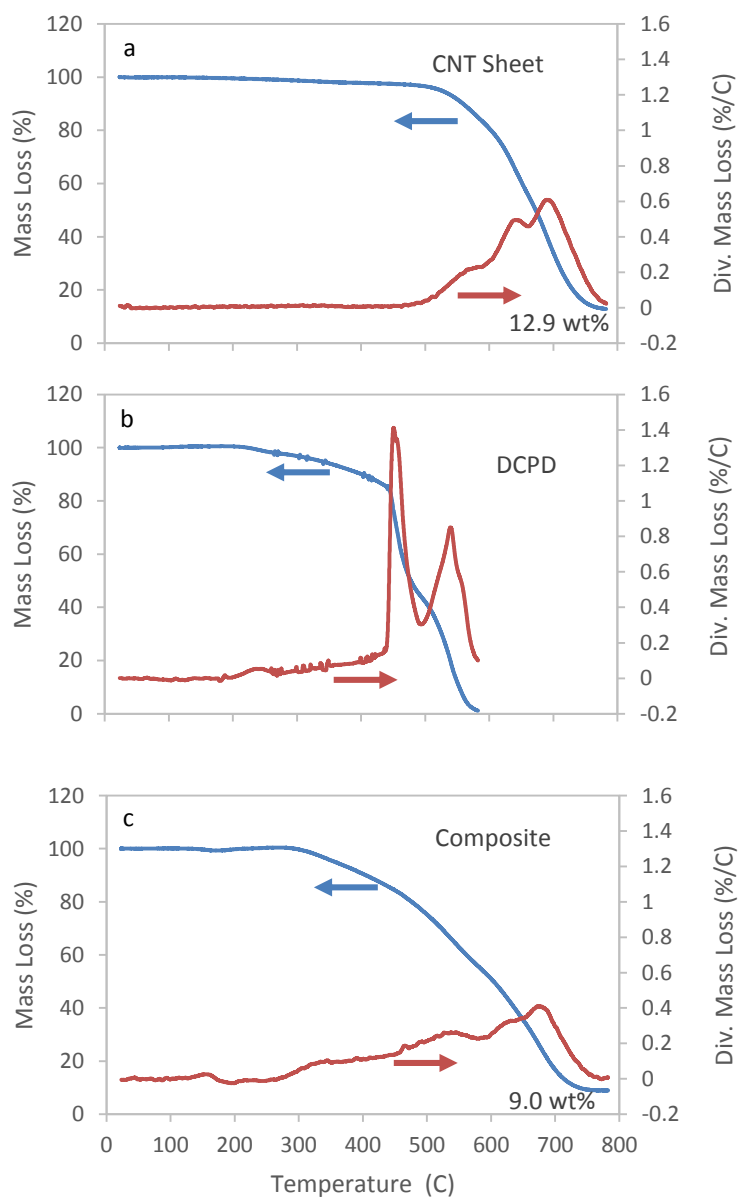
Figure 6.5: Thermal gravimetric analysis showing the mass loss and the derivative of the mass loss for a) neat CNT sheet b) DCPD polymer and c) unstretched composite.

oxidation. The mass steadily dropped between 200 °C and 445 °C. The material then

rapidly degraded at two dominant temperatures.   The first peak in the derivative curve

was located at 451°C, and the second was located at 540 °C. The minimum between

these two peaks was located at 493 °C. In Figure 6.5c, the TGA data is given for the

composite sample indicating the combined results of the CNT and DCPD polymer. In this

sample, oxidation caused the mass to increase 0.5%, peaking at 268°C, which was 85 °C

higher than the polymer alone. Additionally, the mass loss started at 275 °C, indicating a

75 °C increase in thermal decomposition temperature. Above this temperature, the

mass dropped steadily. Evidently the CNT decomposition occurred at a lower

temperature in the composite than in the neat CNT sheet. The peak in the derivative

mass loss was located at 678°C, which is 12 °C lower than the CNT alone. At the end of

this test there was 9.0% residual mass indicating a 70% mass fraction of carbon

nanotubes. The composites made with CNT sheet stretched to 5% and 15% had 53.5%

and 54.0% mass fractions, respectively.

   Tan δ results from the dynamic mechanical analysis of the CNT sheet, DCPD polymer,

and their composite are presented in Figure 6.6. The peak in the tan δ curve gives the

glass transition temperature of a polymer. This is where the polymer chains begin to

move within the material and the structure becomes rubbery. This is related to the

cross-link density and steric hindrance of the polymer. The CNT sheet did not show a

distinct peak corresponding to a glass transition temperature of the CNTs or the

172
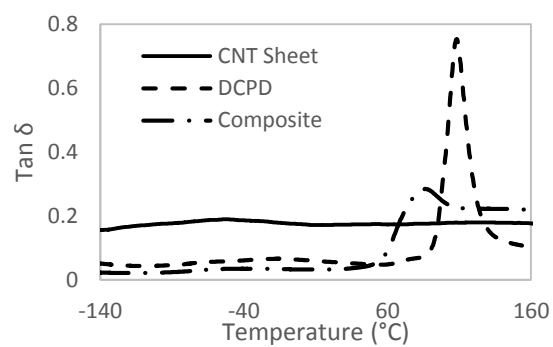
Figure 6.6: Tan δ curves from dynamic mechanical analysis of unstretched CNT sheet, DCPD polymer and composite.

amorphous carbon that coats its surface. However, there was a small, broad peak

located at -53 °C. The DCPD polymer showed a peak in the tan δ indicating a Tg of 108

°C. When combining the DCPD and CNT to form a composite, the peak in the loss

modulus decreased by 22 °C to 86 °C.

6.3.2 ALIGNMENT

The alignment of carbon nanotubes in the stretched sheet is summarized in Table

6.1. For the unstreched sheet, a maximum alignment in a single direction was 3.6%

where a random distribution would have given 2.8 %. Only 14% of the nanotubes were

within ±10° of the drawing direction. The unstretched sheets had a Hermans

orientation factor of 0.071 with respect to the drawing direction used during growth.

An HOF of 1 indicates perfect alignment and a value of 0 indicates random alignment

(Chapter 4). The density of the unstretched samples was 0.21 ± 0.01 g/cm^3. After 5%

elongation, the alignment improved slightly, where the peak orientation reached 3.8%,

and 15% of the nanotubes were within ±10° of the stretching direction. This was little

change to alignment which is confirmed by the HOF value of 0.077. The density of the

5% stretched sample was 0.21 ± 0.01 g/cm^3 indicating no change from the unstretched

sheet. In the 15% stretched sheet the peak alignment was 7.1%, and 27% of the

nanotubes were oriented within ±10° of the stretching direction. The HOF was 0.176

and the density of this sample reduced 10% to 0.19 g/cm^3.

Table 6.1: Alignment in CNT sheets.

Stretch	Peak	±10°	HOF
	%	%	-
0%	3.6	14	0.071
5%	3.8	15	0.077
15%	7.1	27	0.176

6.3.3 Mechanical Properties

Figure 6.7a shows stress versus strain curves for the neat CNT sheet. These results are summarized in Table 6.2. The sheet, had a tensile strength of 540 ± 35 MPa, a modulus of 2.5 ± 0.2 GPa and 27 ± 2% elongation to failure. In the 150 x 25 mm samples, the strain at failure would not exceed 22% even with strain rates of 6.7 x 10^{-4} s^{-1}. The initial slope was low and after approximately 5% elongation the network stiffened and the slope of the curve increased. The curve for the samples prestretched to 5% strain showed a more linear response between stress and strain. The tensile strength was 515 ± 25 MPa, the modulus was 2.6 ± 0.1 GPa and elongation at failure was 21 ± 1%. The samples prestretched to 15% strain before testing reached a tensile strength of 600 ± 25 MPa, a modulus of 6.7 ± 1.0 GPa and an elongation to failure of 12 ± 1%. It should be noted that when stretching the 150 x 25 mm sheet to 5% and 15% elongation the load was not removed until returning to 4% and 13% strain, respectively.

Figure 6.7b shows the stress versus strain curves for the composite samples made from as received, 5% stretched and 15% stretched sheet. These results are also summarized in Table 6.2. All three curves show an initially high slope followed by yielding and deformation with a gradual slope up to failure. The unstretched samples had a tensile strength of 1110±80 MPa, modulus of 60.0 ± 4.0 GPa, and a strain at failure of 11±2%. The composite samples made from sheet drawn to 5% had a tensile strength of 1380±155 MPa, a modulus of 73.0±5.0 GPa, and elongation at failure of 15±2%. This
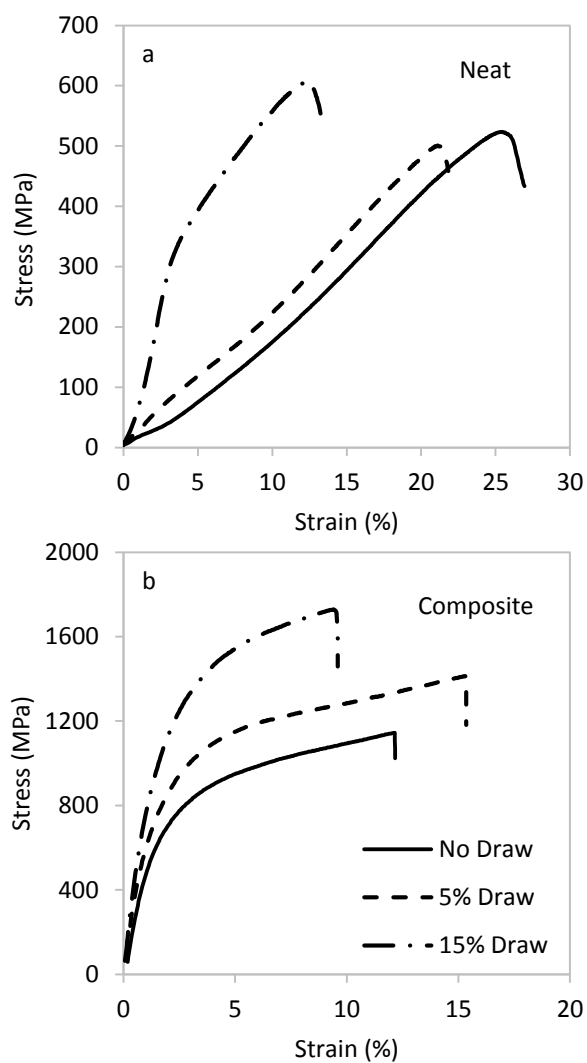
Figure 6.7: Stress versus strain curves for a) neat CNT sheet and b) composite sheets.

Table 6.2: Material properties and effect of stretch and inclusion of polymer on the stress carried by carbon nanotubes.

Draw	Sample	Stress	Modulus	Strain at Failure	Density
		MPa	GPa	%	g/cm^3
0%	Neat	540± 35	2.5 ± 0.2	27 ± 2	0.21 ± 0.01
	Composite	1110 ± 80	60.0 ± 4.0	11 ± 2	0.81 ± 0.08
5%	Neat	515 ± 25	2.6 ± 0.1	21 ± 1	0.21 ± 0.01
	Composite	1380 ± 155	73.0 ± 5.0	15 ± 2	0.85 ± 0.12
15%	Neat	598 ± 26	6.7 ± 1.0	12 ± 1	0.19 ± 0.01
	Composite	1760 ± 225	102 ± 15	8 ± 2	1.01 ± 0.05

28% increase in elongation over the unstretched composite is statistically significant. The composite samples made from sheet drawn to 15% elongation had the highest strength and modulus at 1760±225 MPa and 102±15 GPa, respectively. This came at the expense of elongation which was 8±2%.

6.3.4 FAILURE

Figure 6.8 shows the surface of a composite made from unstreched CNT sheet that has been stretched to failure. The location is away from the fracture tip to demonstrate the surface morphology prior to failure. There is a distinct line across the image which is indicated by an arrow. This was a fold that was present in the material as received. These folds have been described previously (Chapter 4). This region is magnified in the inset micrograph, highlighting CNT pullout. In the low magnification micrograph there were also dark regions which are circled. These are locations of high resin content. The surface of the sheet also contained regions of lower resin concentration and one of these regions is indicated with a broken arrow. The surface of the composites made with 5% and 15% stretched sheet had similar structures but the creases were not present.

Figure 6.9 shows the fracture surface of the composite made from 15% pre-stretched CNT sheet. It was clear that the resin fully infiltrated into the porous CNT network and after failure the CNT pullout was approximately 40 μm. The composite failed between layers of CNTs producing a stepped fracture surface. Arrows indicate three of the layers
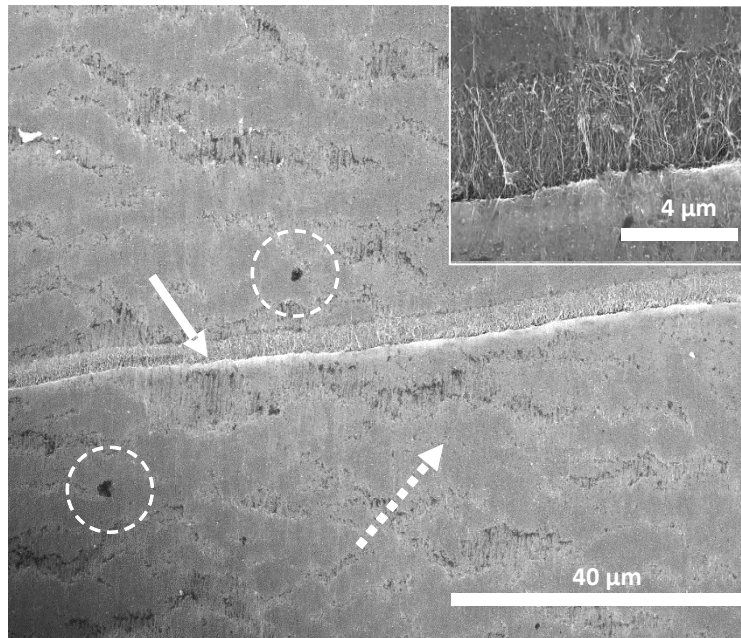
Figure 6.8: Surface of composite after failure and away from fracture tip of a) undrawn. Dashed arrow indicates regions of high CNT concentration. Solid arrow arrows indicates a deformed crease. Circles highlight DCPD polymer. Inset micrograph magnifies crease region.
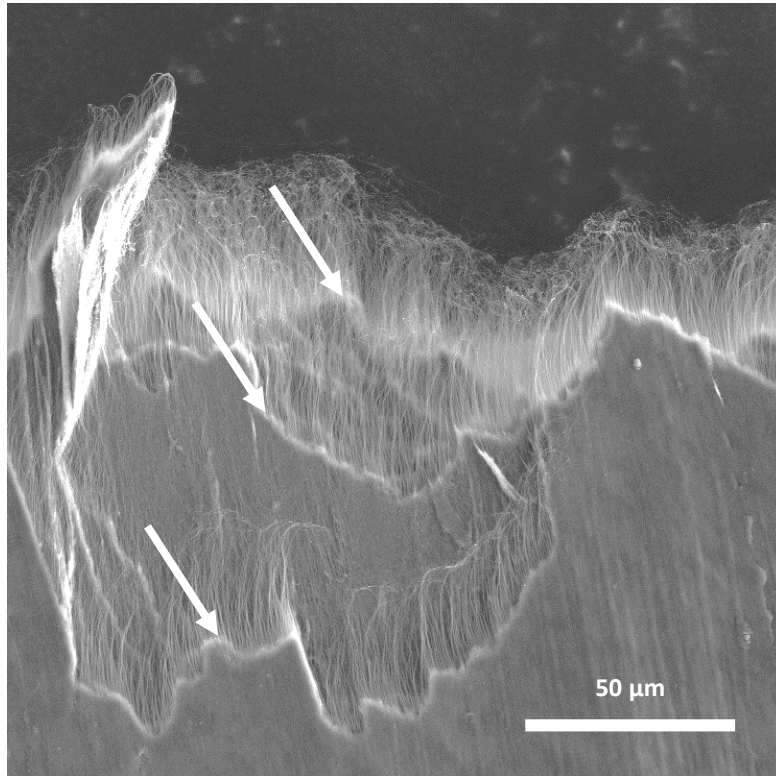
Figure 6.9: Fracture tip of 15% drawn composite. Arrow indicate individual layers of pulled out nanotubes.

where the polymer stops and CNTs protrude. The composites made from un-stretched

and 5% stretched CNT sheet also exhibited similar fracture surfaces. This type of

stepped fracture surface has also been observed in other multilayer composite sheets

[212, 216].

6.4 DISCUSSION

6.4.1 CARBON NANOTUBE COMPOSITE

The density of the composites made with unstretched and 5%pre-stretched sheet

was 0.81 and 0.85 g/cm^3, respectively. This infers there is porosity in the structure since

the solid polymer is ~1 g/cm^3, and the density of the nanotubes is 2.0 g/cm^3 [175].

However, focused ion beam cross-sections of the composite did not show large porosity,

and instead indicated a solid and uniform structure. One explanation of the reduced

density is that the resin did not penetrate within bundles of nanotubes as was observed

in the model by Gao et al. [244]. This level of pore size might not have been observed in

focused ion beam cross-sections due to material redeposition causing the pores to fill.

The tan δ from the DMA analysis showed a small broad peak for the CNT sheet

located at -53 °C that could correspond to the loss associated with the surface coating of

amorphous carbon on the CNTs which amounted to 4 wt% according to TGA data. The

DCPD polymer showed a distinct peak at 108 °C, but when incorporating the DCPD into

the CNT assembly to form a composite, the T_g dropped 22 °C. This is unlikely a result of

different steric hindrance of the polymer side groups. Instead, it must infer that the

cross-link density is reduced in the composite. The CNTs probably hindered the

diffusion of the catalyst through the network and decreased the extent of cross-linking

during polymerization. The molar concentration of the catalyst to DCPD was 65,000 : 1.

By assuming the molecular volume of the DCPD dimer is a 0.5 nm cube, then there

would be one catalyst molecule for a 20 nm cube of resin, which is on the order of the

pore size in CNT agglomerates [284-287].

6.4.2 LOAD TRANSFER

The load transfer in a carbon nanotube network, without resin, is reliant on the

friction between nanotubes preventing the bundles from slipping apart. The CNTs are

held into bundles by van der Waals forces with minimal adhesion between the bundles.

When resin is added to the CNT network, a dramatic increase in load transfer to the

nanotubes occurs. We have proposed that this is due to the capstan effect (Chapter 5).

Here, the curvature of nanotube bundles causes the CNTs to pull out through a tortuous

path. This path introduces transverse forces and increases the friction that must be

overcome for CNT pullout. By comparing the stress applied to the CNT network without

resin and the stress applied to the CNTs in the composite, we can observe the increase

in load transfer results from capstans. This is done with the capstan equation:

$$T_{Load} = T_{Hold}e^{\mu\varphi}$$

(6.3)

where T_{Load} is the load applied to the nanotube that is being pulled out, T_{Hold} is the holding stress that comes from the friction between nanotubes, μ is the coefficient of friction between nanotubes (0.08 [274-277]) and ϕ is the angle in radians that the CNT bundle is in contact with the capstan. Solving equation 3 for ϕ gives;

$$\varphi = \; ln\left(\frac{T_{Load}}{T_{Fric}}\right) \times \frac{1}{\mu}$$

(6.4)

where T_{Fric} is the stress at failure in the CNT network without resin and T_{Load} is the stress in the composite at failure. In the neat CNT sheets, the average stress on the CNTs in the unstretched, 5% stretched, and 15% stretched were 540, 515, and 600 MPa, respectively. After forming a composite, the stresses increased to 1110, 1380 and 1760 MPa, respectively. Inputting these values into equation (6.4) gives ϕ values for the unstretched, 5% stretched and 15% stretched CNT networks of 9.0, 12.4, and 13.5 radians, respectively. These values are summarized in Table 6.3. This means that as the CNT network is stretched to produce alignment, the capstan contact angle from the curved CNT structure is also increasing. This can be accounted for by the formation of kinks as the network deforms.

6.5 CONCLUSION

Composite sheets have been prepared from dicyclopentadiene and carbon nanotube sheets subject to different degrees of alignment. The composite that was formed was

Table 6.3: The effect stretching has on the kink curvature in composite sheets.

Stretch	T_{Load} MPa	T_{Fric} MPa	Φ Radians
0%	1107	538	9.0
5%	1383	515	12.4
15%	1764	598	13.5

fully infused and had densities between 0.8 and 1.0 g/cm^3 indicating porosity. This was

attributed to voids inside nanotube bundles. It was shown that stretching the CNT

networks improved alignment but also increased nanotube kinking. This kinking was

estimated based on the level of increased load transfer to the CNT network within the

composites.

CHAPTER 7: CONCLUSIONS AND FUTURE WORK

7.1 CONCLUSIONS

The aim of this thesis is to demonstrate a new DCPD and CNT material system for

high strength composites and bring understanding to the relationship between the

microstructure of carbon nanotube assemblies and their mechanical properties. Efforts

have to be made to control the sample preparation and improve the structure with

alignment and consolidation. From the various structures, conclusions are drawn about

the load transfer mechanisms operating between the CNTs and the polymer.

Determining the alignment in CNT sheets provided insight into how the network

responds to deformation by stretching. The alignment observed in the sheets was not

dramatic reaching a maximum HOF of 0.3 even when stretching all the way to failure.

During growth the CNT sheets were drawn from the furnace as rapidly as possible

without breaking the aerogel. This was done to impart the most alignment possible to

the CNT assemblies before the structure densified. This method was only capable of

imparting a small amount of alignment. However, the alignment during growth was enough to make the mechanical properties vary widely. The tensile strength was approximately 3x higher in the growth direction than it was perpendicular. The alignment was less dependent on direction, and the material deformed freely until the structure aligned and failure occurred by slip within bundles. The alignment occurred in phases where stretching in the transverse direction resulted in large amounts of deformation without a corresponding increases in the alignment.

From chapter 5, the incorporation of polymerized DCPD provided insight into how load is transferred through CNT bundles. As was predicted, the low viscosity of DCPD improved infusion into the porous CNT network, and it had high surface affinity which aided infusion by surface wetting. Additionally, the unpolymerized DCPD acted as a lubricant between CNTs. This reduced the stress required to deform the CNT yarns but it did not change the elongation to failure. The failure remained reliant on CNT bundle sliding apart which is dependent on strain and not sliding force. The polymerization of DCPD dramatically increased the tensile stress that could be supported by the CNT network. This was far in excess of any tensile contribution of the DCPD as the composite stresses reached 2 GPa while the polymer alone could only support 60 MPa. To reflect this increase in mechanical properties a capstan mechanism was proposed as a load transfer mechanism when CNT bundles are in contact with a polymer. This

mechanism reflects the tortuous structure of the CNT assemblies, and it does not rely on shear stress between the polymer and nanotubes.

In chapter 6, the strengthening mechanism in composite yarns was simplified and expanded upon by eliminating twist in the composite. Removing twist meant the sheets did not have an additional mechanism for load transfer as a helical structure would compress its core when put under tension. Also, by measuring the alignment of the CNT network in response to stretching it was possible to understand the microstructure of the composite. It was observed that the formation of the composite increased the thermal stability of the DCPD polymer whereby it increased the decomposition temperature 75 °C. However, the CNTs interfered with cross-linking and caused the glass transition temperature to drop by 22 °C. From mechanical testing, it was clear that as the network became more aligned both the strength and the modulus increased. The modulus increase can be attributed to the higher proportion of CNTs oriented along the tensile direction. Like in the yarns, the strength increase was attributed to a capstan effect. However, in this work, the increases in stress was used to estimate the extent of the tortuous configuration of the CNTs. It suggested that as the CNT network aligns it is also becomes more tortuous, as tubes oriented transversely are kinked during alignment. Even a small localized kink can have a large effect on the long range tensile properties of the CNT bundles.

This thesis establishes DCPD and CNT assemblies as an effective material system for high strength composites. Furthermore, it will help future researchers understand that high volume fraction CNT composites are not simple parallel rods in a matrix or even a helical structure in a yarn. The chaotic structure of the CNT assemblies and high aspect ratio of the nanotubes causes the network to become a complex three dimensional fishing net. To remove these chaotic structures methods are needed to push the CNT past the level of elongation that can be achieved by stretching. Though DCPD and CNTs form an ideal system due to low viscosity and surface affinity, functionalization to form covalent bonds, will likely give further improvements. Also this work provides a new approach to considering the load transfer at the nanoscale between CNTs and polymer.

7.2 FUTURE WORK

7.2.1 IN SITU CHARACTERIZATION OF ALIGNMENT

To overcome the limitations in beam intensity and analysis time it would be advantageous to carry out alignment studies at a synchrotron source which would enable in situ characterization. Davies et al. [288] used the European Synchrotron Radiation Facility to characterize the fracture surface of CNT yarns with WAXS, SAXS and florescence utilizing a microscopic beam that allowed spatial resolution. This is a common technique in characterizing polymer films and fibers. Wu et al. [289] used the National Synchrotron Light Source at the Brookhaven National Laboratory to characterize the structure of Poly (vinylidene fluoride) fibers during stretching. There

189

was a clear alignment of the crystal structure to the stretching axis. A similar

arrangement is available at Beamline 7.3.3 of the Advanced Light Source Lawrence

Berkeley National Laboratory. This system incorporates a tensile testing fixture along

with environmental chambers. This equipment would allow investigation of the

structure of the CNT material while being stretched and twisted. Furthermore, it would

allow the observation of the microstructure while the DCPD polymer is being cured and

stretched. Other properties that could be investigated are creep, stress relaxation and

the structural evolution during cyclical loading.

7.2.2 ALIGNMENT BY A STABLE PROCESSES

Section 2.4 demonstrated the multitude of methods used to align carbon nanotubes

where stretching and twisting was utilized in the present research. Most of the

methods are unstable in that they apply higher stress to thin area. In a CNT fiber, thin

regions are stretched more and when twisted these thin sections twist more than thick

sections. One example of a stable process is the rolling of sheet metal. In this case a

gap can be fixed between a set of rolls and CNT material can be passed through. Thick

sections will experience more compression than thin sections and with a wide enough

cross-section the deformation will be plane strain. Alignment should develop in the

same manner as texture develops in rolled steel. This material can be deformed with

DCPD acting as a lubricant between nanotubes and then heated to lock in the aligned

structure. Thick sheets of at least a few hundred microns should be easily analyzed by

WAXS to enable good understanding of the processing parameters. The closest

published work to this rolling approach was developed by Miao [290] where two rolls

mimicked traditional hand fiber spinning. The gap was not controlled, and the soft

plastic rolls and rapid side to side shearing, made the process hard to control and the

resulting fiber properties were low. However, with the right arrangement it could be

possible to form aligned and densified CNT structures in a continuous process.

7.2.3 EXPANSION OF CAPSTAN MODEL

Expanding the capstan model would be beneficial to validate the presences of this

load transfer mechanism. This can be done by developing a finite element model that,

at first, could be a simple arrangements of rigid cylinders acting as capstans and several

bundles of nanotubes that are interlaced. The interlacing can be controlled to either

create a distribution of contact angles between CNTs and capstans or they can be

arranged into a single contact angle for all bundles. The model can then be expanded

into three dimensions by making a foam structure where the struts are tortuous bundles

of CNTs. An interesting parameter to adjust would be the stiffness of the polymer that

fills the void space. It has been shown that cross-linked polymers transfer more load to

CNT bundles [117] and that the highly cross-linked BMI resins have produced the

highest strength CNT composites [212, 216, 217]. It would be interesting to see if these

polymers act as more rigid capstans and improve load transfer by preventing the

alignment of the CNT network.

REFERENCES

[1]   Kroto HW, Heath JR, O'Brien SC, Curl RF, Smalley RE. C60: Buckminsterfullerene. Nature. 1985;318(6042):162-3.

[2]   Rohlfing EA, Cox DM, Kaldor A. Production and characterization of supersonic carbon cluster beams. The Journal of chemical physics. 1984;81(7):3322-30.

[3]   Iijima S. Helical microtubules of graphitic carbon. Nature. 1991;354(6348):56-8.

[4]   Yakobson BI, Smalley RE. Fullerene nanotubes: C 1,000,000 and beyond: Some unusual new molecules—long, hollow fibers with tantalizing electronic and mechanical properties—have joined diamonds and graphite in the carbon family. American Scientist. 1997:324-37.

[5]   Bethune DS, Klang CH, de Vries MS, Gorman G, Savoy R, Vazquez J, et al. Cobalt-catalysed growth of carbon nanotubes with single-atomic-layer walls. Nature. 1993;363(6430):605-7.

[6]   Iijima S, Ichihashi T. Single-shell carbon nanotubes of 1-nm diameter. Nature. 1993;363(6430):603-5.

[7]   Balandin AA. Thermal properties of graphene and nanostructured carbon materials. Nat Mater. 2011;10(8):569-81.

[8]   Collins PG, Avouris P. Nanotubes for electronics. Scientific american. 2000;283(6):62-9.

[9]   Li Q, Li Y, Zhang X, Chikkannanavar SB, Zhao Y, Dangelewicz AM, et al. Structure-dependent electrical properties of carbon

nanotube fibers. ADVANCED MATERIALS-DEERFIELD BEACH THEN WEINHEIM-. 2007;19(20):3358.

[10]   Demczyk BG, Wang YM, Cumings J, Hetman M, Han W, Zettl A, et al. Direct mechanical measurement of the tensile strength and elastic modulus of multiwalled carbon nanotubes. Materials Science and Engineering: A. 2002;334(1–2):173-8.

[11]   Yu M-F, Files BS, Arepalli S, Ruoff RS. Tensile Loading of Ropes of Single Wall Carbon Nanotubes and their Mechanical Properties. Physical Review Letters. 2000;84(24):5552-5.

[12]   Thayer AM. Carbon nanotubes by the metric ton. Chemical & Engineering News. 2007;85(46):29-35.

[13]   Markarian J. Flame retardants for polyamides - new developments and processing concerns. Plastics, Additives and Compounding. 2005;7(2):22-5.

[14]   Baibarac M, Gómez-Romero P. Nanocomposites based on conducting polymers and carbon nanotubes: from fancy materials to functional applications. Journal of nanoscience and nanotechnology. 2006;6(2):289-302.

[15]   Hu YS, Liu X, Müller JO, Schlögl R, Maier J, Su DS. Synthesis and Electrode Performance of Nanostructured V2O5 by Using a Carbon Tube-in-Tube as a Nanoreactor and an Efficient Mixed-Conducting Network. Angewandte Chemie International Edition. 2009;48(1):210-4.

[16]   Liu X, Hu YS, Müller JO, Schlögl R, Maier J, Su DS. Composites of Molecular-Anchored Graphene and Nanotubes with Multitubular Structure: A New Type of Carbon Electrode. ChemSusChem. 2010;3(2):261-5.

[17]   Xu YJ, Liu X, Cui G, Zhu B, Weinberg G, Schlögl R, et al. A Comparative Study on the Lithium-Ion Storage Performances of Carbon Nanotubes and Tube-in-Tube Carbon Nanotubes. ChemSusChem. 2010;3(3):343-9.

[18]   Centi G, Gangeri M, Fiorello M, Perathoner S, Amadou J, Bégin D, et al. The role of mechanically induced defects in carbon nanotubes to modify the properties of electrodes for PEM fuel cell. Catalysis Today. 2009;147(3):287-99.

[19]   Li W, Liang C, Zhou W, Qiu J, Zhou Z, Sun G, et al. Preparation and characterization of multiwalled carbon nanotube-supported platinum for cathode catalysts of direct methanol fuel cells. The Journal of Physical Chemistry B. 2003;107(26):6292-9.

[20]   Liang C, Ding L, Li C, Pang M, Su D, Li W, et al. Nanostructured WCx/CNTs as highly efficient support of electrocatalysts with low Pt loading for oxygen reduction reaction. Energy & Environmental Science. 2010;3(8):1121-7.

[21]   Nihei M, Kawabata A, Kondo D, Horibe M, Sato S, Awano Y. Electrical properties of carbon nanotube bundles for future via interconnects. Japanese journal of applied physics. 2005;44(4R):1626.

[22]   Naeemi A, Sarvari R, Meindl JD. Performance modeling and optimization for single-and multi-wall carbon nanotube interconnects. Design Automation Conference, 2007 DAC'07 44th ACM/IEEE: IEEE; p. 568-73.

[23]   Zhou C, Vyas A, Wang P, Chan M, Yang CY. Fabrication and characterization of carbon nanotube interconnect vias for next-generation technology nodes. Electron Devices and Solid-State

Circuits (EDSSC), 2014 IEEE International Conference on: IEEE; p. 1-2.

[24]   Derenskyi V, Gomulya W, Rios JMS, Fritsch M, Fröhlich N, Jung S, et al. Carbon Nanotube Network Ambipolar Field-Effect Transistors with 108 On/Off Ratio. Advanced Materials. 2014;26(34):5969-75.

[25]   Javey A, Guo J, Wang Q, Lundstrom M, Dai H. Ballistic carbon nanotube field-effect transistors. nature. 2003;424(6949):654-7.

[26]   Raffaelle R, Landi B, Harris J, Bailey S, Hepp A. Carbon nanotubes for power applications. Materials Science and Engineering: B. 2005;116(3):233-43.

[27]   Kozlov ME, Capps RC, Sampson WM, Ebron VH, Ferraris JP, Baughman RH. Spinning Solid and Hollow Polymer-Free Carbon Nanotube Fibers. Advanced Materials. 2005;17(5):614-7.

[28]   Dalton AB, Collins S, Munoz E, Razal JM, Ebron VH, Ferraris JP, et al. Super-tough carbon-nanotube fibres. Nature. 2003;423(6941):703-.

[29]   Muñoz E, Dalton AB, Collins S, Kozlov M, Razal J, Coleman JN, et al. Multifunctional Carbon Nanotube Composite Fibers. Advanced Engineering Materials. 2004;6(10):801-4.

[30]   Frackowiak E, Beguin F. Electrochemical storage of energy in carbon nanotubes and nanostructured carbons. Carbon. 2002;40(10):1775-87.

[31]   Gooding JJ. Nanostructuring electrodes with carbon nanotubes: A review on electrochemistry and applications for sensing. Electrochimica Acta. 2005;50(15):3049-60.

[32]   Jose MV, Marx S, Murata H, Koepsel RR, Russell AJ. Direct electron transfer in a mediator-free glucose oxidase-based carbon nanotube-coated biosensor. Carbon. 2012;50(11):4010-20.

[33]   Wang J. Carbon-nanotube based electrochemical biosensors: a review. Electroanalysis. 2005;17(1):7-14.

[34]   Bonard J-M, Dean KA, Coll BF, Klinke C. Field emission of individual carbon nanotubes in the scanning electron microscope. Physical review letters. 2002;89(19):197602.

[35]   Neupane S, Lastres M, Chiarella M, Li W, Su Q, Du G. Synthesis and field emission properties of vertically aligned carbon nanotube arrays on copper. Carbon. 2012;50(7):2641-50.

[36]   Cheng Y, Zhou O. Electron field emission from carbon nanotubes. Comptes Rendus Physique. 2003;4(9):1021-33.

[37]   Bonard J-M, Kind H, Stöckli T, Nilsson L-O. Field emission from carbon nanotubes: the first five years. Solid-State Electronics. 2001;45(6):893-914.

[38]   Garcia EJ, Wardle BL, Hart AJ. Joining prepreg composite interfaces with aligned carbon nanotubes. Composites Part A: Applied Science and Manufacturing. 2008;39(6):1065-70.

[39]   Breuer O, Sundararaj U. Big returns from small fibers: A review of polymer/carbon nanotube composites. Polymer Composites. 2004;25(6):630-45.

[40]   Lau AK-T, Hui D. The revolutionary creation of new advanced materials—carbon nanotube composites. Composites Part B: Engineering. 2002;33(4):263-77.

[41]   An F, Lu C, Li Y, Guo J, Lu X, Lu H, et al. Preparation and characterization of carbon nanotube-hybridized carbon fiber to reinforce epoxy composite. Materials & Design. 2012;33:197-202.

[42]   Zhong X-H, Li Y-L, Liu Y-K, Qiao X-H, Feng Y, Liang J, et al. Continuous Multilayered Carbon Nanotube Yarns. Advanced Materials. 2010;22(6):692-6.

[43]   Baughman RH, Cui C, Zakhidov AA, Iqbal Z, Barisci JN, Spinks GM, et al. Carbon Nanotube Actuators. Science. 1999;284(5418):1340-4.

[44]   Viry L, Mercader C, Miaudet P, Zakri C, Derre A, Kuhn A, et al. Nanotube fibers for electromechanical and shape memory actuators. Journal of Materials Chemistry. 2010;20(17):3487-95.

[45]   Mirfakhrai T, Oh J, Kozlov M, Fang S, Zhang M, Baughman RH, et al. Carbon Nanotube Yarn Actuators: An Electrochemical Impedance Model. Journal of The Electrochemical Society. 2009;156(6):K97-K103.

[46]   Foroughi J, Spinks GM, Wallace GG, Oh J, Kozlov ME, Fang S, et al. Torsional Carbon Nanotube Artificial Muscles. Science. 2011;334(6055):494-7.

[47]   De Volder MF, Tawfick SH, Baughman RH, Hart AJ. Carbon nanotubes: present and future commercial applications. Science. 2013;339(6119):535-9.

[48]   Baughman RH, Zakhidov AA, de Heer WA. Carbon nanotubes--the route toward applications. Science. 2002;297(5582):787-92.

[49]   Dai H. Carbon nanotubes: opportunities and challenges. Surface Science. 2002;500(1):218-41.

[50]   Robertson J. Realistic applications of CNTs. Materials Today. 2004;7(10):46-52.

[51]   Cornwell CF, Welch CR. Very-high-strength (60-GPa) carbon nanotube fiber design based on molecular dynamics simulations. The Journal of Chemical Physics. 2011;134(20):204708-8.

[52]   Salvetat-Delmotte J-P, Rubio A. Mechanical properties of carbon nanotubes: a fiber digest for beginners. Carbon. 2002;40(10):1729-34.

[53]   Coulson CA, McWeeny R. Coulson's Valence: Oxford University Press; 1979.

[54]   Silberberg M. Chemistry: The Molecular Nature of Matter and Change: McGraw-Hill; 2004.

[55]   La Torre A, Botello-Mendez A, Baaziz W, Charlier JC, Banhart F. Strain-induced metal–semiconductor transition observed in atomic carbon chains. Nat Commun. 2015;6.

[56]   Heimann R, Evsyukov SE, Kavan L. Carbyne and carbynoid structures: Springer Science & Business Media; 1999.

[57]   Liu M, Artyukhov VI, Lee H, Xu F, Yakobson BI. Carbyne from First Principles: Chain of C Atoms, a Nanorod or a Nanorope. ACS Nano. 2013;7(11):10075-82.

[58]   Jun T, Akio T, Kikuko K. Structure and Electrical Properties of Polyacetylene Yielding a Conductivity of 10 5 S/cm. Japanese Journal of Applied Physics. 1990;29(1R):125.

[59]   Berets DJ, Smith DS. Electrical properties of linear polyacetylene. Transactions of the Faraday Society. 1968;64(0):823-8.

[60]   Ansari R, Ajori S, Motevalli B. Mechanical properties of defective single-layered graphene sheets via molecular dynamics simulation. Superlattices and Microstructures. 2012;51(2):274-89.

[61]   Wehling TO, Yuan S, Lichtenstein AI, Geim AK, Katsnelson MI. Resonant Scattering by Realistic Impurities in Graphene. Physical Review Letters. 2010;105(5):056802.

[62]   Katsnelson MI. Graphene: carbon in two dimensions. Materials Today. 2007;10(1–2):20-7.

[63]   Ehrenfreund P, Foing BH. Fullerenes and Cosmic Carbon. Science. 2010;329(5996):1159-60.

[64]   Tsuzuki S, Lüthi HP. Interaction energies of van der Waals and hydrogen bonded systems calculated using density functional theory: Assessing the PW91 model. The Journal of Chemical Physics. 2001;114(9):3949-57.

[65]   Charlier JC, Gonze X, Michenaud JP. Graphite Interplanar Bonding: Electronic Delocalization and van der Waals Interaction. EPL (Europhysics Letters). 1994;28(6):403.

[66]   Bailey AC, Yates B. Anisotropic Thermal Expansion of Pyrolytic Graphite at Low Temperatures. Journal of Applied Physics. 1970;41(13):5088-91.

[67]   Thostenson ET, Ren Z, Chou T-W. Advances in the science and technology of carbon nanotubes and their composites: a

review. Composites Science and Technology. 2001;61(13):1899-912.

[68]   Li ZQ, Lu CJ, Xia ZP, Zhou Y, Luo Z. X-ray diffraction patterns of graphite and turbostratic carbon. Carbon. 2007;45(8):1686-95.

[69]   Xu Z, Bai X, Wang ZL, Wang E. Multiwall Carbon Nanotubes Made of Monochirality Graphite Shells. Journal of the American Chemical Society. 2006;128(4):1052-3.

[70]   Martins-Júnior PA, Alcântara CE, Resende RR, Ferreira AJ. Carbon Nanotubes: Directions and Perspectives in Oral Regenerative Medicine. Journal of Dental Research. 2013;92(7):575-83.

[71]   Jorio A, Saito R, Dresselhaus G, Dresselhaus MS. Raman Spectroscopy: From Graphite to sp2 Nanocarbons. Raman Spectroscopy in Graphene Related Systems: Wiley-VCH Verlag GmbH & Co. KGaA 2011, p. 73-101.

[72]   Harris P. Carbon nanotube composites. International Materials Reviews. 2004;49(1):31-43.

[73]   Dresselhaus MS, Dresselhaus G, Saito R, Jorio A. Raman spectroscopy of carbon nanotubes. Physics reports. 2005;409(2):47-99.

[74]   Xu B, Yin J, Liu Z. Phonon Scattering and Electron Transport in Single Wall Carbon Nanotube: INTECH Open Access Publisher; 2013.

[75]   Belin T, Epron F. Characterization methods of carbon nanotubes: a review. Materials Science and Engineering: B. 2005;119(2):105-18.

[76]   Saito R, Dresselhaus G, Dresselhaus MS. Physical Properties of Carbon Nanotubes: Imperial College Press; 1998.

[77]   Qin L-C, Zhao X, Hirahara K, Miyamoto Y, Ando Y, Iijima S. Materials science: The smallest carbon nanotube. Nature. 2000;408(6808):50-.

[78]   Ohta T, Bostwick A, Seyller T, Horn K, Rotenberg E. Controlling the Electronic Structure of Bilayer Graphene. Science. 2006;313(5789):951-4.

[79]   Dumitrica T, Hua M, Yakobson BI. Symmetry-, time-, and temperature-dependent strength of carbon nanotubes. Proceedings of the National Academy of Sciences. 2006;103(16):6105-9.

[80]   Yu M-F. Fundamental Mechanical Properties of Carbon Nanotubes: Current Understanding and the Related Experimental Studies. Journal of Engineering Materials and Technology. 2004;126(3):271-8.

[81]   Yao Z, Postma HWC, Balents L, Dekker C. Carbon nanotube intramolecular junctions. Nature. 1999;402(6759):273-6.

[82]   Wu J, Nagao S, He J, Zhang Z. Nanohinge-Induced Plasticity of Helical Carbon Nanotubes. Small. 2013;9(21):3561-6.

[83]   Biró LP, Lazarescu SD, Thiry PA, Fonseca A, Nagy JB, Lucas AA, et al. Scanning tunneling microscopy observation of tightly wound, single-wall coiled carbon nanotubes. EPL (Europhysics Letters). 2000;50(4):494.

[84]   Tersoff J, Ruoff RS. Structural Properties of a Carbon-Nanotube Crystal. Physical Review Letters. 1994;73(5):676-9.

[85]   López MJ, Rubio A, Alonso JA, Qin LC, Iijima S. Novel Polygonized Single-Wall Carbon Nanotube Bundles. Physical Review Letters. 2001;86(14):3056-9.

[86]   Elliott JA, Sandler JKW, Windle AH, Young RJ, Shaffer MSP. Collapse of Single-Wall Carbon Nanotubes is Diameter Dependent. Physical Review Letters. 2004;92(9):095501.

[87]   Motta M, Moisala A, Kinloch IA, Windle AH. High Performance Fibres from 'Dog Bone' Carbon Nanotubes. Advanced Materials. 2007;19(21):3721-6.

[88]   Reznik D, Olk CH, Neumann DA, Copley JRD. X-ray powder diffraction from carbon nanotubes and nanoparticles. Physical Review B. 1995;52(1):116-24.

[89]   Volkov AN, Shiga T, Nicholson D, Shiomi J, Zhigilei LV. Effect of bending buckling of carbon nanotubes on thermal conductivity of carbon nanotube materials. Journal of Applied Physics. 2012;111(5):-.

[90]   Pantano A, M. Parks D, Boyce MC. Mechanics of deformation of single- and multi-wall carbon nanotubes. Journal of the Mechanics and Physics of Solids. 2004;52(4):789-821.

[91]   Poncharal P, Wang ZL, Ugarte D, Heer WAd. Electrostatic Deflections and Electromechanical Resonances of Carbon Nanotubes. Science. 1999;283(5407):1513-6.

[92]   Qian D, Wagner GJ, Liu WK, Yu M-F, Ruoff RS. Mechanics of carbon nanotubes. Applied Mechanics Reviews. 2002;55(6):495-533.

[93]   Ruoff RS, Lorents DC. Mechanical and thermal properties of carbon nanotubes. Carbon. 1995;33(7):925-30.

[94]   Yakobson BI, Brabec CJ, Bernholc J. Nanomechanics of Carbon Tubes: Instabilities beyond Linear Response. Physical Review Letters. 1996;76(14):2511-4.

[95]   Lu JP. Elastic Properties of Carbon Nanotubes and Nanoropes. Physical Review Letters. 1997;79(7):1297-300.

[96]   Seldin EJ, Nezbeda CW. Elastic Constants and Electron-Microscope Observations of Neutron-Irradiated Compression-Annealed Pyrolytic and Single-Crystal Graphite. Journal of Applied Physics. 1970;41(8):3389-400.

[97]   Ding W, Calabri L, Kohlhaas KM, Chen X, Dikin DA, Ruoff RS. Modulus, Fracture Strength, and Brittle vs. Plastic Response of the Outer Shell of Arc-grown Multi-walled Carbon Nanotubes. Exp Mech. 2007;47(1):25-36.

[98]   Zhao Q, Nardelli MB, Bernholc J. Ultimate strength of carbon nanotubes: A theoretical study. Physical Review B. 2002;65(14):144105.

[99]   Buongiorno Nardelli M, Yakobson BI, Bernholc J. Mechanism of strain release in carbon nanotubes. Physical Review B. 1998;57(8):R4277-R80.

[100] Zhang R, Wen Q, Qian W, Su DS, Zhang Q, Wei F. Superstrong Ultralong Carbon Nanotubes for Mechanical Energy Storage. Advanced Materials. 2011;23(30):3387-91.

[101] Berber S, Kwon Y-K, Tománek D. Unusually High Thermal Conductivity of Carbon Nanotubes. Physical Review Letters. 2000;84(20):4613-6.

[102] Anthony TR, Banholzer WF, Fleischer JF, Wei L, Kuo PK, Thomas RL, et al. Thermal diffusivity of isotopically enriched $^{12}\mathrm{C}$ diamond. Physical Review B. 1990;42(2):1104-11.

[103] Jiang H, Liu B, Huang Y, Hwang KC. Thermal Expansion of Single Wall Carbon Nanotubes. Journal of Engineering Materials and Technology. 2004;126(3):265-70.

[104] Maniwa Y, Fujiwara R, Kira H, Tou H, Kataura H, Suzuki S, et al. Thermal expansion of single-walled carbon nanotube (SWNT) bundles: X-ray diffraction studies. Physical Review B. 2001;64(24):241402.

[105] McEuen PL, Bockrath M, Cobden DH, Yoon Y-G, Louie SG. Disorder, Pseudospins, and Backscattering in Carbon Nanotubes. Physical Review Letters. 1999;83(24):5098-101.

[106] McEuen PL. Single-wall carbon nanotubes. Physics World. 2000;13(6):31-6.

[107] Kong J, Yenilmez E, Tombler TW, Kim W, Dai H, Laughlin RB, et al. Quantum Interference and Ballistic Transmission in Nanotube Electron Waveguides. Physical Review Letters. 2001;87(10):106801.

[108] Dürkop T, Getty SA, Cobas E, Fuhrer MS. Extraordinary Mobility in Semiconducting Carbon Nanotubes. Nano Letters. 2004;4(1):35-9.

[109] Frank S, Poncharal P, Wang ZL, Heer WAd. Carbon Nanotube Quantum Resistors. Science. 1998;280(5370):1744-6.

[110] McEuen PL, Fuhrer MS, Park H. Single-walled carbon nanotube electronics. Nanotechnology, IEEE Transactions on. 2002;1(1):78-85.

[111] Gao B, Chen YF, Fuhrer MS, Glattli DC, Bachtold A. Four-Point Resistance of Individual Single-Wall Carbon Nanotubes. Physical Review Letters. 2005;95(19):196802.

[112] Chen Q, Wang S, Peng L-M. Establishing Ohmic contacts for in situ current–voltage characteristic measurements on a carbon nanotube inside the scanning electron microscope. Nanotechnology. 2006;17(4):1087.

[113] Kim W, Javey A, Tu R, Cao J, Wang Q, Dai H. Electrical contacts to carbon nanotubes down to 1nm in diameter. Applied Physics Letters. 2005;87(17):173101.

[114] Odom TW, Huang J-L, Kim P, Lieber CM. Atomic structure and electronic properties of single-walled carbon nanotubes. Nature. 1998;391(6662):62-4.

[115] Dresselhaus M, Dresselhaus G, Jorio A, Souza Filho A, Saito R. Raman spectroscopy on isolated single wall carbon nanotubes. Carbon. 2002;40(12):2043-61.

[116] Jishi RA, Venkataraman L, Dresselhaus MS, Dresselhaus G. Phonon modes in carbon nanotubules. Chemical Physics Letters. 1993;209(1–2):77-82.

[117] Ma W, Liu L, Zhang Z, Yang R, Liu G, Zhang T, et al. High-Strength Composite Fibers: Realizing True Potential of Carbon

Nanotubes in Polymer Matrix through Continuous Reticulate Architecture and Molecular Level Couplings. Nano Letters. 2009;9(8):2855-61.

[118] Schadler LS, Giannaris SC, Ajayan PM. Load transfer in carbon nanotube epoxy composites. Applied Physics Letters. 1998;73(26):3842-4.

[119] O'Connell MJ, Bachilo SM, Huffman CB, Moore VC, Strano MS, Haroz EH, et al. Band Gap Fluorescence from Individual Single-Walled Carbon Nanotubes. Science. 2002;297(5581):593-6.

[120] Wang F, Dukovic G, Brus LE, Heinz TF. The optical resonances in carbon nanotubes arise from excitons. Science. 2005;308(5723):838-41.

[121] Zhang Y, Franklin NW, Chen RJ, Dai H. Metal coating on suspended carbon nanotubes and its implication to metal–tube interaction. Chemical Physics Letters. 2000;331(1):35-41.

[122] Collins PG, Bradley K, Ishigami M, Zettl A. Extreme Oxygen Sensitivity of Electronic Properties of Carbon Nanotubes. Science. 2000;287(5459):1801-4.

[123] Rahman MM, Umar A, Sawada K. Development of amperometric glucose biosensor based on glucose oxidase co-immobilized with multi-walled carbon nanotubes at low potential. Sensors and Actuators B: Chemical. 2009;137(1):327-33.

[124] Suekane O, Nagataki A, Mori H, Nakayama Y. Static Friction Force of Carbon Nanotube Surfaces. Appl Phys Express. 2008;1:3.

[125] Ebbesen TW, Ajayan PM. Large-scale synthesis of carbon nanotubes. Nature. 1992;358(6383):220-2.

[126] Seraphin S, Zhou D, Jiao J, Withers JC, Loutfy R. Effect of processing conditions on the morphology and yield of carbon nanotubes. Carbon. 1993;31(5):685-9.

[127] Rafique MMA, Iqbal J. Production of carbon nanotubes by different routes-a review. Journal of encapsulation and adsorption sciences. 2011;1(02):29.

[128] Journet C, Maser WK, Bernier P, Loiseau A, de la Chapelle ML, Lefrant S, et al. Large-scale production of single-walled carbon nanotubes by the electric-arc technique. Nature. 1997;388(6644):756-8.

[129] Bethune DS, Beyers RB, Kiang CH. Carbon fibers and method for their production. Google Patents 1995.

[130] Nishi Y, Mukai H, Ozamoto D. Process for producing carbon nanotubes by arc discharge. Google Patents 2009.

[131] Guo T, Nikolaev P, Thess A, Colbert DT, Smalley RE. Catalytic growth of single-walled manotubes by laser vaporization. Chemical Physics Letters. 1995;243(1–2):49-54.

[132] Yudasaka M, Yamada R, Sensui N, Wilkins T, Ichihashi T, Iijima S. Mechanism of the Effect of NiCo, Ni and Co Catalysts on the Yield of Single-Wall Carbon Nanotubes Formed by Pulsed Nd:YAG Laser Ablation. The Journal of Physical Chemistry B. 1999;103(30):6224-9.

[133] Bandow S, Asaka S, Saito Y, Rao AM, Grigorian L, Richter E, et al. Effect of the Growth Temperature on the Diameter Distribution and Chirality of Single-Wall Carbon Nanotubes. Physical Review Letters. 1998;80(17):3779-82.

[134] Puretzky AA, Geohegan DB, Fan X, Pennycook SJ. Dynamics of single-wall carbon nanotube synthesis by laser vaporization. Applied Physics A. 2000;70(2):153-60.

[135] Landi BJ, Raffaelle RP. Effects of Carrier Gas Dynamics on Single Wall Carbon Nanotube Chiral Distributions During Laser Vaporization Synthesis. Journal of Nanoscience and Nanotechnology. 2007;7(3):883-90.

[136] Thess A, Lee R, Nikolaev P, Dai H, Petit P, Robert J, et al. Crystalline Ropes of Metallic Carbon Nanotubes. Science. 1996;273(5274):483-7.

[137] Baker RTK, Barber MA, Harris PS, Feates FS, Waite RJ. Nucleation and growth of carbon deposits from the nickel catalyzed decomposition of acetylene. Journal of Catalysis. 1972;26(1):51-62.

[138] Jourdain V, Bichara C. Current understanding of the growth of carbon nanotubes in catalytic chemical vapour deposition. Carbon. 2013;58:2-39.

[139] Wang Y, Luo Z, Li B, Ho PS, Yao Z, Shi L, et al. Comparison study of catalyst nanoparticle formation and carbon nanotube growth: Support effect. Journal of Applied Physics. 2007;101(12):124310.

[140] Noda S, Hasegawa K, Sugime H, Kakehi K, Zhang Z, Maruyama S, et al. Millimeter-Thick Single-Walled Carbon Nanotube Forests: Hidden Role of Catalyst Support. Japanese Journal of Applied Physics. 2007;46(5L):L399.

[141] Vander Wal RL, Ticich TM, Curtis VE. Substrate–support interactions in metal-catalyzed carbon nanofiber growth. Carbon. 2001;39(15):2277-89.

[142] Colomer JF, Stephan C, Lefrant S, Van Tendeloo G, Willems I, Kónya Z, et al. Large-scale synthesis of single-wall carbon nanotubes by catalytic chemical vapor deposition (CCVD) method. Chemical Physics Letters. 2000;317(1–2):83-9.

[143] Kathyayini H, Nagaraju N, Fonseca A, Nagy JB. Catalytic activity of Fe, Co and Fe/Co supported on Ca and Mg oxides, hydroxides and carbonates in the synthesis of carbon nanotubes. Journal of Molecular Catalysis A: Chemical. 2004;223(1–2):129-36.

[144] Kong J, Cassell AM, Dai H. Chemical vapor deposition of methane for single-walled carbon nanotubes. Chemical Physics Letters. 1998;292(4–6):567-74.

[145] Couteau E, Hernadi K, Seo JW, Thiên-Nga L, Mikó C, Gaál R, et al. CVD synthesis of high-purity multiwalled carbon nanotubes using CaCO3 catalyst support for large-scale production. Chemical Physics Letters. 2003;378(1–2):9-17.

[146] Zhao N, He C, Jiang Z, Li J, Li Y. Fabrication and growth mechanism of carbon nanotubes by catalytic chemical vapor deposition. Materials Letters. 2006;60(2):159-63.

[147] Kitiyanan B, Alvarez WE, Harwell JH, Resasco DE. Controlled production of single-wall carbon nanotubes by catalytic decomposition of CO on bimetallic Co–Mo catalysts. Chemical Physics Letters. 2000;317(3–5):497-503.

[148] Resasco DE, Alvarez WE, Pompeo F, Balzano L, Herrera JE, Kitiyanan B, et al. A Scalable Process for Production of Single-

walled Carbon Nanotubes (SWNTs) by Catalytic Disproportionation of CO on a Solid Catalyst. Journal of Nanoparticle Research. 2002;4(1-2):131-6.

[149] Qian W, Liu T, Wei F, Wang Z, Li Y. Enhanced production of carbon nanotubes: combination of catalyst reduction and methane decomposition. Applied Catalysis A: General. 2004;258(1):121-4.

[150] Corrias M, Caussat B, Ayral A, Durand J, Kihn Y, Kalck P, et al. Carbon nanotubes produced by fluidized bed catalytic CVD: first approach of the process. Chemical Engineering Science. 2003;58(19):4475-82.

[151] Qian D, Liu WK, Ruoff RS. Load transfer mechanism in carbon nanotube ropes. Composites Science and Technology. 2003;63(11):1561-9.

[152] Li WZ, Xie SS, Qian LX, Chang BH, Zou BS, Zhou WY, et al. Large-Scale Synthesis of Aligned Carbon Nanotubes. Science. 1996;274(5293):1701-3.

[153] Huang ZP, Xu JW, Ren ZF, Wang JH, Siegal MP, Provencio PN. Growth of highly oriented carbon nanotubes by plasma-enhanced hot filament chemical vapor deposition. Applied Physics Letters. 1998;73(26):3845-7.

[154] Zhang Y, Zou G, Doorn SK, Htoon H, Stan L, Hawley ME, et al. Tailoring the Morphology of Carbon Nanotube Arrays: From Spinnable Forests to Undulating Foams. ACS Nano. 2009;3(8):2157-62.

[155] Ren ZF, Huang ZP, Xu JW, Wang JH, Bush P, Siegal MP, et al. Synthesis of Large Arrays of Well-Aligned Carbon Nanotubes on Glass. Science. 1998;282(5391):1105-7.

[156] Lepró X, Lima MD, Baughman RH. Spinnable carbon nanotube forests grown on thin, flexible metallic substrates. Carbon. 2010;48(12):3621-7.

[157] Bower C, Zhu W, Jin S, Zhou O. Plasma-induced alignment of carbon nanotubes. Applied Physics Letters. 2000;77(6):830-2.

[158] Huang S, Cai X, Liu J. Growth of Millimeter-Long and Horizontally Aligned Single-Walled Carbon Nanotubes on Flat Substrates. Journal of the American Chemical Society. 2003;125(19):5636-7.

[159] Zheng LX, O'Connell MJ, Doorn SK, Liao XZ, Zhao YH, Akhadov EA, et al. Ultralong single-wall carbon nanotubes. Nat Mater. 2004;3(10):673-6.

[160] Wang X, Li Q, Xie J, Jin Z, Wang J, Li Y, et al. Fabrication of Ultralong and Electrically Uniform Single-Walled Carbon Nanotubes on Clean Substrates. Nano Letters. 2009;9(9):3137-41.

[161] Wen Q, Zhang R, Qian W, Wang Y, Tan P, Nie J, et al. Growing 20 cm Long DWNTs/TWNTs at a Rapid Growth Rate of 80–90 μm/s. Chemistry of Materials. 2010;22(4):1294-6.

[162] Zhang R, Zhang Y, Zhang Q, Xie H, Qian W, Wei F. Growth of Half-Meter Long Carbon Nanotubes Based on Schulz–Flory Distribution. ACS Nano. 2013;7(7):6156-61.

[163] Hofmann M, Nezich D, Reina A, Kong J. In-Situ Sample Rotation as a Tool to Understand Chemical Vapor Deposition Growth of Long Aligned Carbon Nanotubes. Nano Letters. 2008;8(12):4122-7.

[164] Nikolaev P, Bronikowski MJ, Bradley RK, Rohmund F, Colbert DT, Smith KA, et al. Gas-phase catalytic growth of single-walled carbon nanotubes from carbon monoxide. Chemical Physics Letters. 1999;313(1–2):91-7.

[165] Bronikowski MJ, Willis PA, Colbert DT, Smith KA, Smalley RE. Gas-phase production of carbon single-walled nanotubes from carbon monoxide via the HiPco process: A parametric study. Journal of Vacuum Science & Technology A. 2001;19(4):1800-5.

[166] Vazquez E, Georgakilas V, Prato M. Microwave-assisted purification of HIPCO carbon nanotubes. Chemical Communications. 2002(20):2308-9.

[167] Nasibulin AG, Moisala A, Brown DP, Jiang H, Kauppinen EI. A novel aerosol method for single walled carbon nanotube synthesis. Chemical Physics Letters. 2005;402(1–3):227-32.

[168] Chen Y, Sun Z, Li YN, Tay BK. Optimization of carbon nanotube powder growth using low pressure floating catalytic chemical vapor deposition. Materials Chemistry and Physics. 2006;98(2–3):256-60.

[169] Hiraoka T, Bandow S, Shinohara H, Iijima S. Control on the diameter of single-walled carbon nanotubes by changing the pressure in floating catalyst CVD. Carbon. 2006;44(9):1853-9.

[170] Fan Y-Y, Kaufmann A, Mukasyan A, Varma A. Single- and multi-wall carbon nanotubes produced using the floating catalyst method: Synthesis, purification and hydrogen up-take. Carbon. 2006;44(11):2160-70.

[171] Andrews R, Jacques D, Rao AM, Derbyshire F, Qian D, Fan X, et al. Continuous production of aligned carbon nanotubes: a step closer to commercial realization. Chemical Physics Letters. 1999;303(5–6):467-74.

[172] Mayne M, Grobert N, Terrones M, Kamalakaran R, Rühle M, Kroto HW, et al. Pyrolytic production of aligned carbon nanotubes from homogeneously dispersed benzene-based aerosols. Chemical Physics Letters. 2001;338(2–3):101-7.

[173] Zhu HW, Xu CL, Wu DH, Wei BQ, Vajtai R, Ajayan PM. Direct Synthesis of Long Single-Walled Carbon Nanotube Strands. Science. 2002;296(5569):884-6.

[174] Lupo F, Rodríguez-Manzo JA, Zamudio A, Elías AL, Kim YA, Hayashi T, et al. Pyrolytic synthesis of long strands of large diameter single-walled carbon nanotubes at atmospheric pressure in the absence of sulphur and hydrogen. Chemical Physics Letters. 2005;410(4-6):384-90.

[175] Li Y-L, Kinloch IA, Windle AH. Direct Spinning of Carbon Nanotube Fibers from Chemical Vapor Deposition Synthesis. Science. 2004;304(5668):276-8.

[176] Koziol K, Vilatela J, Moisala A, Motta M, Cunniff P, Sennett M, et al. High-Performance Carbon Nanotube Fiber. Science. 2007;318(5858):1892-5.

[177] Lashmore D, Brown J, Dean R, Antoinette P. Systems and methods of synthesis of extended length nanostructures. Google Patents 2008.

[178] Lashmore D, Brown JJ, Dean RC, Antoinette PL. Systems and methods for synthesis of extended length nanostructures. Google Patents 2009.

[179] Ci L, Li Y, Wei B, Liang J, Xu C, Wu D. Preparation of carbon nanofibers by the floating catalyst method. Carbon. 2000;38(14):1933-7.

[180] Chung Y-H, Jou S. Carbon nanotubes from catalytic pyrolysis of polypropylene. Materials Chemistry and Physics. 2005;92(1):256-9.

[181] Nakazawa S, Yokomori T, Mizomoto M. Flame synthesis of carbon nanotubes in a wall stagnation flow. Chemical Physics Letters. 2005;403(1–3):158-62.

[182] Zhang YF, Gamo MN, Xiao CY, Ando T. Liquid phase synthesis of carbon nanotubes. Physica B: Condensed Matter. 2002;323(1–4):293-5.

[183] G.Z. C, D.J. F. Recent development in electrolytic formation of carbon nanotubes in molten salts. Journal of Mining and Metallurgy, Section B : Metallurgy. 2003.

[184] Sears K, Skourtis C, Atkinson K, Finn N, Humphries W. Focused ion beam milling of carbon nanotube yarns to study the relationship between structure and strength. Carbon. 2010;48(15):4450-6.

[185] Liu, Phang IY, Shen L, Chow SY, Zhang W-D. Morphology and Mechanical Properties of Multiwalled Carbon Nanotubes Reinforced Nylon-6 Composites. Macromolecules. 2004;37(19):7214-22.

[186] Cadek M, Coleman JN, Barron V, Hedicke K, Blau WJ. Morphological and mechanical properties of carbon-nanotube-reinforced semicrystalline and amorphous polymer composites. Applied Physics Letters. 2002;81(27):5123-5.

[187] Ruan SL, Gao P, Yang XG, Yu TX. Toughening high performance ultrahigh molecular weight polyethylene using multiwalled carbon nanotubes. Polymer. 2003;44(19):5643-54.

[188] Chang TE, Jensen LR, Kisliuk A, Pipes RB, Pyrz R, Sokolov AP. Microscopic mechanism of reinforcement in single-wall carbon nanotube/polypropylene nanocomposite. Polymer. 2005;46(2):439-44.

[189] Wong M, Paramsothy M, Xu XJ, Ren Y, Li S, Liao K. Physical interactions at carbon nanotube-polymer interface. Polymer. 2003;44(25):7757-64.

[190] White KL, Li P, Sumi Y, Sue H-J. Rheology of Disentangled Multiwalled Carbon Nanotubes Dispersed in Uncured Epoxy Fluid. The Journal of Physical Chemistry B. 2014;118(1):362-71.

[191] Shaffer MSP, Fan X, Windle AH. Dispersion and packing of carbon nanotubes. Carbon. 1998;36(11):1603-12.

[192] Wang Z, Liang Z, Wang B, Zhang C, Kramer L. Processing and property investigation of single-walled carbon nanotube (SWNT) buckypaper/epoxy resin matrix nanocomposites. Composites Part A: Applied Science and Manufacturing. 2004;35(10):1225-32.

[193] Vigolo B, Pénicaud A, Coulon C, Sauder C, Pailler R, Journet C, et al. Macroscopic Fibers and Ribbons of Oriented Carbon Nanotubes. Science. 2000;290(5495):1331-4.

[194] Vigolo B, Poulin P, Lucas M, Launois P, Bernier P. Improved structure and properties of single-wall carbon nanotube spun fibers. Applied Physics Letters. 2002;81(7):1210-2.

[195] Young K, Blighe FM, Vilatela JJ, Windle AH, Kinloch IA, Deng L, et al. Strong Dependence of Mechanical Properties on Fiber Diameter for Polymer–Nanotube Composite Fibers: Differentiating Defect from Orientation Effects. ACS Nano. 2010;4(11):6989-97.

[196] Steinmetz J, Glerup M, Paillet M, Bernier P, Holzinger M. Production of pure nanotube fibers using a modified wet-spinning method. Carbon. 2005;43(11):2397-400.

[197] Badaire S, Pichot V, Zakri C, Poulin P, Launois P, Vavro J, et al. Correlation of properties with preferred orientation in coagulated and stretch-aligned single-wall carbon nanotubes. Journal of Applied Physics. 2004;96(12):7509-13.

[198] Davis VA, Ericson LM, Parra-Vasquez ANG, Fan H, Wang Y, Prieto V, et al. Phase Behavior and Rheology of SWNTs in Superacids. Macromolecules. 2003;37(1):154-60.

[199] Ericson LM, Fan H, Peng H, Davis VA, Zhou W, Sulpizio J, et al. Macroscopic, Neat, Single-Walled Carbon Nanotube Fibers. Science. 2004;305(5689):1447-50.

[200] Behabtu N, Young CC, Tsentalovich DE, Kleinerman O, Wang X, Ma AWK, et al. Strong, Light, Multifunctional Fibers of Carbon Nanotubes with Ultrahigh Conductivity. Science. 2013;339(6116):182-6.

[201] Jiang K, Li Q, Fan S. Nanotechnology: Spinning continuous carbon nanotube yarns. Nature. 2002;419(6909):801-.

[202] Zhu C, Cheng C, He YH, Wang L, Wong TL, Fung KK, et al. A self-entanglement mechanism for continuous pulling of carbon nanotube yarns. Carbon. 2011;49(15):4996-5001.

[203] Zhang X, Jiang K, Feng C, Liu P, Zhang L, Kong J, et al. Spinning and Processing Continuous Yarns from 4-Inch Wafer Scale Super-Aligned Carbon Nanotube Arrays. Advanced Materials. 2006;18(12):1505-10.

[204] Zhang M, Atkinson KR, Baughman RH. Multifunctional Carbon Nanotube Yarns by Downsizing an Ancient Technology. Science. 2004;306(5700):1358-61.

[205] Zhang M, Fang S, Zakhidov AA, Lee SB, Aliev AE, Williams CD, et al. Strong, Transparent, Multifunctional, Carbon Nanotube Sheets. Science. 2005;309(5738):1215-9.

[206] Aliev AE, Guthy C, Zhang M, Fang S, Zakhidov AA, Fischer JE, et al. Thermal transport in MWCNT sheets and yarns. Carbon. 2007;45(15):2880-8.

[207] Atkinson KR, Hawkins SC, Huynh C, Skourtis C, Dai J, Zhang M, et al. Multifunctional carbon nanotube yarns and transparent sheets: Fabrication, properties, and applications. Physica B: Condensed Matter. 2007;394(2):339-43.

[208] Zhang Y, Zheng L, Sun G, Zhan Z, Liao K. Failure mechanisms of carbon nanotube fibers under different strain rates. Carbon. 2012;50(8):2887-93.

[209] Naraghi M, Filleter T, Moravsky A, Locascio M, Loutfy RO, Espinosa HD. A Multiscale Study of High Performance Double-Walled Nanotube–Polymer Fibers. ACS Nano. 2010;4(11):6463-76.

[210] Zheng L, Sun G, Zhan Z. Tuning Array Morphology for High Strength Carbon Nanotube Fibers. Small. 2010;6(1):132-7.

[211] Zhang X, Li Q, Tu Y, Li Y, Coulter JY, Zheng L, et al. Strong Carbon-Nanotube Fibers Spun from Long Carbon-Nanotube Arrays. Small. 2007;3(2):244-8.

[212] Wang X, Yong ZZ, Li QW, Bradford PD, Liu W, Tucker DS, et al. Ultrastrong, Stiff and Multifunctional Carbon Nanotube Composites. Materials Research Letters. 2012:1-7.

[213] Cooper CH, Zhang HF, Czerw R. Methods for the production of aligned carbon nanotubes and nanostructured material containing the same. Google Patents 2012.

[214] Lemaire AB, Lemaire CA, Stordal LT, Thomforde DJ. Method for growing carbon nanotube forests, and generating nanotube structures therefrom, and apparatus. Google Patents 2013.

[215] Vilatela JJ, Windle AH. Yarn-Like Carbon Nanotube Fibers. Advanced Materials. 2010;22(44):4959-63.

[216] Cheng Q, Bao J, Park J, Liang Z, Zhang C, Wang B. High Mechanical Performance Composite Conductor: Multi-Walled Carbon Nanotube Sheet/Bismaleimide Nanocomposites. Advanced Functional Materials. 2009;19(20):3219-25.

[217] Cheng Q, Wang B, Zhang C, Liang Z. Functionalized Carbon-Nanotube Sheet/Bismaleimide Nanocomposites: Mechanical and Electrical Performance Beyond Carbon-Fiber Composites. Small. 2010;6(6):763-7.

[218] Gommans HH, Alldredge JW, Tashiro H, Park J, Magnuson J, Rinzler AG. Fibers of aligned single-walled carbon nanotubes:

Polarized Raman spectroscopy. Journal of Applied Physics. 2000;88(5):2509-14.

[219] Worsley MA, Kucheyev SO, Satcher JH, Hamza AV, Baumann TF. Mechanically robust and electrically conductive carbon nanotube foams. Applied Physics Letters. 2009;94(7):073115.

[220] Bryning MB, Milkie DE, Islam MF, Hough LA, Kikkawa JM, Yodh AG. Carbon Nanotube Aerogels. Advanced Materials. 2007;19(5):661-4.

[221] Zhang S, Koziol KKK, Kinloch IA, Windle AH. Macroscopic Fibers of Well-Aligned Carbon Nanotubes by Wet Spinning. Small. 2008;4(8):1217-22.

[222] Futaba DN, Hata K, Yamada T, Hiraoka T, Hayamizu Y, Kakudate Y, et al. Shape-engineerable and highly densely packed single-walled carbon nanotubes and their application as super-capacitor electrodes. Nat Mater. 2006;5(12):987-94.

[223] Alexander LE. X-ray diffraction methods in polymer science: Wiley-Interscience; 1969.

[224] Cullity BD, Stock SR. Elements of X-ray Diffraction: Prentice hall Upper Saddle River, NJ; 2001.

[225] Jin L, Bower C, Zhou O. Alignment of carbon nanotubes in a polymer matrix by mechanical stretching. Applied Physics Letters. 1998;73(9):1197-9.

[226] Hermans PH. Contribution to the physics of cellulose fibres : a study in sorption, density, refractive power and orientation. Amsterdam; London: Elsevier; 1946.

[227] deHeer WA, Bacsa WS, Châtelain A, Gerfin T, Humphrey-Baker R, Forro L, et al. Aligned Carbon Nanotube Films: Production and Optical and Electronic Properties. Science. 1995;268(5212):845-7.

[228] Tran CD, Humphries W, Smith SM, Huynh C, Lucas S. Improving the tensile strength of carbon nanotube spun yarns using a modified spinning process. Carbon. 2009;47(11):2662-70.

[229] Ajayan PM, Stephan O, Colliex C, Trauth D. Aligned Carbon Nanotube Arrays Formed by Cutting a Polymer Resin—Nanotube Composite. Science. 1994;265(5176):1212-4.

[230] Du F, Fischer JE, Winey KI. Effect of nanotube alignment on percolation conductivity in carbon nanotube/polymer composites. Physical Review B. 2005;72(12):121404.

[231] Miaudet P, Badaire S, Maugey M, Derré A, Pichot V, Launois P, et al. Hot-Drawing of Single and Multiwall Carbon Nanotube Fibers for High Toughness and Alignment. Nano Letters. 2005;5(11):2212-5.

[232] Sreekumar TV, Liu T, Min BG, Guo H, Kumar S, Hauge RH, et al. Polyacrylonitrile Single-Walled Carbon Nanotube Composite Fibers. Advanced Materials. 2004;16(1):58-61.

[233] Zhang S, Zhu L, Minus M, Chae H, Jagannathan S, Wong C-P, et al. Solid-state spun fibers and yarns from 1-mm long carbon nanotube forests synthesized by water-assisted chemical vapor deposition. J Mater Sci. 2008;43(13):4356-62.

[234] Bubke K, Gnewuch H, Hempstead M, Hammer J, Green MLH. Optical anisotropy of dispersed carbon nanotubes induced by an electric field. Applied Physics Letters. 1997;71(14):1906-8.

[235] Martin CA, Sandler JKW, Windle AH, Schwarz MK, Bauhofer W, Schulte K, et al. Electric field-induced aligned multi-wall carbon nanotube networks in epoxy composites. Polymer. 2005;46(3):877-86.

[236] Smith BW, Benes Z, Luzzi DE, Fischer JE, Walters DA, Casavant MJ, et al. Structural anisotropy of magnetically aligned single wall carbon nanotube films. Applied Physics Letters. 2000;77(5):663-5.

[237] Fisher FT, Bradshaw RD, Brinson LC. Fiber waviness in nanotube-reinforced polymer composites—I: Modulus predictions using effective nanotube properties. Composites Science and Technology. 2003;63(11):1689-703.

[238] Hone J, Llaguno MC, Nemes NM, Johnson AT, Fischer JE, Walters DA, et al. Electrical and thermal transport properties of magnetically aligned single wall carbon nanotube films. Applied Physics Letters. 2000;77(5):666-8.

[239] Wang D, Song P, Liu C, Wu W, Fan S. Highly oriented carbon nanotube papers made of aligned carbon nanotubes. Nanotechnology. 2008;19(7):075609.

[240] Bradford PD, Wang X, Zhao H, Maria J-P, Jia Q, Zhu YT. A novel approach to fabricate high volume fraction nanocomposites with long aligned carbon nanotubes. Composites Science and Technology. 2010;70(13):1980-5.

[241] Vilatela JJ, Elliott JA, Windle AH. A Model for the Strength of Yarn-like Carbon Nanotube Fibers. ACS Nano. 2011;5(3):1921-7.

[242] Porwal P, Beyerlein I, Phoenix S. Statistical strength of twisted fiber bundles with load sharing controlled by frictional length

scales. Journal of Mechanics of materials and Structures. 2007;2(4):773-91.

[243] Beyerlein IJ, Porwal PK, Zhu YT, Xu XF, Phoenix SL. Probabilistic Strength of Carbon Nanotube Yarns

Advances in Mathematical Modeling and Experimental Methods for Materials and Structures. In: Gilat R, Banks-Sills L, eds.: Springer Netherlands 2009, p. 211-22.

[244] Gou J, Liang Z, Zhang C, Wang B. Computational analysis of effect of single-walled carbon nanotube rope on molecular interaction and load transfer of nanocomposites. Composites Part B: Engineering. 2005;36(6–7):524-33.

[245] Jorio A, Dresselhaus G, Dresselhaus MS. Carbon Nanotubes: Advanced Topics in the Synthesis, Structure, Properties and Applications: Springer; 2008.

[246] Ando Y, Iijima S. Preparation of Carbon Nanotubes by Arc-Discharge Evaporation. Japanese Journal of Applied Physics. 1993;32(1A):L107.

[247] Xie SS, Li WZ, Pan ZW, Chang BH, Sun LF. Carbon nanotube arrays. Eur Phys J D. 1999;9(1):85-9.

[248] Stano K, Koziol K, Pick M, Motta M, Moisala A, Vilatela J, et al. Direct spinning of carbon nanotube fibres from liquid feedstock. Int J Mater Form. 2008;1(2):59-62.

[249] Zhang S, Lin W, Wong C-P, Bucknall DG, Kumar S. Nanocomposites of Carbon Nanotube Fibers Prepared by Polymer Crystallization. ACS Applied Materials & Interfaces. 2010;2(6):1642-7.

[250] Samuels RJ. Structured Polymer Properties: The Identification, Interpretation, and Application of Crystalline Polymer Structure: John Wiley; 1974.

[251] Lashmore DS, inventor Nanocomp Technologies, Inc., assignee. Supercapacitors and Methods of Manufacturing Same. United States of America. 2008.

[252] Huang W, Wang Y, Luo G, Wei F. 99.9% purity multi-walled carbon nanotubes by vacuum high-temperature annealing. Carbon. 2003;41(13):2585-90.

[253] Shi Z, Lian Y, Liao F, Zhou X, Gu Z, Zhang Y, et al. Purification of single-wall carbon nanotubes. Solid State Communications. 1999;112(1):35-7.

[254] Chen XH, Chen CS, Chen Q, Cheng FQ, Zhang G, Chen ZZ. Non-destructive purification of multi-walled carbon nanotubes produced by catalyzed CVD. Materials Letters. 2002;57(3):734-8.

[255] Saito Y, Yoshikawa T, Bandow S, Tomita M, Hayashi T. Interlayer spacings in carbon nanotubes. Physical Review B. 1993;48(3):1907-9.

[256] Data J--ICfD, Society AC. Powder Diffraction File: Hanawalt Search Manual Inorganic Phases Sets 1-42: International Centre for Diffraction Data; 1992.

[257] Saxby JD, Chatfield SP, Palmisano AJ, Vassallo AM, Wilson MA, Pang LSK. Thermogravimetric analysis of buckminsterfullerene and related materials in air. The Journal of Physical Chemistry. 1992;96(1):17-8.

[258] Bom D, Andrews R, Jacques D, Anthony J, Chen B, Meier MS, et al. Thermogravimetric Analysis of the Oxidation of Multiwalled Carbon Nanotubes: Evidence for the Role of Defect Sites in Carbon Nanotube Chemistry. Nano Letters. 2002;2(6):615-9.

[259] Di J, Hu D, Chen H, Yong Z, Chen M, Feng Z, et al. Ultrastrong, Foldable, and Highly Conductive Carbon Nanotube Film. ACS Nano. 2012;6(6):5457-64.

[260] Liu K, Sun Y, Chen L, Feng C, Feng X, Jiang K, et al. Controlled Growth of Super-Aligned Carbon Nanotube Arrays for Spinning Continuous Unidirectional Sheets with Tunable Physical Properties. Nano Letters. 2008;8(2):700-5.

[261] Nakagawa K. Foam Materials Made from Carbon Nanotubes; 2011.

[262] Kai L, Yinghui S, Ruifeng Z, Hanyu Z, Jiaping W, Liang L, et al. Carbon nanotube yarns with high tensile strength made by a twisting and shrinking method. Nanotechnology. 2010;21(4):045708.

[263] Cheng QF, Wang JP, Wen JJ, Liu CH, Jiang KL, Li QQ, et al. Carbon nanotube/epoxy composites fabricated by resin transfer molding. Carbon. 2010;48(1):260-6.

[264] Yao Z, Zhou L-w, Dai B-b, Cao K. Ring-opening metathesis copolymerization of dicyclopentadiene and cyclopentene through reaction injection molding process. Journal of Applied Polymer Science. 2012;125(4):2489-93.

[265] Kessler M, Larin G, Bernklau N. Cure characterization and viscosity development of ring-opening metathesis polymerized

resins. Journal of Thermal Analysis and Calorimetry. 2006;85(1):7-12.

[266] Sheng X, Kessler MR, Lee JK. The influence of cross-linking agents on ring-opening metathesis polymerized thermosets. Journal of Thermal Analysis and Calorimetry. 2007;89(2):459-64.

[267] Cheung TTP. Cyclopentadiene and Dicyclopentadiene. Kirk-Othmer Encyclopedia of Chemical Technology: John Wiley & Sons, Inc. 2000.

[268] Grubbs RH, Trnka TM. Ruthenium-Catalyzed Olefin Metathesis. Ruthenium in Organic Synthesis: Wiley-VCH Verlag GmbH & Co. KGaA 2005, p. 153-77.

[269] Jeong W, Kessler MR. Toughness Enhancement in ROMP Functionalized Carbon Nanotube/Polydicyclopentadiene Composites. Chemistry of Materials. 2008;20(22):7060-8.

[270] Adanur S. Wellington Sears Handbook of Industrial Textiles: Taylor & Francis; 1995.

[271] Frankland SJV, Caglar A, Brenner DW, Griebel M. Molecular Simulation of the Influence of Chemical Cross-Links on the Shear Strength of Carbon Nanotube–Polymer Interfaces. The Journal of Physical Chemistry B. 2002;106(12):3046-8.

[272] Chawla KK. Composite Materials: Science and Engineering: Springer; 1998.

[273] Morton WE, Hearle JWS, Institute T. Physical properties of textile fibres: Textile Institute; 1962.

[274] Hirata A, Yoshioka N. Sliding friction properties of carbon nanotube coatings deposited by microwave plasma chemical vapor deposition. Tribology International. 2004;37(11–12):893-8.

[275] Mylvaganam K, Zhang LC, Xiao KQ. Origin of friction in films of horizontally oriented carbon nanotubes sliding against diamond. Carbon. 2009;47(7):1693-700.

[276] Sawyer WG, Perry SS, Phillpot SR, Sinnott SB. Integrating experimental and simulation length and time scales in mechanistic studies of friction. Journal of Physics: Condensed Matter. 2008;20(35):354012.

[277] Tu JP, Zhu LP, Hou K, Guo SY. Synthesis and frictional properties of array film of amorphous carbon nanofibers on anodic aluminum oxide. Carbon. 2003;41(6):1257-63.

[278] Che J, Çagin T, III WAG. Thermal conductivity of carbon nanotubes. Nanotechnology. 2000;11(2):65.

[279] Tans SJ, Devoret MH, Dai H, Thess A, Smalley RE, Geerligs LJ, et al. Individual single-wall carbon nanotubes as quantum wires. Nature. 1997;386(6624):474-7.

[280] Mu M, Winey KI. Improved Load Transfer in Nanotube/Polymer Composites with Increased Polymer Molecular Weight†. The Journal of Physical Chemistry C. 2007;111(48):17923-7.

[281] Espy HH, Matlack AS, inventors; Hercules Incorporated, assignee. Conversion of Solid dicyclopentadiene to a liquid monomer for use in reaction injection molding. United States of America. 1988.

[282] Yu ST, Na SJ, Lim TS, Lee BY. Preparation of a Bulky Cycloolefin/Ethylene Copolymer and Its Tensile Properties. Macromolecules. 2010;43(2):725-30.

[283] Cançado LG, Jorio A, Ferreira EHM, Stavale F, Achete CA, Capaz RB, et al. Quantifying Defects in Graphene via Raman Spectroscopy at Different Excitation Energies. Nano Letters. 2011;11(8):3190-6.

[284] Jiang Q, Qu MZ, Zhou GM, Zhang BL, Yu ZL. A study of activated carbon nanotubes as electrochemical super capacitors electrode materials. Materials Letters. 2002;57(4):988-91.

[285] Long RQ, Yang RT. Carbon Nanotubes as Superior Sorbent for Dioxin Removal. Journal of the American Chemical Society. 2001;123(9):2058-9.

[286] Vohrer U, Kolaric I, Haque MH, Roth S, Detlaff-Weglikowska U. Carbon nanotube sheets for the use as artificial muscles. Carbon. 2004;42(5–6):1159-64.

[287] Wu G, Xu B-Q. Carbon nanotube supported Pt electrodes for methanol oxidation: A comparison between multi- and single-walled carbon nanotubes. Journal of Power Sources. 2007;174(1):148-58.

[288] Davies RJ, Riekel C, Koziol KK, Vilatela JJ, Windle AH. Structural studies on carbon nanotube fibres by synchrotron radiation microdiffraction and microfluorescence. Journal of Applied Crystallography. 2009;42(6):1122-8.

[289] Wu J, Schultz JM, Yeh F, Hsiao BS, Chu B. In-Situ Simultaneous Synchrotron Small- and Wide-Angle X-ray Scattering Measurement

of Poly(vinylidene fluoride) Fibers under Deformation. Macromolecules. 2000;33(5):1765-77.

[290] Miao M. Production, structure and properties of twistless carbon nanotube yarns with a high density sheath. Carbon. 2012;50(13):4973-83.